

UNIVERSITY OF CALIFORNIA, SAN DIEGO

Statistical Estimation and Tracking of Refractivity from Radar Clutter

A dissertation submitted in partial satisfaction of the
requirements for the degree Doctor of Philosophy

in

Electrical Engineering
(Applied Ocean Sciences)

by

Caglar Yardim

Committee in charge:

William S. Hodgkiss, Chair
Kenneth Kreutz-Delgado, Co-Chair
William A. Coles
Peter Gerstoft
William A. Kuperman
Robert Pinkel

2007

Copyright
Caglar Yardim, 2007
All rights reserved.

The dissertation of Caglar Yardim is approved, and it is
acceptable in quality and form for publication on microfilm:

Co-Chair

Chair

University of California, San Diego

2007

DEDICATION

To my family...

TABLE OF CONTENTS

| | |
|---|-------|
| Signature Page | iii |
| Dedication | iv |
| Table of Contents | v |
| List of Figures | viii |
| List of Tables | xii |
| Acknowledgements | xiii |
| Vita, Publications, and Fields of Study | xv |
| Abstract | xviii |
| 1 Introduction | 1 |
| 1.1 Background | 1 |
| 1.2 Properties of the Lower Atmosphere | 2 |
| 1.2.1 Electromagnetic Ducts | 5 |
| 1.2.2 Effects of Ducts on Naval Radar and Communication Systems | 8 |
| 1.2.3 Measurement of Duct Properties | 11 |
| 1.3 Electromagnetic Propagation in the Lower Atmosphere | 13 |
| 1.3.1 Tropospheric Propagation Using Split-Step Fast Fourier Transform Parabolic Equation | 14 |
| 1.3.2 Radar Sea Clutter Calculation Under Non-Standard Propagation Conditions | 19 |
| 1.4 Statistical Estimation and Tracking | 22 |
| 1.5 Scope of This Dissertation | 23 |
| Bibliography | 27 |
| 2 Estimation of Radio Refractivity from Radar Clutter Using Bayesian Monte Carlo Analysis | 30 |
| 2.1 Introduction | 31 |
| 2.2 Theory | 34 |
| 2.2.1 Bayesian Inversion | 35 |
| 2.2.2 Likelihood Function | 36 |
| 2.2.3 Markov Chain Monte Carlo Sampling | 37 |
| 2.2.4 Monte Carlo Integration | 40 |
| 2.3 Implementation | 40 |
| 2.3.1 Burn-in Phase | 40 |
| 2.3.2 Initial Sampling and Coordinate Rotation | 41 |

| | | |
|-------|--|-----|
| 2.3.3 | Final Sampling Phase and Convergence | 42 |
| 2.3.4 | Post-Processing | 44 |
| 2.4 | Examples | 44 |
| 2.4.1 | Algorithm Validation | 44 |
| 2.4.2 | Wallops Island Experiment | 48 |
| 2.5 | Conclusion | 55 |
| 2.6 | Acknowledgment | 57 |
| | Bibliography | 60 |
| 3 | Statistical Maritime Radar Duct Estimation Using a Hybrid Genetic Algorithms – Markov Chain Monte Carlo Method | 63 |
| 3.1 | Introduction | 64 |
| 3.2 | Model Formulation | 66 |
| 3.3 | The Hybrid GA-MCMC Method | 69 |
| 3.3.1 | Monte Carlo Integration and Genetic Algorithms | 69 |
| 3.3.2 | Voronoi Decomposition | 70 |
| 3.3.3 | MCMC (Gibbs) Resampling | 72 |
| 3.4 | Examples | 74 |
| 3.4.1 | Synthetic Data | 74 |
| 3.4.2 | Wallops’98 Data | 82 |
| 3.5 | Conclusion | 90 |
| 3.6 | Acknowledgment | 91 |
| | Bibliography | 93 |
| 4 | Tracking Refractivity From Clutter | 96 |
| 4.1 | Introduction | 97 |
| 4.2 | Theory | 98 |
| 4.2.1 | Creation of the 2-D Modified Refractivity Profile from State Variables | 100 |
| 4.2.2 | State Equation – Environmental Model | 101 |
| 4.2.3 | Measurement Equation – Propagation Model | 103 |
| 4.3 | Tracking Algorithms | 105 |
| 4.3.1 | Extended Kalman Filter | 105 |
| 4.3.2 | Unscented Kalman Filter | 106 |
| 4.3.3 | Particle Filter | 108 |
| 4.3.4 | Posterior Cramér-Rao Lower Bound | 109 |
| 4.4 | Examples | 111 |
| 4.4.1 | Case Study I: Temporal Tracking of a Range-Independent Surface-Based Duct | 111 |
| 4.4.2 | Case Study II: Divergence in Surface-Based Duct Tracking | 116 |
| 4.4.3 | Case Study III: Range-Dependent Evaporation Duct Tracking in Coastal Regions | 119 |

| | | |
|-------|--|-----|
| 4.5 | Discussion | 121 |
| 4.6 | Conclusion | 124 |
| 4.7 | Acknowledgment | 125 |
| | Bibliography | 126 |
| 5 | Conclusions and Future Work | 130 |
| 5.1 | Conclusions | 130 |
| 5.1.1 | Statistical Estimation of Refractivity | 130 |
| 5.1.2 | Refractivity Tracking | 132 |
| 5.2 | Future Work | 134 |

LIST OF FIGURES

| | |
|---|----|
| Figure 1.1: Tropospheric propagation conditions. Sub-refraction, standard refraction, super-refraction, and trapping (ducting). (Figure taken from [1]) | 4 |
| Figure 1.2: Most common three duct types. Evaporation, surface-based, and elevated ducts. | 6 |
| Figure 1.3: Vertical M-profiles, coverage diagrams, and clutter maps resulting from (a) a weak evaporation duct and (b) a strong surface-based duct. | 9 |
| Figure 1.4: Effects of ducting on naval and communication systems.(Figure taken from [1]) | 10 |
| Figure 1.5: Sea surface grazing angle as a function of range for different evaporation duct heights computed using ray-tracing. | 22 |
| Figure 1.6: An observation \mathbf{d} is mapped into a distribution of environmental parameters \mathbf{m} that potentially could have generated it. These environmental parameters are then mapped into the usage domain \mathbf{u} | 23 |
| Figure 2.1: Clutter map from Space Range Radar (SPANDAR) at Wallops Island, VA. | 32 |
| Figure 2.2: Tri-linear M-profile and its corresponding coverage diagram. | 33 |
| Figure 2.3: The 4-parameter tri-linear M-profile model used in this work. | 33 |
| Figure 2.4: Full implementation of the MCMC algorithm: (a) burn-in and initial sampling phases in the original parameter space, and (b) two parallel-running samplers operating on the new parameter landscape after coordinate rotation. | 41 |
| Figure 2.5: Initial sampling phase - convergence of the model covariance matrix in terms of percent error. \mathbf{C}_m later will be used for coordinate rotation. | 46 |
| Figure 2.6: Final sampling phase - Kolmogorov-Smirnov statistic D for each parameter. Used for the convergence of the posterior probability density. | 47 |
| Figure 2.7: Marginal posterior probability distributions for the synthetic test case. Vertical lines show the true values of the parameters. (a) exhaustive search, (b) Metropolis algorithm, (c) Gibbs algorithm, and (d) genetic algorithm. | 48 |
| Figure 2.8: Both 1-D marginal (diagonal) and 2-D marginal (upper diagonal) PPD's for the synthetic test case obtained by the Metropolis algorithm. Vertical lines (in 1-D plots) and crosses (in 2-D plots) show the true values of the parameters. | 49 |
| Figure 2.9: Wallops '98 Experiment: SPANDAR radar and the helicopter measurements (37.83° N, 75.48° W) | 50 |

| | |
|--|----|
| Figure 2.10: Marginal posterior probability distributions obtained using SPANDAR data. (a) Metropolis algorithm and (b) genetic algorithm. Vertical lines show the estimated optimum values of the parameters. | 51 |
| Figure 2.11: Both 1-D marginal (diagonal) and 2-D marginal (upper diagonal) PPD's obtained from the SPANDAR data obtained by the Metropolis algorithm. Vertical lines (in 1-D plots) and crosses (in 2-D plots) show the optimum values of the parameters. . . . | 52 |
| Figure 2.12: M-profiles 0-60km: (a) helicopter measurements at different ranges, (b) helicopter profiles and HPD regions for the range-independent model, and (c) range-independent ML solution and mean of the profiles measured at different ranges. | 53 |
| Figure 2.13: Coverage diagrams. One-way propagation loss for: (a) standard atmosphere, (b) helicopter-measured profile, and (c) Metropolis result. The difference between (d) helicopter and standard atmosphere and (e) helicopter and Metropolis results. | 54 |
| Figure 2.14: Clutter power vs. range plots. Clutter measured by SPANDAR (solid), the predicted clutter obtained using the Metropolis ML solution $\hat{\mathbf{m}}$ (dashed), and the predicted clutter obtained using the helicopter-measured refractivity profile (dotted). . . . | 55 |
| Figure 2.15: PPD for propagation factor F at range 60 km with altitudes of (a) 28 m and (b) 180 m above MSL. (c) PPD of the coverage area for the given communication link. | 56 |
| Figure 3.1: Four-parameter range-independent tri-linear M-profile. . . . | 67 |
| Figure 3.2: Voronoi cells and a single GS step. Conditional PPD's used in the Gibbs step for the given conditional cut lines are shown on the top and to the right of the Voronoi diagram. GA and Gibbs samples are represented by (*) and (♦), respectively. . . | 76 |
| Figure 3.3: Two adjacent cells V_i and V_j intersecting a conditional line. \mathbf{m}^i and \mathbf{m}^j are the corresponding GA samples. The conditional approximate PPD which is constant except for the cell boundary intersection is given above the Voronoi cell structure. | 77 |
| Figure 3.4: Marginal posterior densities for the synthetic case. Vertical lines show the true values of the parameters. (a) Exhaustive search, (b) Metropolis sampler (MCMC), (c) GA, and (d) hybrid GA-MCMC using 15k GA and 40k Gibbs samples. | 78 |
| Figure 3.5: Both 1-D marginal (diagonal) and 2-D marginal (upper diagonal) PPD's obtained by (a) exhaustive search and (b) hybrid GA-MCMC. Vertical lines (in 1-D plots) and crosses (in 2-D plots) show the true values of the parameters. | 79 |

| | |
|--|-----|
| Figure 3.6: Convergence in GA: Effect of GA sample size on 1-D marginal posterior densities for a 40k Gibbs sample size. Distributions calculated using (a) exhaustive search and the hybrid method with (b) 1k, (c) 5k, and (d) 15k GA samples. | 81 |
| Figure 3.7: Convergence in GS: Effect of GS sample size on 1-D marginal posterior densities for a 15k GA sample size. Distributions calculated using (a) exhaustive search and the hybrid method with (b) 1k, (c) 5k, and (d) 20k Gibbs samples. | 82 |
| Figure 3.8: Convergence of the hybrid method. D for each parameter as a function of (a) GA sample size for a 40k Gibbs sample size and (b) Gibbs sample size for a 15k GA sample size | 83 |
| Figure 3.9: An example of range-dependent sixteen parameter M-profile with four parameters per 20 km. Vertical profile at any given range is calculated by linear interpolation of both the slopes and the layer thicknesses. | 84 |
| Figure 3.10: Results for the Wallops data. (a) estimated and helicopter-measured profiles at various ranges and (b) SPANDAR clutter together with the clutter that one would obtain from the estimated range-dependent and independent environments. | 85 |
| Figure 3.11: Marginal and conditional distributions. (a) 1-D (diagonal) and 2-D (upper diagonal) posterior probability distributions in terms of percent HPD, for the range-dependent SPANDAR data inversion. (b) Error function for conditional planes. | 88 |
| Figure 3.12: Posterior densities for propagation factor F at three different ranges. Color plots show the PPD of F for height values between 0 m and 200 m in terms of percent HPD, with the MAP solution (dashed white). | 89 |
| Figure 3.13: Posterior probability densities for propagation factor F at (a) 20 and (b) 100 m altitudes. Color plots show the PPD of F for ranges between 0–90 km in terms of percent HPD, with the dashed white line showing the MAP solution. | 92 |
| Figure 4.1: Ten 2-D M-profiles measured by JHU helicopter, Wallops’98 experiment (gray) and best trilinear profile fit for each measurement (black). | 103 |
| Figure 4.2: Case study I. (a) Regional map and the location of the station (\times), (b) average spring M-profile, (c) 100 Monte Carlo trajectories, and (d) RMS errors of the EKF, UKF, and 200-particle PF along with the square root of the posterior CRLB. | 115 |
| Figure 4.3: Efficiency of the PF as a function of the number of particles. | 117 |
| Figure 4.4: Case Study II: Temporal evolution of the range-independent duct. | 117 |
| Figure 4.5: Evolution of the highly nonlinear relative radar clutter \mathbf{y}_k (dB) computed for the true environment without \mathbf{w}_k | 118 |

| | |
|---|-----|
| Figure 4.6: Case Study II: Temporal tracking of the range-independent SBD. c_1 and c_2 are in M-units/m and h_1 and h_2 are in meters. True trajectories (dashed) and filter estimates (solid) for the EKF, UKF and PF-200. | 119 |
| Figure 4.7: Case Study III. (a) EDH statistics and (b) air-sea temperature difference, (c) spatio-temporal evolution of the EDH, (d) 2-D M-profiles, and (e) the evolution of the EDH for the selected range grid that is used to construct the state vector \mathbf{x}_k | 123 |

LIST OF TABLES

| | |
|---|-----|
| Table 1.1: Tropospheric Propagation Conditions | 5 |
| Table 1.2: Some Regional Duct Statistics | 8 |
| Table 2.1: Notation | 58 |
| Table 2.2: Synthetic data case: GA estimates and Metropolis algorithm results | 59 |
| Table 2.3: Wallops island experiment (clutter map 17): GA estimates and Metropolis algorithm results | 59 |
| Table 3.1: System Parameters | 75 |
| Table 3.2: Synthetic data case: Model Parameters | 75 |
| Table 3.3: Wallops'98 Experiment: Model Parameters | 90 |
| Table 4.1: Case Study I: Comparison of Tracking Algorithms and CRLB Radiosonde Station Bahrain, Persian Gulf | 112 |
| Table 4.2: Performance Comparison for Case Study I | 114 |
| Table 4.3: Performance Comparison for Case Study II | 120 |
| Table 4.4: Case Study III: Coastal Range-Dependent Evaporation Duct Tracking, Eastern Mediterranean | 122 |
| Table 4.5: Performance Comparison for Case Study III | 122 |

ACKNOWLEDGMENTS

I would like to genuinely thank my advisors, Professor William S. Hodgkiss and Dr. Peter Gerstoft, for their inspirational guidance, constant support, encouragement, affection, and patience throughout my Ph.D. work, in their entirely different but equally effective American and European ways. They guided me at every step of my Ph.D. journey and helped me keep on track, teaching me not only the knowledge necessary for this dissertation but beyond that teaching me how to learn and conduct independent research which, I now realize, is far more important than the work itself. I am truly grateful for this life changing five years.

I am also thankful to my committee members, Professor Kenneth Kreutz-Delgado, Professor William A. Coles, Professor William A. Kuperman, and Professor Robert Pinkel for their valuable comments and time.

I would like to thank everybody at the Marine Physical Laboratory (MPL) for their help and friendship. I wish to express my gratitude to Evelyn Doudera for keeping all the graduate students at MPL well-fed and caffeinated at all times, to Chen-fen Huang for helping me at every step with our long discussions, and to all my friends at UCSD.

I would like to thank Ted Rogers at Space and Naval Warfare Systems Center, San Diego, CA for his invaluable discussions, comments and for providing us with the Wallops Island Experiment results.

Finally, I would like to dedicate my dissertation to my family, my parents, my brother, his wife, little Doga and Elif for their love and constant encouragement. It would have been impossible to complete this work without their understanding and support.

This work was supported by the Office of Naval Research Code 32, under grant No. N00014-05-1-0369.

This dissertation is a collection of papers that were published or submitted for publication. The text of Chapter Two is in full a reprint of the material as it appears in Caglar Yardim, Peter Gerstoft, and William S. Hodgkiss,

"Estimation of radio refractivity from radar clutter using Bayesian Monte Carlo analysis," *IEEE Trans. on Antennas and Propagation*, vol. 54, pp. 1318-1327, doi:10.1109/TAP.2006.872673, 2006.

The text of Chapter Three is in full a reprint of the material as it appears in Caglar Yardim, Peter Gerstoft, and William S. Hodgkiss, "Statistical maritime radar duct estimation using a hybrid genetic algorithms - Markov chain Monte Carlo method," *Radio Science*, in press 2007.

The text of Chapter Four is in part and under some rearrangements a reprint of the material as it appears in Caglar Yardim, Peter Gerstoft, and William S. Hodgkiss, "Tracking refractivity from radar clutter," *IEEE Trans. on Antennas and Propagation*, submitted 2007.

The dissertation author was the primary researcher and author, and the co-authors listed in these publications directed and supervised the research which forms the basis for this dissertation.

VITA

| | |
|-----------|--|
| 1998 | B.S. in Electrical Engineering, Middle East Technical University, Ankara, Turkey |
| 2001 | M.S. in Electrical Engineering, Middle East Technical University, Ankara, Turkey |
| 2007 | Ph.D. in Electrical Engineering, University of California, San Diego, CA |
| 1998-2000 | Teaching/Research Assistant, Department of Electrical and Electronics Engineering, Middle East Technical University, Ankara, Turkey |
| 2000-2002 | Research and Development Engineer, Radar and Electronic Warfare Section, Microwave System Technologies Division, ASELSAN Military Electronics Inc., Ankara, Turkey |
| 2002-2007 | Graduate Student Research Associate Marine Physical Laboratory, Scripps Institution of Oceanography, University of California, San Diego, CA |

PUBLICATIONS

Journals

1. C. Yardim, P. Gerstoft, and W. S. Hodgkiss, Estimation of radio refractivity from radar clutter using Bayesian Monte Carlo analysis, *IEEE Trans. on Antennas and Propagation*, vol. 54, pp. 1318-1327, doi:10.1109/TAP.2006.872673, 2006.
2. C. Yardim, P. Gerstoft, and W. S. Hodgkiss, Statistical maritime radar duct estimation using a hybrid genetic algorithms - Markov chain Monte Carlo method, *Radio Science*, in press 2007.
3. C. Yardim, P. Gerstoft, and W. S. Hodgkiss, Tracking refractivity from radar clutter, *IEEE Trans. on Antennas and Propagation*, submitted 2007.

Conferences

1. C. Yardim, P. Gerstoft, and W. S. Hodgkiss, Tracking atmospheric ducts using radar clutter: Evaporation duct tracking using Kalman filters, *IEEE Antennas and Propagation Conference*, Honolulu, HI, June 2007.

2. C. Yardim, P. Gerstoft, and W. S. Hodgkiss, Tracking atmospheric ducts using radar clutter: Surface-based duct tracking using multiple model particle filters, *IEEE Antennas and Propagation Conference*, Honolulu, HI, June 2007.
3. (INVITED) C. Yardim, P. Gerstoft, W. S. Hodgkiss, and Ted Rogers, Statistical estimation of refractivity from radar sea clutter, *IEEE Radar Conference*, Waltham, MA, April 2007.
4. C. Yardim, P. Gerstoft, and W. S. Hodgkiss, Atmospheric refractivity tracking from radar clutter using Kalman and particle filters, *IEEE Radar Conference*, Waltham, MA, April 2007.
5. C. Yardim, P. Gerstoft, and W. S. Hodgkiss, Error variance estimation in Bayesian refractivity from clutter inversion, *USNC/URSI Conference*, Boulder, CO, January 2006.
6. (INVITED) C. Yardim, P. Gerstoft, and W. S. Hodgkiss, A fast hybrid genetic algorithm-Gibbs sampler approach to estimate geoacoustic parameter uncertainties, *Underwater Acoustic Measurements Conference*, Crete, Greece, June 2005.
7. C. Yardim, P. Gerstoft, W. S. Hodgkiss, and C.-F. Huang, Refractivity from clutter (RFC) estimation using a hybrid genetic algorithm - Markov chain Monte Carlo method, *IEEE Antennas and Propagation & USNC/URSI Conference*, Washington DC, July 2005.
8. C. Yardim, P. Gerstoft, and W. S. Hodgkiss, Estimation of radio refractivity from clutter using Bayesian Monte Carlo analysis, *USNC/URSI Conference*, Boulder, CO, January 2005.
9. C. Yardim, P. Gerstoft, and W. S. Hodgkiss, Uncertainty analysis in the refractivity from clutter (RFC) problem, *IEEE Antennas and Propagation & USNC/URSI Conference*, Monterey, CA, June 2004.
10. A. Hizal, C. Yardim, and E. Halavut, Wideband tapered rolling strip antenna, *IEEE AP2000 Millennium Conference on Antennas & Propagation*, Davos, Switzerland, April, 2000.
11. A. Hizal, E. Halavut, C. Yardim, and A. Celebi, A linear patch antenna array for adaptive beamforming with a spherical wave incidence, *COST 260 Workshop on Smart Antennas*, Aveiro, Portugal, November 1999.

Other

1. C. Yardim and P. Gerstoft, Applicability of refractivity from clutter (RFC) method in various seas for existing radar systems, *Joint MPL/UCSD - Lockheed Martin (LM) Project Report*, December, 2005.
2. C. Yardim, Design and construction of annular sector radiating line (ANSERLIN), microstrip helix radiating line (MISHERLIN), and tapered rolling strip (TAROS) antennas, *M.S. Thesis*, 2001.

FIELDS OF STUDY

Major Field: Electrical Engineering

Studies in digital signal processing, optimization, estimation theory, detection theory, array processing, and their applications in the atmospheric refractivity estimation problem.

Professors William S. Hodgkiss and Kenneth Kreutz-Delgado, Dr. Peter Gerstoft

Studies in applied ocean science, electromagnetic ducts, effects of ducting on naval radar systems, acoustic and electromagnetic propagation in inhomogeneous media, and their applications in radar clutter prediction for non-standard lower atmospheric maritime environments.

Professor William A. Kuperman, Dr. Peter Gerstoft

ABSTRACT OF THE DISSERTATION

Statistical Estimation and Tracking of Refractivity from Radar Clutter

by

Caglar Yardim

Doctor of Philosophy in Electrical Engineering

(Applied Ocean Sciences)

University of California, San Diego, 2007

William S. Hodgkiss, Chair

Kenneth Kreutz-Delgado, Co-Chair

In many maritime regions of the world, such as the Mediterranean, Persian Gulf, East China Sea, and the Californian Coast, atmospheric ducts are common occurrences. They result in various anomalies such as significant variations in the maximum operational radar range, creation of regions where the radar is practically blind (radar holes) and increased sea clutter. Therefore, it is important to predict the real-time 3-D environment in which the radar is operating so that the radar operator will at least know the true system limitations and in some cases even compensate for them.

This dissertation addresses the estimation and tracking of the lower atmospheric radio refractivity under non-standard propagation conditions frequently encountered in low altitude maritime radar applications. This is done by statistically estimating the duct strength (range and height-dependent atmospheric index of refraction) from the sea-surface reflected radar clutter. Therefore, such methods are called Refractivity From Clutter (RFC) techniques. These environmental statistics can then be used to predict the radar performance. The electromagnetic propagation in these complex environments is simulated using a split-step fast Fourier transform (FFT) based parabolic equation (PE) approximation to the wave equation.

The first part of this thesis discusses various algorithms such as genetic algorithms (GA), Markov chain Monte Carlo samplers (MCMC) and the hybrid GA-MCMC samplers that are used to estimate atmospheric radio refractivity for a given azimuth direction and time. The results show that radar clutter can be a rich source of information about the environment and the techniques mentioned above are used successfully as near real-time estimators for the data collected during the Wallops'98 experiment conducted by the Naval Surface Warfare Center.

The second part of this dissertation focuses on both spatial and temporal tracking of the 3-D environment. Techniques such as the extended (EKF) and unscented (UKF) Kalman filters, and particle filters (PF) are used for tracking the spatial and temporal evolution of the lower atmosphere. Even though the tracking performance of the Kalman filters was limited for certain duct types such as the surface-based ducts due to the high non-linearity of the split-step FFT PE, they performed well for other environments such as evaporation ducts. On the other hand, particle filters proved to be very promising in tracking a wide variety of scenarios including even abruptly changing environments.

1

Introduction

1.1 Background

The main objective of this dissertation is to predict and improve maritime radar performance by statistically estimating and tracking the three dimensional real-time properties of the lower atmosphere in which the radar is operating. This means that one has to predict the electromagnetic lower atmospheric ducts that frequently form in many ocean and coastal regions of the world. Therefore, this necessitates the understanding of these atmospheric events, the ability to predict their effects on a radar system, the estimation of the environment using the measured clutter, and finally compensating and taking necessary precautions to counter the effects.

Hence, the work done in this dissertation involves three different fields:

1. *Meteorology*, for understanding the common lower atmospheric phenomena that affect electromagnetic propagation, radar, and communication systems operating in various environments, the atmospheric dynamics that result in the formation of electromagnetic ducts, types of ducts and their differences, the regions there they commonly occur, their occurrence rates, spatial and temporal variabilities, differences between coastal and open water environments, and the ability to forecast duct properties using meteorological

models.

2. *Electromagnetic Theory*, particularly radar theory and electromagnetic propagation in inhomogeneous media, for understanding how the radar signal propagates in complex environments, the effects of the atmospheric duct as a leaky waveguide, interaction and scattering of the electromagnetic signal with the sea surface for very low angle of incidence and different sea states, incidence angle and sea clutter calculations using ray-tracing and the split-step fast Fourier transform based parabolic equation approximation to the wave equation.
3. *Signal Processing*, for understanding how to formulate the problem in a Bayesian framework, the statistical estimation of the environmental duct parameters from the measured radar clutter using techniques such as genetic algorithms (GA), different Markov chain Monte Carlo samplers (MCMC), and hybrid GA-MCMC samplers that use nearest neighborhood and Voronoi decomposition techniques, spatial and temporal tracking of the range, height, azimuth and time dependent atmospheric index of refraction using various Kalman and particle filters.

1.2 Properties of the Lower Atmosphere

The term refraction refers to the property of a medium to bend an electromagnetic wave as it passes through the medium. The index of refraction of a medium, n is defined as the ratio of the speed of light in vacuum to that of the medium $n = c/v$. For many atmospheric applications it is simply taken as unity since the atmospheric n changes only slightly, between 1.000250 and 1.000400 in the lower atmosphere [1,2]. These fluctuations in the index of refraction are caused by local changes in the temperature, pressure, and the humidity of the atmosphere. Since the deviations are small, a new parameter N called the refractivity is defined as the part-per-million (ppm) change in n , and is used for convenience in prop-

agation calculations. Due to the curvature of the Earth, an initially horizontally propagating signal will be moving away from the surface. To take this effect into account, the modified refractivity (M) has been introduced. N and M can be computed as

$$N = (n - 1) \times 10^6 = \frac{77.6p}{T} + \frac{e_s 3.73 \times 10^5}{T^2} \quad (1.1)$$

$$e_s = \frac{rh 6.105 \exp x}{100} \quad (1.2)$$

$$x = 25.22 \frac{T - 273.2}{T} - 5.31 \log_e \left(\frac{T}{273.2} \right) \quad (1.3)$$

$$M = N + \frac{h}{a} \times 10^6 \quad (1.4)$$

$$M \simeq N + 0.157h, \quad (1.5)$$

where e_s is the partial pressure of water vapor, p is the barometric pressure in millibars, T is the temperature in °K, rh is the percent relative humidity, h is the height above the earth's surface, and a is the radius of the Earth.

Classification of Atmospheric Conditions

Even though the fluctuations are on the order of part-per-millions, they are sufficient to cause major changes in the tropospheric electromagnetic propagation. Normally, the refractivity is a near-exponential function of the altitude. This exponential can be linearized within the first kilometer or so of the atmosphere. The slope of this linear function is -0.039 N-units/m or 0.118 M-units/m and it usually is referred to as the “standard atmosphere”. Standard atmosphere will result in a downward bending of the electromagnetic wave. However, this is less than the curvature of the earth, effectively resulting in a wave that slowly moves away from the surface. This type of propagation is called the normal propagation condition and it occurs as long as N is between -0.079 to 0 N-units/m (0.079 to 0.157 M-units/m).

If N has a positive slope with respect to the altitude, the wave will further bend upward creating the sub-refractive conditions, which only infrequently occurs

in nature.

On the other hand if the N-gradient continues to decrease it can reach a critical value of -0.157 N-units/m (0 M-units/m). At this point the downward bending caused by refraction exactly matches the curvature of the earth creating an electromagnetic wave propagating horizontally to the surface. The condition where the refraction strength is between the normal and this critical value is called the super-refraction condition.

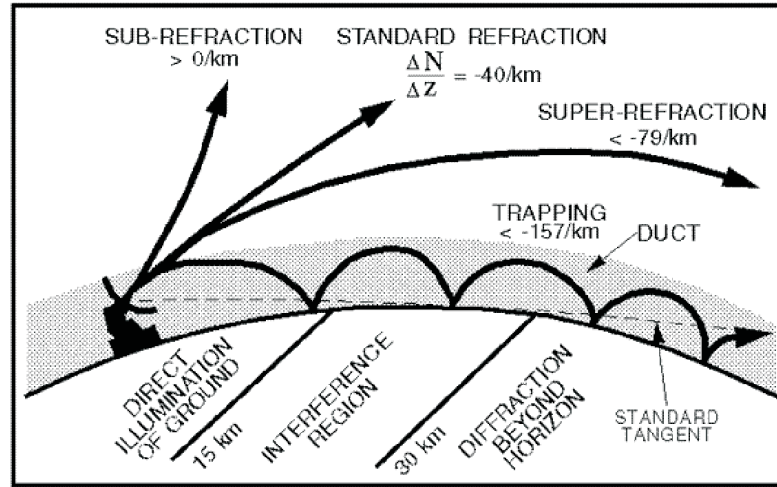


Figure 1.1: Tropospheric propagation conditions. Sub-refraction, standard refraction, super-refraction, and trapping (ducting). (Figure taken from [1])

If the negative N-gradient is even stronger than the critical value, the wave will be forced to bend downward, eventually hitting the surface. However, since the surface-reflected wave will reenter the strongly negative N-gradient region it will again be bent down bouncing multiple times from the surface as shown in Fig. 1.1. It effectively will be trapped between the surface and an imaginary upper boundary creating a waveguide with an open leaky top wall called an electromagnetic duct. Therefore this condition is called the trapping condition. These conditions are summarized in Table 1.1.

Table 1.1: Tropospheric Propagation Conditions

| Atmospheric Condition | $\frac{\partial N}{\partial z}$ (N-units/m) | $\frac{\partial M}{\partial z}$ (M-units/m) |
|-----------------------|---|---|
| Standard | -0.039 | 0.118 |
| Sub-refraction | >0 | >0.157 |
| Normal | -0.079 - 0 | 0.079 - 0.157 |
| Super-refraction | -0.157 - -0.079 | 0 - 0.079 |
| Trapping | <-0.157 | <0 |

1.2.1 Electromagnetic Ducts

An electromagnetic duct is formed when the atmospheric index of refraction sharply decreases with altitude. There are two atmospheric processes that can achieve this:

1. A humidity inversion, where the water-vapor content decreases with height.
2. A temperature inversion, where the temperature increases with height.

Land ducts usually occur at nights when the land mass cools down while the upper air is not affected, creating a temperature inversion. Strong land ducts can be produced if the ground is moist, enhancing the temperature inversion by a humidity inversion.

Another duct formation is the thunderstorm duct. The relatively cool air which spreads out from the base of a thunderstorm results in a temperature inversion. This usually is strengthened by a humidity inversion created by the moisture gradient of the thunderstorm.

However, the effects of the temperature inversion are not as strong as that of the humidity inversion so any strong and persistent duct formation can be sustained only in high humidity regions, hence the ocean and coastal areas. The inherent moisture inversion profile in the lower atmosphere above large water masses is a perfect environment for duct formation. When supported by a temperature inversion (typically caused by advection of the warm and dry continental air

over the coastal regions and the ocean) very strong sea ducts of several hundred kilometer size can be formed, lasting for days. Typical examples that induce strong duct formations include the Santa Ana of southern California, the Sirocco of the southern Mediterranean, and the Shamal of the Persian Gulf.

The sea duct essentially is a fine-weather phenomenon. Since it requires a strongly stratified atmosphere for temperature and humidity inversion, a well mixed atmosphere due to poor weather conditions will prevent sea duct formation. Rough terrain, high winds, cold, stormy, rainy, and cloudy conditions usually will result in more uniform vertical temperature and humidity profiles, decreasing duct formation. Therefore ducting is more common in equatorial, tropical, and sub-tropical regions. Ducting is further enhanced in these regions due to the high evaporation rate. The same is true for the summer and day time ducts [1, 2].

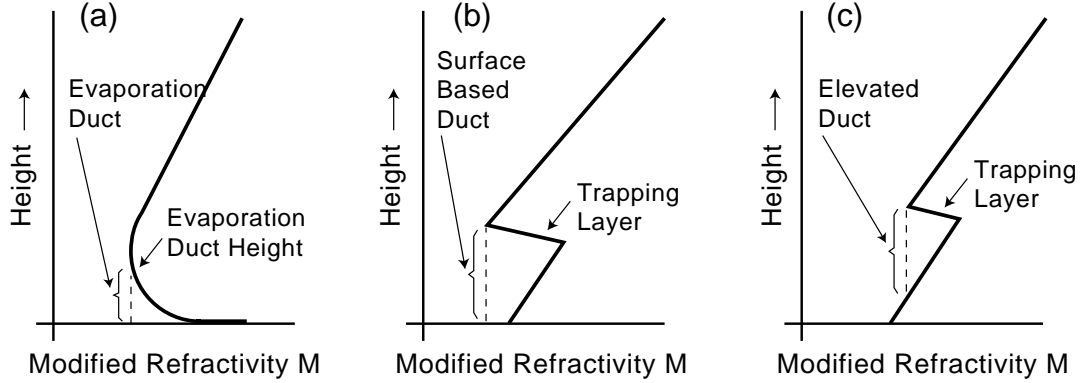


Figure 1.2: Most common three duct types. Evaporation, surface-based, and elevated ducts.

There are three major sea ducts frequently encountered in the lower atmosphere (Fig. 1.2):

1. *Evaporation ducts (ED)* are formed due to the inherent humidity inversion at the air/sea boundary. They are the most commonly encountered type of sea ducts. The air in contact with the sea is saturated with water vapor and the water vapor decreases approximately as a logarithmic function of height creating the evaporation duct structure given in Fig. 1.2 (a). The

height at which the modified refractivity M becomes minimum is called the evaporation duct height (EDH). ED formation is a strong function of latitude since the necessary evaporation rates required cannot be sustained in colder regions. For example, an evaporation duct with an $\text{EDH} > 10$ m occurs 92 % of the time in the coastal regions of northern Brazil, whereas this number is only 2 % at Bering Strait. EDH will very rarely be more than 40 m and the world average is 13 m.

2. *Surface-based ducts (SBD)* are formed when sharp humidity and temperature inversions occur due to the advection of warm and dry air over the ocean. The humidity gradient is usually further enhanced due to the evaporation from the sea surface. They are less common than the evaporation ducts but usually have a more pronounced effect on electromagnetic propagation. They typically are represented by a tri-linear profile with a negatively-sloped trapping layer as given in Fig. 1.2 (b). When the bottom of the trapping layer touches the sea surface, the SBD is sometimes referred to as a surface duct. In both the SBD and ED, the sea surface serves as the bottom boundary for the leaky electromagnetic waveguide.
3. *Elevated ducts (ElevD)* are formed due to the presence of marine boundary layers. The resultant inversion is called tradewind inversion, generating an strong duct at the top of the marine boundary layer. Elevated duct also has a tri-linear profile similar to a SBD as given in Fig. 1.2 (c). Elevated ducts are formed essentially from the same meteorological conditions as a SBD. In fact, coastal SBD's can slope upward to become elevated ducts. Similarly, a tradewind inversion may intensify, turning an elevated duct into a SBD. Elevated ducts usually occur at altitudes much higher than the SBD. For example the average elevated duct height is 600 m and 1500 m, respectively for the southern California coast and the coast of Japan. The fundamental difference between an elevated duct and other duct types is that the duct

is no more bounded below by the sea surface. This is especially important for RFC, since the ducting conditions are inferred from the surface-reflected sea clutter. Since elevated ducts do not interact with the surface, the RFC techniques discussed in this dissertation cannot be used for elevated duct prediction.

Annual regional statistics of different regions throughout the world are given in Table 1.2.

Table 1.2: Some Regional Duct Statistics

| Region | Percent Occurrence (Annual Averages) | | | | | | | |
|--|--------------------------------------|----|-----|----|-------|----|-------------|-----------|
| | ED>10 m | | SBD | | ElevD | | multi-Elev. | Elev.+SBD |
| | D | N | D | N | D | N | D/N Avg. | D/N Avg. |
| Persian Gulf | 77 | 62 | 36 | 52 | 26 | 33 | 2.8 | 4.8 |
| Gulf of Mexico | 84 | 79 | 9 | 10 | 38 | 40 | 8.3 | 2.6 |
| East China Sea | 83 | 76 | 10 | 7 | 15 | 18 | 3.4 | 2.0 |
| (Indian Ocean) Diego Garcia | 87 | 76 | 34 | 18 | 20 | 37 | 7.3 | 3.8 |
| (Atlantic Ocean) Rio Grande do Nor. | 92 | 87 | 18 | 18 | 24 | 30 | 6.8 | 7.2 |
| East Mediterranean | 72 | 62 | 13 | 11 | 12 | 16 | 2.4 | 2.5 |
| West Mediterranean | 58 | 45 | 15 | 14 | 10 | 12 | 1.7 | 2.6 |
| Yellow Sea | 63 | 56 | 16 | 13 | 17 | 18 | 7.0 | 3.4 |
| Southern California | 46 | 35 | 23 | 15 | 33 | 38 | 5.6 | 3.2 |
| Baltic Sea | 12 | 8 | 2 | 3 | 3 | 4 | 0.6 | 0.4 |
| Bering Strait | 2 | 1 | 6 | 5 | 4 | 5 | 1.1 | 0.8 |

1.2.2 Effects of Ducts on Naval Radar and Communication Systems

Even though the sub-refractive and super-refractive conditions are important in their own right, they do not result in a major change in the shape of the coverage diagram of a radar. On the contrary, trapping conditions will fundamen-

tally alter the propagation characteristics, the coverage area, and hence almost all of the important radar parameters as shown in Fig. 1.3.

The M-profile structure seen in Fig. 1.3 (a) is a weak evaporation duct. Notice how the value of M increases at a rate of 0.118 M-units/m except for the evaporative region near the surface. Since the evaporation duct is very weak it does not affect the propagation as seen from its coverage diagram obtained using the split-step fast Fourier transform (FFT) parabolic equation (PE). The upward bending effect of the normal propagation conditions can be seen clearly. Since the signal is bend upward, it has minimal interaction with the sea surface resulting in a clear clutter map, defined as the clutter observed on the radar plan position indicator (PPI).

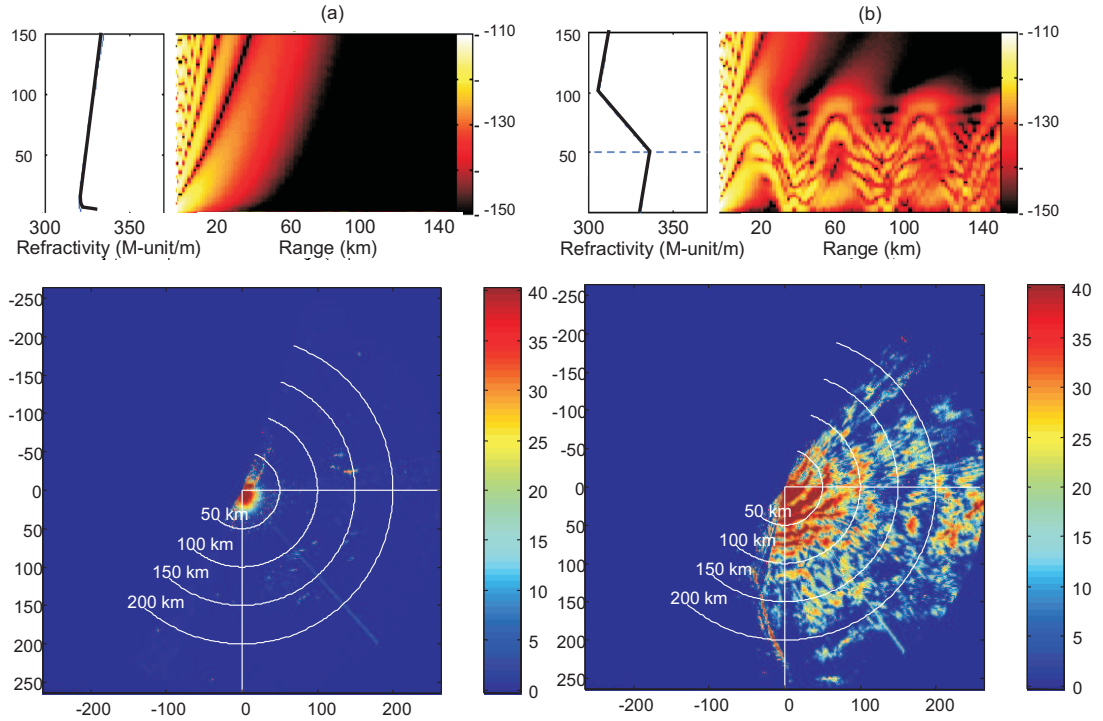


Figure 1.3: Vertical M-profiles, coverage diagrams, and clutter maps resulting from (a) a weak evaporation duct and (b) a strong surface-based duct.

Fig. 1.3 (b) shows what happens in the event of the formation a lower atmospheric duct. The coverage diagram is now entirely changed with a complex waveguide-like propagation pattern within the duct. Since the electromagnetic wave is trapped, it interacts heavily with the surface, resulting in an increase in the sea clutter observed by the radar. With each bounce, a small portion of the signal is scattered depending on the surface roughness and observed by the radar as shown on the radar PPI. Since the surface bounces occur at certain ranges as shown in the coverage diagram, it results in the formation of clutter rings around the radar on the PPI screen. The RFC techniques introduced in this dissertation uses this effect to estimate and track the atmospheric ducting conditions.

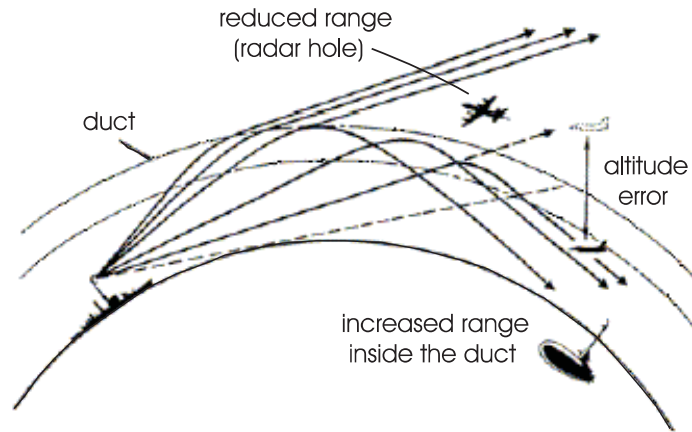


Figure 1.4: Effects of ducting on naval and communication systems.(Figure taken from [1])

The propagation changes discussed above result in important deviations in the radar/communication system characteristics as shown in Fig. 1.4. An important effect of ducting is the change in the maximum radar detection/communication channel range. For example, the range can be reduced significantly outside the duct since most of the electromagnetic signal is trapped within the duct. These areas are called radar holes. On the contrary, the maximum detection range within the

duct increases typically from two to five times that of a standard atmospheric case [2].

Moreover, ducting will also cause altitude errors in the target location due to the strong bending of the wave. System performance may also suffer from increased sea clutter.

1.2.3 Measurement of Duct Properties

The most accurate way of measuring the atmospheric refractivity profile is using a microwave refractometer [2,3]. It measures the index of refraction directly by using cavity resonance. It is composed of two microwave cavities fed by the same source. One is an open cavity that will collect the sample of atmosphere and the other one is a sealed cavity acting as a reference. The difference in the resonance frequencies will indicate how much difference there is between the two media, enabling the measurement of the n of the environment. Even with its very high accuracy and measurement speed refractometers are expensive and must be used with a helicopter or plane flying in a sawtooth pattern to obtain the two dimensional height and range dependent profile greatly limiting their usage.

The most common measurement technique is measuring n indirectly from the atmospheric temperature, humidity and pressure profiles, and using these in (1.1). Radiosonde balloons [4] that carry conventional weather observation instruments to measure these three environmental parameters are used for this purpose. Their shortcomings are the slow response time (typically 30 min. to get a vertical profile), slow update rate (typically one launch every two to twelve hours), inability to obtain range-dependent profiles, local heat sources lowering the accuracy (especially the effect of the metallic body of the ship it is launched from), non-vertical sampling due to the horizontal drift resulting from the wind, the need of extra hardware and measurement, and the associated cost for these hardware. These drawbacks also are valid for the rocketsondes that essentially do the same thing.

Doppler spread radars [5] are another way of gathering information about the environment. Although they do not directly measure the refractivity profile, they provide detailed temporal and spatial pictures of the structure parameter C_n^2 describing the turbulent perturbations in the refractivity. This theoretically can be used to extract refractivity itself. However, in practice, clouds, other contaminants, the need for a high signal to noise ratio, and contamination of the doppler spectrum due to non-turbulence related processes limit the effectiveness of the technique.

One other option is to forecast the ducting conditions using atmospheric prediction models. One such has recently been developed by the US Navy. The Coupled Ocean/Atmosphere Mesoscale Prediction System (COAMPS), developed by the Naval Research Laboratory (NRL), is a high-resolution, local weather-prediction model coupled with a powerful data assimilation code that integrates regional and satellite measurements [6,7]. It can provide a range-dependent “ducting forecast” anywhere around the world and usually updates every 12 hours. However, COAMPS also has limited capabilities and the M-profile predictions near the surface have relatively poor accuracy.

Another technique that can infer the refractivity is the lidar [8] techniques such as the differential absorption lidar (DIAL) and the Raman lidar. Lidars are used to measure the temperature and water vapor profiles. DIAL uses the strong wavelength-dependent absorption characteristics of atmospheric gases. Raman-scattering lidars utilize a weak molecular scattering process which shifts the incident wavelength by a fixed amount associated with rotational or vibrational transitions of the scattering molecule. They can measure both horizontal and vertical variations and are much faster than radiosondes. Disadvantages of lidar are that it is a more complex technique using expensive equipment and that lidars are limited by daytime background radiation and aerosol extinction.

The Global Positioning System (GPS) technique [9] is an attempt to use GPS satellites to infer the atmospheric environment. Similar to the radar signal, a GPS signal from a rising or setting satellite just over the horizon will

be distorted while propagating through the duct. Therefore, it may be possible to get information about the environment through which the GPS signal passes. This method estimates duct parameters by matching the delays in the received GPS signal using a ray-tracing code. Although still under development, GPS measurements may be a promising alternative to the radiosonde measurements due to higher update rates.

Finally, one can use the radar itself to gather information about the environment. The prospect of using the radar itself during its normal operation without needing any other hardware or extra measurements makes the refractivity from clutter (RFC) technique a promising alternative and addition to the methods provided above. It would only require the radar clutter, the normally filtered-out and discarded part of the radar signal, as its input. The technique potentially can provide the estimation and tracking of the range, azimuth and time-dependent three-dimensional cylindrical refractivity profile with the radar at its center. However it should also be noted that, similar to the techniques above, RFC comes with its own limitations and assumptions as discussed in detail throughout the dissertation.

1.3 Electromagnetic Propagation in the Lower Atmosphere

The electromagnetic theory section can be split into two sections. First one describes the split-step fast Fourier transform parabolic equation approximation to the wave equation used in this work and the other describes the extraction of the radar clutter return in this complex environment using the radar equation, taking into account the very low-angle sea surface radar cross section and the adjustment in the propagation loss due to the non-standard propagation.

1.3.1 Tropospheric Propagation Using Split-Step Fast Fourier Transform Parabolic Equation

Computation of the electromagnetic propagation in the atmosphere usually means solving the Maxwell's equations for a very large domain of interest with respect to the wavelength. This makes it impossible to solve the exact problem and approximations are made to simplify the problem to a manageable size. For many years, approximate methods such as the geometrical optics and mode theory have been used in tropospheric propagation calculations involving complex refraction problems such as the non-standard propagation formed under ducting conditions. These methods were largely replaced in 1990's by the parabolic equation (PE) following the introduction of the method in [10]. The formulation developed below is based on the ones given in [11–14]. Two different PE codes are used throughout this dissertation; our own code developed following [14] that is embedded into our Monte Carlo sampler and tracking algorithm codes, and the Terrain Parabolic Equation Model (TPEM) code written by Amalia E. Barrios [13].

Assuming a time harmonic variation of $e^{-j\omega t}$, the two dimensional cylindrical scalar wave equation for the electromagnetic field $\psi(r, z)$ in a homogeneous medium with a refractive index n can be written as

$$\frac{\partial^2 \psi}{\partial r^2} + \frac{1}{r} \frac{\partial \psi}{\partial r} + \frac{\partial^2 \psi}{\partial z^2} + k^2 n^2 \psi = 0, \quad (1.6)$$

where k is the wave number, r and z are range and height of the cylindrical coordinates (r, θ, z) , respectively. However, in reality the index of refraction will not be constant in our inhomogeneous medium but a function of r and z as $n(r, z)$. But since the variation in n will almost always be very small relative to the wavelength, (1.6) is still a highly accurate approximation.

An electromagnetic field trapped within the duct would have a canonical outgoing solution to the wave equation in cylindrical coordinates in terms of a Hankel function $H_0^1(kr)$ of the first kind and of order 0. Since the Hankel function can be represented by the first order term in its asymptotic expansion in the

far-field, one can define the reduced function $u(r, z)$ in terms of the field $\psi(r, z)$ propagating in the r -direction as

$$H_0^1(kr) \simeq \sqrt{\frac{2}{\pi kr}} e^{j(kr - \frac{\pi}{4})} \quad (1.7)$$

$$u(r, z) = \sqrt{kr} e^{-jkr} \psi(r, z). \quad (1.8)$$

where the square root term represents the decay in cylindrical spreading ($1/\sqrt{r}$ compared to the $1/r$ decay term of the classical spherical spreading). Inserting (1.8) into (1.6) one can obtain the wave equation for a flat earth given by

$$\left\{ \frac{\partial^2}{\partial r^2} + 2jk \frac{\partial}{\partial r} + \frac{\partial^2}{\partial z^2} + k^2(n^2 - 1) \right\} u(r, z) = 0, \quad (1.9)$$

which can be factored as

$$\left\{ \frac{\partial}{\partial r} + jk(1 - Q) \right\} \left\{ \frac{\partial}{\partial r} + jk(1 + Q) \right\} u(r, z) = 0. \quad (1.10)$$

Q in (1.10) is a pseudo-differential operator defined by

$$Q(Q(u)) = \frac{1}{k^2} \frac{\partial^2 u}{\partial z^2} + n^2 u. \quad (1.11)$$

By defining a special square root function that corresponds to the composition of operators one can formally define Q as

$$Q = \sqrt{\frac{1}{k^2} \frac{\partial^2}{\partial z^2} + n^2(r, z)}. \quad (1.12)$$

Finally one can define a function Z such that

$$Z = \frac{1}{k^2} \frac{\partial^2}{\partial z^2} + (n^2 - 1) \quad (1.13)$$

$$Q = \sqrt{1 + Z}. \quad (1.14)$$

One should note that there are inherent errors in the factorization given in (1.10).

If the index of refraction n varies considerably with range, then the operator Q does not commute with the range derivative and the factorization fails.

Now the wave equation can readily be split into outgoing and incoming field components, each corresponding to a parabolic equation

$$\frac{\partial u_+}{\partial r} = -jk(1 - Q)u_+ \quad (1.15)$$

$$\frac{\partial u_-}{\partial r} = -jk(1 + Q)u_-, \quad (1.16)$$

where u_+ and u_- correspond to the forward and backward propagating waves, respectively. Assuming that the backward propagating part of the wave is negligible so that all the energy propagates in the forward direction the wave equation will have a solution given by

$$u(r + \Delta r, z) = e^{jk\Delta r(-1+Q)}u(r, z). \quad (1.17)$$

This equation can be solved by marching techniques given the initial vertical field profile at a desired initial range, and the necessary boundary conditions on the bottom and top of the domain. The bottom of the domain is the sea/air interface usually taken as a perfect electric conductor (PEC) boundary layer. The top is an open infinite boundary condition so the artificially created domain truncation will require an absorbing boundary condition to prevent the signal going upwards from reflecting back into the region of interest.

The simplest approximation of (1.15) is obtained by using the first order Taylor series expansions of the square root and exponential functions.

$$Q = \sqrt{1 + Z} \simeq 1 + \frac{Z}{2} \quad (1.18)$$

This yields the standard parabolic equation (SPE)

$$\frac{\partial^2 u(r, z)}{\partial z^2} + 2jk \frac{\partial u(r, z)}{\partial r} + k^2(n^2(r, z) - 1)u(r, z) = 0. \quad (1.19)$$

Note that (1.19) is exactly the same as the original equation (1.9) with the first term dropped. This is because all the intermediate steps and approximations covered above can be combined into a single narrow-angle condition called the paraxial or parabolic approximation where

$$2k \left| \frac{\partial u}{\partial r} \right| \gg \left| \frac{\partial^2 u}{\partial r^2} \right|, \quad (1.20)$$

which results in the cancelation of the first term in (1.9). Therefore, to approximate the wave equation in this parabolic equation form the following conditions must be satisfied [14]:

1. The equation is only valid within a narrow beam geometry called the paraxial cone, typically not more than 10° . The first order error term associated with increased propagation angle is proportional to $\sin^4 \alpha$, where α is the angle between the propagation direction and the horizontal paraxial direction r . This error term will increase with α as 10^{-7} , 10^{-3} , and over 10^{-2} for 1° , 10° , and 20° , respectively. More computationally expensive wider angle schemes can be implemented using the Padé coefficients however lower atmospheric duct calculations will typically require an angle less than 0.5° (see Fig. 1.5) making the fast narrow angle code preferable to wide angle finite difference schemes.
2. The field is valid only in the far-field, not close to the source.
3. The medium is only weakly inhomogeneous such as the part-per-million changes involved here.
4. Most of the energy should be propagating forward without any significant back scattering.

Equation (1.17) can be marched using the split-step fast Fourier transform (FFT) method, where $u(r, z)$ and $U(r, p)$ are Fourier transform pair related by

$$U(r, p) = \mathfrak{F} \{u(r, z)\} = \int_{-z_{\max}}^{z_{\max}} u(r, z) e^{-jpz} dz \quad (1.21)$$

$$u(r, z) = \mathfrak{F}^{-1} \{U(r, p)\} = \frac{1}{2\pi} \int_{-p_{\max}}^{p_{\max}} u(r, z) e^{jpz} dp, \quad (1.22)$$

where the transform variable is defined by $p = k \sin \alpha$, and the domain truncation height is related to p_{\max} using the Nyquist criteria $z_{\max} p_{\max} = N\pi$, N being the FFT size. Taking the FFT of the SPE (1.19) one can compute the closed form

solution for $U(r, p)$ as

$$-p^2 U(r, p) - 2jk \frac{\partial U(r, p)}{\partial r} + k^2(n^2 - 1)U(r, p) = 0 \quad (1.23)$$

$$U(r, p) = e^{-jp^2 r/(2k)} \cdot e^{jk(n^2-1)r/2}, \quad (1.24)$$

which will result in a marching solution of

$$u(r + \Delta r, z) = e^{jk(n^2-1)\Delta r/2} \mathfrak{F}^{-1} \left\{ e^{-jp^2 \Delta r/(2k)} \mathfrak{F} \{u(r, z)\} \right\}. \quad (1.25)$$

An important step is the inclusion of the correction term in the first exponential due to the earth flattening transformation. This will replace n^2 with the modified index of refraction m^2 where

$$m(r, z) = n(r, z)e^{(z/a)} \simeq n + \frac{z}{a}, \quad 0 \leq n - 1 \ll 1, \quad z \ll a \quad (1.26)$$

$$M(r, z) = \left[n(r, z) - 1 + \frac{z}{a} \right] \times 10^6 \quad (1.27)$$

$$m^2 - 1 \simeq 2(m - 1) = 2M(r, z) \times 10^{-6}. \quad (1.28)$$

Although not critical for our case, a final improvement in (1.25) is obtained by using a slightly improved wide angle approximation given in [13]. This will finally result in the split-step FFT parabolic equation used throughout this dissertation with a marching step given by

$$u(r + \Delta r, z) = \exp \left[ik_o \Delta r M(r, z) 10^{-6} \right] \times \mathfrak{F}^{-1} \left\{ \exp \left[i \Delta r \left(\sqrt{k^2 - p^2} - k \right) \right] \mathfrak{F} \{u(z, r)\} \right\}. \quad (1.29)$$

A normalized Gaussian antenna pattern is used here as the starter field with

$$U(r_o, p) = e^{-p^2 w^2/4} \quad (1.30)$$

$$w = \frac{\sqrt{2 \ln 2}}{k \sin \left(\frac{\alpha_{BW}}{2} \right)} \quad (1.31)$$

where α_{BW} is the half power beamwidth. A launch angle other than the horizontal is achieved by simply replacing $U(r_o, p)$ with $U(r_o, p - p_o)$, with $p_o = k \sin \alpha_o$.

It should be noted that at high altitudes the earth flattening transformation given here becomes less accurate. Moreover, the modified index of refraction

becomes large at high altitudes making the narrow-angle scheme inaccurate at more than a few kilometers. However, the form given in (1.29) totally satisfies all accuracy needs of the lower atmospheric narrow-angle ducted propagation environments simulated in this work.

1.3.2 Radar Sea Clutter Calculation Under Non-Standard Propagation Conditions

Using the classical radar equation, received radar clutter power can be written as

$$P_c = \frac{P_t G_t^2 \lambda^2 F^4 \sigma}{(4\pi)^3 R^4}, \quad (1.32)$$

where P_t is the transmitter power, G_t is the transmit antenna gain, λ is the wavelength, σ is the sea surface radar cross section (RCS), R is the range, and F is the propagation factor (ratio of the electric field at a point to that which would have been created by the same system operating in free space with the on-axis gain of the antenna) [15]. After F is calculated at the effective scattering height given as 0.6 times the mean wave height [16], the one-way propagation loss L then can be written as

$$L = L_{fs}/F^2 \quad (1.33)$$

$$L_{fs} = \frac{(4\pi R)^2}{\lambda^2}, \quad (1.34)$$

where L_{fs} is the free space loss. Sea surface RCS can be written as $\sigma = A_c \sigma^o$, where A_c is the illuminated area (proportional to R at small grazing angles) and σ^o is the normalized sea surface radar cross section (RCS). Then the clutter power can be written as

$$P_c = \frac{P_t G_t^2 4\pi A_c \sigma^o}{L^2 \lambda^2} \quad (1.35)$$

$$P_c = \frac{C \sigma^o R}{L^2} \quad (1.36)$$

$$P_{c,dB} = -2L_{dB} + \sigma^o(R)_{dB} + 10 \log_{10}(R) + C_{dB}, \quad (1.37)$$

where C accounts for all the constant terms [17].

In reality, both σ° and F are functions of grazing angle, the effective clutter height (which itself is a function of average wave height at the sea), range and duct parameters. Hence, they can only be accurately calculated after the forward model run with the additional knowledge of wind speed and direction. There are various models such as the Georgia Institute of Technology model (GIT) and hybrid model (HYB) and in present codes such as the Advanced Refractive Effects Prediction System (AREPS), a modified GIT is used [1, 16, 18].

The grazing angle Ψ_o dependence for vertical polarization is still an active research subject. It is not easy to determine the exact nature of the dependence of the sea surface RCS to the grazing angle and dependencies between Ψ_o^0 and Ψ_o^4 are reported in the literature [19, 20]. However, one main problem is that many of these studies are done under conditions where either there is no ducting or where there is no information about the duct. In his evaporation duct height inversion paper [21], Rogers *et al.* report that while the data did not provide a definitive answer to the grazing angle dependency problem, the use of $\sigma^\circ \propto \Psi_o^0$ generated the best results in his duct height estimation algorithm.

One interesting difference of a ducted environment relative to the standard atmospheric conditions is that, as the electromagnetic wave gets trapped and propagates inside the duct, the surface grazing angle converges to a constant value. This phenomenon is very unlike the $1/R$ variation of Ψ_o with respect to the range that would be observed in a low-angle non-ducting atmosphere. Hence, regardless of the assumed dependence of the sea surface RCS on the grazing angle, the grazing angle and hence σ° will become constant under ducting conditions after a certain range value. This assumes similar conditions such as the wind profile throughout the desired range interval. To show this, an electromagnetic ray-tracing is performed to observe the dependence of Ψ_o on the ducting conditions as a function of range as given in Fig. 1.5. It can clearly be seen that for long ranges the grazing angle is almost constant and the minimum range where one can assume a constant

Ψ_o decreases as the strength of the duct increases.

Combining this fact with the observations given in [21] (that $\sigma^o \propto \Psi_o^0$, *i.e.* independent, or at most weakly dependent), one could arguably state that range-dependence of σ^o in (1.37) can be dropped if only the power clutter at ranges larger than a R_{min} is used in the inversion. This value is selected to be 12 km in [21] and a value of 10 km has been used throughout this dissertation.

One other practical problem is the level of the clutter signal at longer ranges. The Space Range Radar (SPANDAR) used to measure the radar clutter in the Wallops Island experiments used in this thesis is a high power, high gain system relative to a sea-borne naval radar. It can achieve typically a 40 dB clutter-to-noise ratio (CNR) at 10 km range with CNR dropping to 0 dB anywhere between 30 to 50 km for an evaporation duct environment depending on various other conditions such as the wind and ducting strength. An average naval system will probably have a 0 dB CNR at 20-25 km. This value is typically much higher in surface-based duct cases. This limits the maximum range of the clutter that can be used in the inversion. R_{max} values of 25 km and 60 km (the main reason for the selection of 60 km in the SBD case is because the helicopter measurements are limited to 0-60 km range, not the lack of clutter power) are selected for the evaporation and surface-based ducts, respectively, throughout this dissertation.

To summarize, the main issue here in a practical system will be the selection of ranges which will be used in the inversion. Short ranges are preferred since at close ranges the returned clutter is larger (high CNR), whereas constant grazing angle assumption is more accurate at longer ranges. The selected values will also strongly depend on the radar parameters, especially its height, power and gain and the mean environment the radar will be operating in. Depending on the system, GIT or modified GIT clutter models may be more accurate than the assumptions used in this work. Ranges between 10-25 km and 10-60 km are used in this dissertation for the evaporation duct inversions and the surface-based duct inversions, respectively.

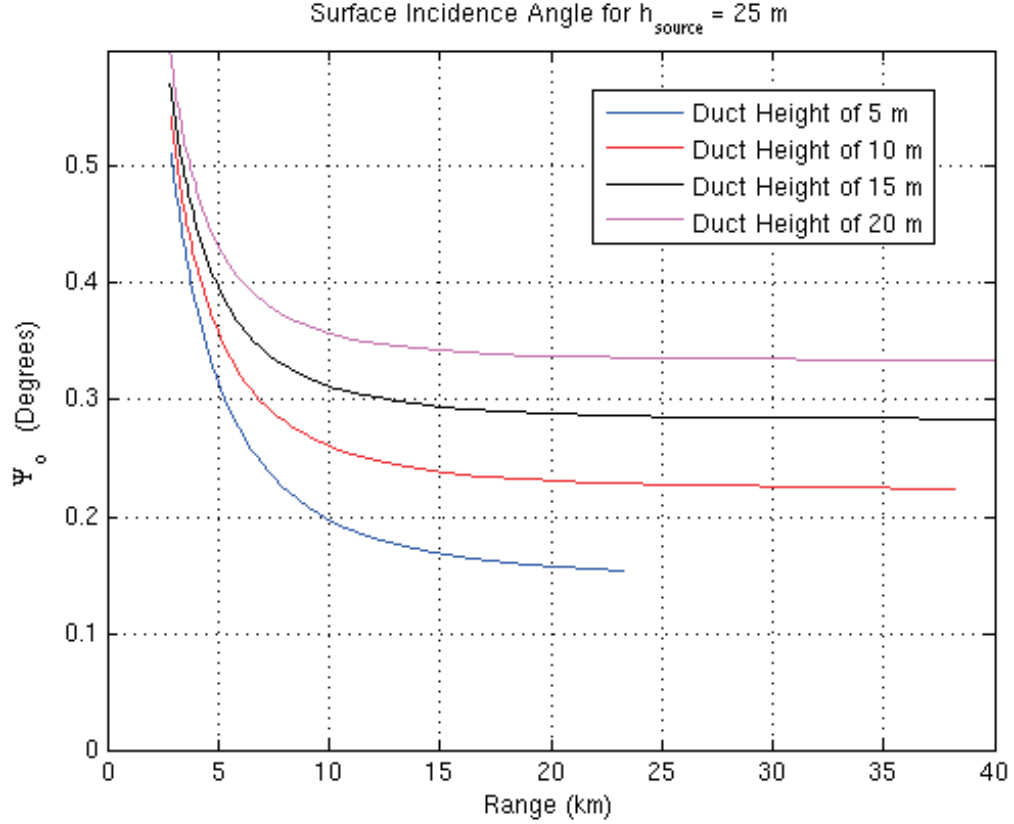


Figure 1.5: Sea surface grazing angle as a function of range for different evaporation duct heights computed using ray-tracing.

1.4 Statistical Estimation and Tracking

A Bayesian framework was adopted throughout this dissertation. All the environmental parameters were selected as random variables with posterior probability density functions (pdf's). This statistical estimation allowed the projection of the environmental probabilities into the pdf's of parameters-of-interest as shown in Fig. 1.6. Measured data \mathbf{d} , which is the radar clutter return, is mapped into a posterior distribution $p(\mathbf{m}|\mathbf{d})$ of environmental duct parameters \mathbf{m} . The environmental parameters are then mapped into the usage domain U as $p(\mathbf{u}|\mathbf{d})$ via Monte Carlo integration. \mathbf{u} typically constitutes the propagation factor (F) or the one-way transmission loss (L) so that $p(\mathbf{u}|\mathbf{d})$ can be used in radar calculations such as the detection probability (P_D), two-dimensional coverage diagrams and the false

alarm rate.

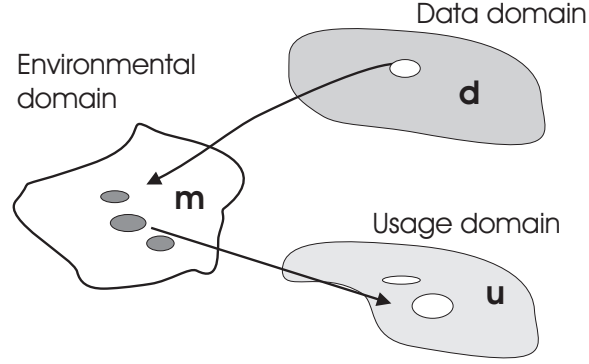


Figure 1.6: An observation d is mapped into a distribution of environmental parameters m that potentially could have generated it. These environmental parameters are then mapped into the usage domain u .

The list of techniques used in this work are given as below. Each of these techniques is summarized in their prospective chapters.

- Genetic Algorithms (GA)
- Simulated Annealing (SA)
- Metropolis-Hastings (MCMC) Sampler
- Gibbs (MCMC) Sampler
- Hybrid GA-MCMC Sampler
- Extended Kalman Filter (EKF)
- Unscented Kalman Filter (UKF)
- Sequential Importance Resampling Particle Filter (SIR-PF)

1.5 Scope of This Dissertation

The major contents of this dissertation consist of three chapters, Chapters 2 to 5¹. The first two of these chapters deals with the statistical estimation of the

¹Each chapter is essentially a full or partial reprint of papers that are published, accepted, or submitted to a professional journal. Therefore, each has been written in a paper format and is self-contained.

atmospheric index of refraction while Chapter 5 covers the spatial and temporal tracking of it.

Chapter 2 is devoted to the analysis of the RFC inversion problem using different Markov chain Monte Carlo samplers (MCMC) [22]. A typical range-independent tri-linear surface-based electromagnetic duct is estimated statistically using Metropolis-Hastings [23] and Gibbs [24] samplers. The main purpose is estimating statistically the uncertainties in the environmental parameters and projecting these into the posterior probability densities of transmission loss and propagation factor using Monte Carlo integration that can be used to predict and in some cases correct the radar performance operating in such an environment. The results are checked with exhaustive search and compared with previous studies conducted using genetic algorithms [17]. The methods are then successfully tested on data collected during the Wallops Island 1998 experiment conducted by the Naval Surface Warfare Center, Dahlgren Division that included both range-dependent environmental refractivity measurements using the helicopter provided by the Applied Physics Laboratory, John Hopkins University and radar clutter maps obtained during the operation of the Space Range Radar (SPANDAR). The results showed that these methods can accurately compute the required Monte Carlo integrations but needed high number of forward model runs which are composed of propagating the electromagnetic signal in these complex environments using the split-step FFT PE method and hence are not suitable for a real or near-real time statistical RFC estimator. Moreover, inclusion of range-dependence results in an increase in the number of environmental parameters to be estimated and an increased dimension of the parameter state-space, making these algorithm even less suitable for real-time applications. This resulted in a search for techniques that would necessitate fewer forward model runs with a minimal degradation in the MCMC performance.

This problem is addressed in Chapter 3. A hybrid genetic algorithms (GA) – Markov chain Monte Carlo method [25] based on the nearest neighborhood algorithm proposed in [26, 27] is implemented. This method uses a Voronoi

decomposition scheme that divides the entire state space into Voronoi cells, effectively discretizing the entire multi-dimensional state space. These cells are centered around the set of samples obtained from the entire set of generations of populations of the preceding genetic algorithms run. This creates an approximation to the environmental posterior density, which subsequently is resampled by a MCMC sampler such as the Gibbs algorithm to accurately compute the necessary MC integrals. This method removes computation of the forward model during the resampling MCMC phase and can result in a large reduction in the forward model runs required. The hybrid method is compared with the classical MCMC samplers used in the previous chapter. The results showed that accurate MC integrals can be computed using much smaller set of GA samples. Then the method is successfully used to estimate an range-dependent inversion of the environment in the Wallops Island 1998 experiment data.

Chapter 4 treats the RFC problem as a real-time tracking problem [28–31]. The purpose is to perform a real-time tracking of the three dimensional environment within a circular radius centered on the radar system. This requires both temporal and spatial tracking of the environmental parameters. The problem is non-linear due to the split-step FFT PE and usually non-Gaussian due to the prior densities obtained from either inversions performed in Chapters 2 and 3 or from some other source such as the regional statistics or COAMPS forecasts. Moreover, the strength of the non-linearity depends on the environment. For example, surface-based and mixed type ducts show highly nonlinear electromagnetic propagation characteristics whereas evaporation ducts result in only mild non-linearities. This necessitates implementation and comparison of different types of tracking filters for different scenarios that are commonly encountered in maritime regions. The advantages and drawbacks of each filter and selection of the best possible filter for various environmental conditions are addressed. Three filters, namely the extended Kalman (EKF), unscented Kalman (UKF), and particle filters (PF), are used [32]. The Sequential Importance Resampling (SIR) algorithm is used in the

implementation of the PF. Both Kalman filters performed poorly in surface-based duct environments with high-nonlinearties. On the contrary, the PF performed well in these environments with a mean square error (MSE) converging to that predicted by the posterior Cramér-Rao lower bound (PCRLB). The Kalman filters performed much better in evaporation duct tracking applications.

Finally, Chapter 5 addresses the conclusions of this dissertation and suggestions for possible future work.

Bibliography

- [1] Space and Naval Warfare Systems Center, Atmospheric Propagation Branch, San Diego, CA. *User's Manual for Advanced Refractive Effect Prediction System*, 3.4 edition, April 2005.
- [2] Merrill I. Skolnik. *Introduction to Radar Systems*. McGraw-Hill, New York, third edition, 2001.
- [3] J. H. Richter. Sensing of radio refractivity and aerosol extinction. *IEEE Geoscience and Remote Sensing Symposium, IGARSS'94*, 1:381–385, 1994.
- [4] J. R. Rowland and S. M. Babin. Fine-scale measurements of microwave profiles with helicopter and low cost rocket probes. *Johns Hopkins APL Tech. Dig.*, 8 (4):413–417, 1987.
- [5] J. H. Richter. High resolution tropospheric radar sounding. *Radio Science*, 4(12):1261–1268, 1969.
- [6] Cory A. Springer. The gouge on COAMPS: What is it? why use it? how to use it. *Naval Meteorology & Oceanography Command News*, 19(2), 1999.
- [7] Naval Research Laboratory, Monterey Marine Metrology Division. *Coupled Ocean/Atmosphere Mesoscale Prediction System (COAMPS) Web Page*, 3.1.1 edition, 2004.
- [8] Adam Willitsford and C. R. Philbrick. Lidar description of the evaporative duct in ocean environments. volume 5885. Proceedings of SPIE, Bellingham, WA, September 2005.
- [9] Anthony R. Lowry, Chris Rocken, Sergey V. Sokolovskiy, and Kenneth D. Anderson. Vertical profiling of atmospheric refractivity from ground-based GPS. *Radio Science*, 37(3):1041–1059, 2002. doi:10.1029/2000RS002565.
- [10] H. W. Ko, J. W. Sari, and J. P. Skura. Anomalous wave propagation through atmospheric ducts. *Johns Hopkins APL Tech. Dig.*, 4:12–26, 1983.
- [11] G. D. Dockery. Modeling electromagnetic wave propagation in the troposphere using the parabolic equation. *IEEE Trans. Antennas Propagat.*, 36 (10):1464–1470, 1988.

- [12] Amalia E. Barrios. Parabolic equation modeling in horizontally inhomogeneous environments. *IEEE Trans. Antennas Propagat.*, 40 (7):791–797, 1992.
- [13] Amalia E. Barrios. A terrain parabolic equation model for propagation in the troposphere. *IEEE Trans. Antennas Propagat.*, 42 (1):90–98, 1994.
- [14] M. Levy. *Parabolic Equation Methods for Electromagnetic Wave Propagation*. The Institution of Electrical Engineers, London, United Kingdom, 2000.
- [15] David Barton. *Modern Radar System Analysis*. Artech House, Norwood, MA, 1988.
- [16] J. P. Reilly and G. D. Dockery. Influence of evaporation ducts on radar sea return. *IEE Proc. Radar and Signal Processing*, 137 (F–2):80–88, 1990.
- [17] Peter Gerstoft, L. T. Rogers, J. Krolik, and W. S. Hodgkiss. Inversion for refractivity parameters from radar sea clutter. *Radio Science*, 38 (3):1–22, 2003. doi:10.1029/2002RS002640.
- [18] G. D. Dockery. Method of modelling sea surface clutter in complicated propagation environments. *IEE Proceedings*, 137 (F–2):73–79, 1990.
- [19] D. E. Barrick. Grazing angle behavior of scatter and propagation above any rough surface. *IEEE Trans. Antennas Propagat.*, 46(1):73–83, 1998.
- [20] V. I. Tatarski and Charnotskii M. On the behaviour of scattering from a rough surface for small grazing angles. *IEEE Trans. Antennas Propagat.*, 46(1):67–72, 1998.
- [21] L. Ted Rogers, C. P. Hattan, and J. K. Stapleton. Estimating evaporation duct heights from radar sea echo. *Radio Science*, 35 (4):955–966, 2000. doi:10.1029/1999RS002275.
- [22] Caglar Yardim, Peter Gerstoft, and William S. Hodgkiss. Estimation of radio refractivity from radar clutter using Bayesian Monte Carlo analysis. *IEEE Trans. Antennas Propagat.*, 54(4):1318–1327, 2006.
- [23] N. Metropolis, A. W. Rosenbluth, M. N. Rosenbluth, A. H. Teller, and E. Teller. Equation of state calculations by fast computing machines. *J. of Chemical Physics*, 21:1087–1092, 1953.
- [24] S. Geman and D. Geman. Stochastic relaxation, Gibbs distributions, and the Bayesian restoration of images. *IEEE Trans. Pattern Anal. Machine Intell.*, 6:721–741, 1984.
- [25] Caglar Yardim, Peter Gerstoft, and William S. Hodgkiss. Statistical maritime radar duct estimation using a hybrid genetic algorithms – Markov chain Monte Carlo method. *Radio Science*, in press.

- [26] Malcolm Sambridge. Geophysical inversion with a neighborhood algorithm - I. searching a parameter space. *Geophys. J. Int.*, 138:479–494, 1999.
- [27] Malcolm Sambridge. Geophysical inversion with a neighborhood algorithm - II. appraising the ensemble. *Geophys. J. Int.*, 138:727–746, 1999.
- [28] Caglar Yardim, Peter Gerstoft, and William S. Hodgkiss. Tracking refractivity from clutter. *IEEE Trans. Antennas Propagat.*, submitted.
- [29] Caglar Yardim, Peter Gerstoft, and William S. Hodgkiss. Atmospheric refractivity tracking from radar clutter using Kalman and particle filters. IEEE Radar Conference, Boston, MA, April 2007.
- [30] Caglar Yardim, Peter Gerstoft, and William S. Hodgkiss. Tracking atmospheric ducts using radar clutter: I. evaporation duct tracking using Kalman filters. IEEE APS Conference, Honolulu, Hawaii, June 2007.
- [31] Caglar Yardim, Peter Gerstoft, and William S. Hodgkiss. Tracking atmospheric ducts using radar clutter: II. surface-based duct tracking using multiple model particle filters. IEEE APS Conference, Honolulu, Hawaii, June 2007.
- [32] Branko Ristic, Sanjeev Arulampalam, and Neil Gordon. *Beyond the Kalman Filter, Particle Filters for Tracking Applications*. Artech House, Boston, 2004.

Estimation of Radio Refractivity from Radar Clutter Using Bayesian Monte Carlo Analysis

This paper describes a Markov Chain Monte Carlo sampling approach for the estimation of not only the radio refractivity profiles from radar clutter but also the uncertainties in these estimates. This is done by treating the Refractivity From Clutter (RFC) problem in a Bayesian framework. It uses unbiased Markov Chain Monte Carlo (MCMC) sampling techniques, such as Metropolis and Gibbs sampling algorithms, to gather more accurate information about the uncertainties. Application of these sampling techniques using an electromagnetic split-step fast Fourier transform parabolic equation propagation model within a Bayesian inversion framework can provide accurate posterior probability distributions of the estimated refractivity parameters. Then these distributions can be used to estimate the uncertainties in the parameters-of-interest. Two different MCMC samplers (Metropolis and Gibbs) are analyzed and the results are compared not only with the exhaustive search results but also with the genetic algorithm (GA) results and helicopter refractivity profile measurements. Although it is slower than global optimizers, the probability densities obtained by this method are closer to

the true distributions.

2.1 Introduction

An accurate knowledge of radio refractivity is essential in many radar and propagation applications. Especially at low altitudes, radio refractivity can vary considerably with both height and range, heavily affecting the propagation characteristics. One important example is the formation of an electromagnetic duct. A signal sent from a surface or low altitude source, such as a ship or low-flying object, can be totally trapped inside the duct. This will result in multiple reflections from the surface and they will appear as clutter rings in the radar PPI screen (Fig. 2.1). In such cases, a standard atmospheric assumption with a slope of modified refractivity of 0.118 M-units/m may not give reliable predictions for a radar system operating in such an environment.

Ducting is a phenomenon that is encountered mostly in sea-borne applications due to the abrupt changes in the vertical temperature and humidity profiles just above large water masses, which may result in an sharp decrease in the modified refractivity (M-profile) with increasing altitude. This will, in turn, cause the electromagnetic signal to bend downward, effectively trapping the signal within the duct. It is frequently encountered in many regions of the world such as the Persian Gulf, the Mediterranean and California. In many cases, a simple tri-linear M-profile is used to describe this variation. The coverage diagram of a trapped signal in such an environment is given in Fig. 2.2.

The first attempt in estimating the M-profile from radar clutter returns using a maximum likelihood (ML) approach was made in [1] and was followed by similar studies, which used either a marching-algorithm approach [2] or the global-parametrization approach [3, 4]. The later is adopted in this work. The main purpose of these studies is to estimate the M-profile using only the radar clutter return, which can readily be obtained during the normal radar operation, without

requiring any additional measurements or hardware. A near-realtime estimation can be achieved with a sufficiently fast optimizer. Moreover, information obtained from other sources can be easily incorporated into the Bayesian formulation, *e.g.* the statistics of M-profiles in the region, meteorological model simulation results, helicopter, radiosonde or some other ship-launched *in situ* instrument measurements.

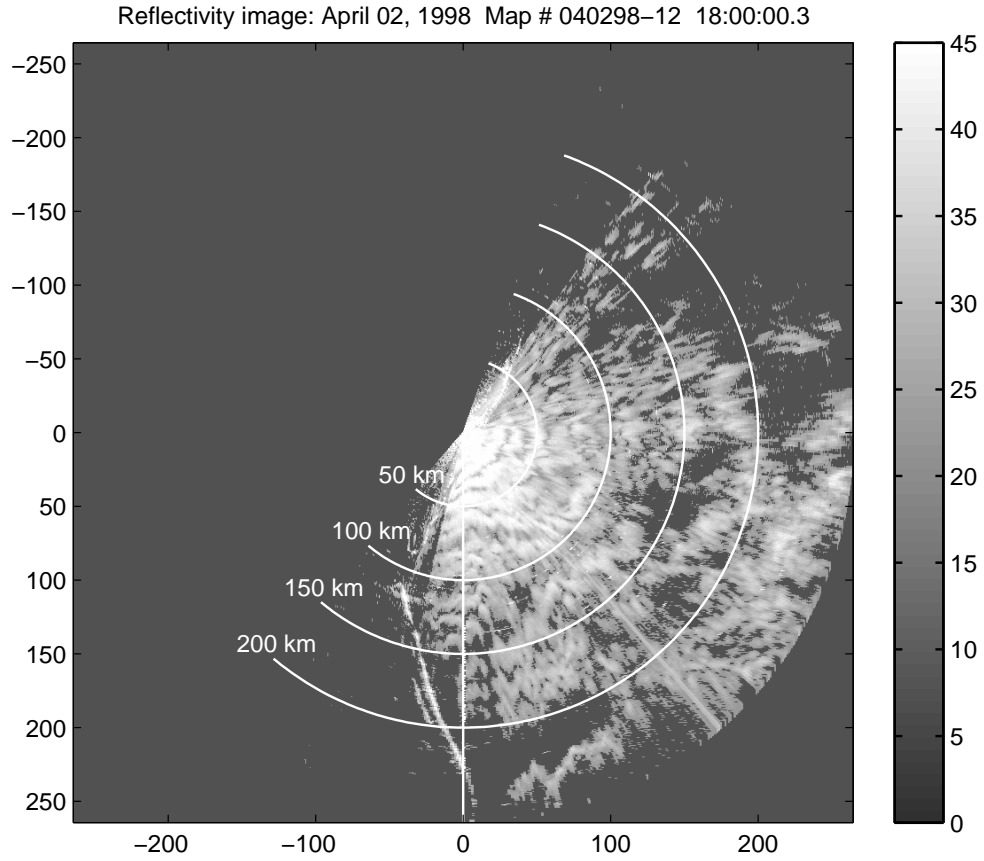


Figure 2.1: Clutter map from Space Range Radar (SPANDAR) at Wallops Island, VA.

To address the uncertainties in the M-profile parameter estimates, determination of the basic quantities such as the mean, variance and marginal posterior probability distribution of each estimated parameter is necessary. They can be computed by taking multi-dimensional integrals of the posterior probability den-

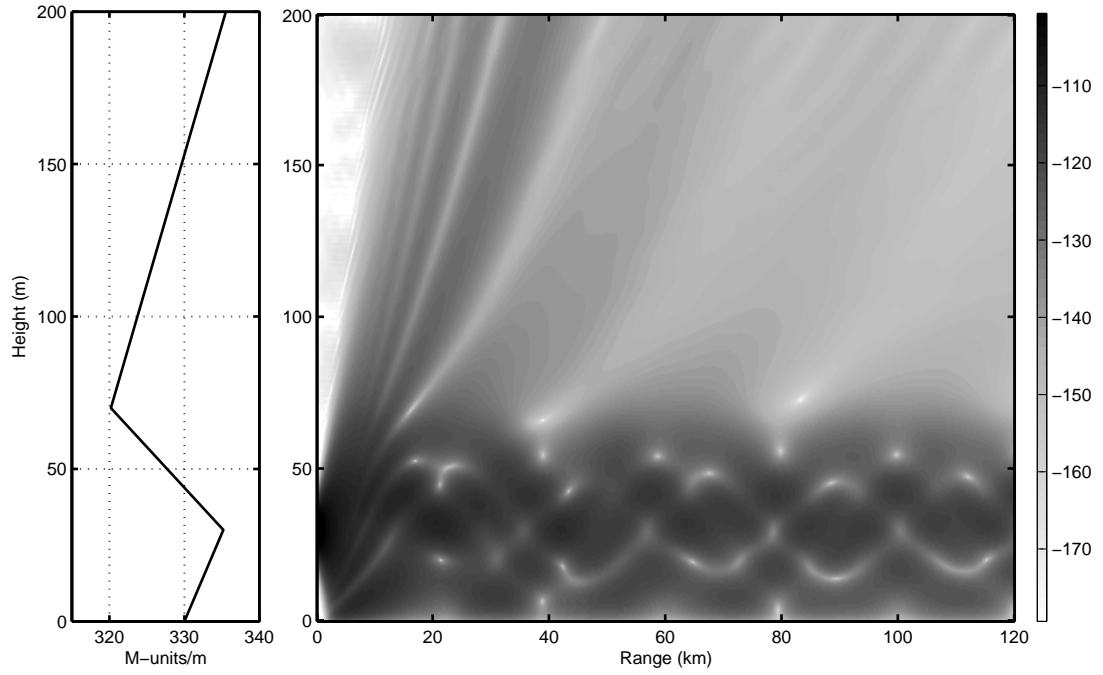


Figure 2.2: Tri-linear M-profile and its corresponding coverage diagram.

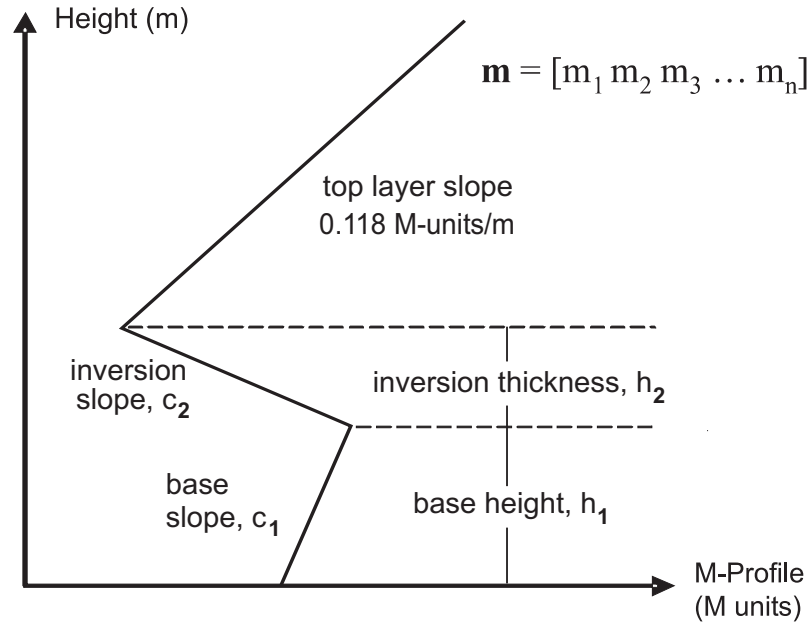


Figure 2.3: The 4-parameter tri-linear M-profile model used in this work.

sity (PPD), which can be accomplished by a Markov Chain Monte Carlo (MCMC) sampling method within a Bayesian inversion structure. MCMC is selected because it provides unbiased sampling of the PPD, unlike global optimizers such as the genetic algorithm, which usually over-sample the peaks of the PPD and introduce a bias [5].

Bayesian inversion is a likelihood-based technique which, when combined with a powerful sampling algorithm such as MCMC, can be an effective tool in the estimation of uncertainty in non-linear inversion problems such as the electromagnetic refractivity from clutter (RFC) inversion. An alternative approach, which does not make use of likelihood is given in [6]. The likelihood formulations are based on those used in [7]. The MCMC sampler employs a split-step FFT parabolic equation code as its forward propagation model.

2.2 Theory

The M-profile is assumed range-independent and a simple tri-linear profile is used to model the vertical M-profile (Fig. 2.3). An M-profile with n parameters is represented by the vector \mathbf{m} , with the element m_i being the value of the i^{th} parameter. Each of these environmental parameters is then treated as an unknown random variable. Therefore, an n -dimensional joint posterior probability density function (PPD), can be defined using all of the parameters. All of the desired quantities such as the means, variances and marginal posterior distributions can be found using the PPD. A summary of the notation used is given in Table 2.1.

The n -parameter refractivity model \mathbf{m} is given to a forward model, an electromagnetic split-step FFT parabolic equation, along with the other necessary input parameters such as frequency, transmitter height, beamwidth, antenna beam pattern [8,9]. The forward model propagates the field in a medium characterized by \mathbf{m} and outputs the radar clutter $f(\mathbf{m})$. This is then compared with the measured clutter data \mathbf{d} and an error function $\phi(\mathbf{m})$ is derived for the likelihood function.

In previous global-parametrization approaches, this error function was used by a global optimization algorithm such as the genetic algorithm (GA), which would minimize $\phi(\mathbf{m})$ and reach the maximum likelihood (ML) solution. Instead of GA, a likelihood function based on $\phi(\mathbf{m})$ can be used in a Metropolis or Gibbs sampler. This makes it possible to get not only the ML solution but also better estimates for the uncertainties in terms of variances, marginal and multi-dimensional PPD's.

2.2.1 Bayesian Inversion

RFC can be solved using a Bayesian framework, where the unknown environmental parameters are taken as random variables with corresponding 1-D probability density functions (pdf) and a n -dimensional joint pdf. This probability function can be defined as the probability of the model vector \mathbf{m} given the experimental data vector \mathbf{d} , $p(\mathbf{m}|\mathbf{d})$, and it is called the posterior pdf (PPD). \mathbf{m} with the highest probability is referred to as the maximum *a posteriori* (MAP) solution. For complex probabilities, global optimizers such as the genetic algorithm or simulated annealing can be used to find the MAP solution. An alternative to this is minimizing the mean square error between clutter data \mathbf{d} and the reconstructed clutter $f(\mathbf{m})$. It is referred to as the Bayesian minimum mean square error (MMSE) estimator and can easily be shown to be equal to the vector mean of $p(\mathbf{m}|\mathbf{d})$ [10]. Both estimates are calculated in this work. Due to the fact that a non-informative prior is used, MAP and ML solutions are the same and will be referred simply as ML from now on. The posterior means, variances and marginal probability distributions then can be found by taking n - or $(n - 1)$ -dimensional integrals of this PPD.

$$\mu_i = \int \dots \int_{\mathbf{m}'} m'_i p(\mathbf{m}'|\mathbf{d}) d\mathbf{m}' \quad (2.1)$$

$$\sigma_i^2 = \int \dots \int_{\mathbf{m}'} (m'_i - \mu_i)^2 p(\mathbf{m}'|\mathbf{d}) d\mathbf{m}' \quad (2.2)$$

$$p(m_i|\mathbf{d}) = \int \dots \int_{\mathbf{m}'} \delta(m'_i - m_i) p(\mathbf{m}'|\mathbf{d}) d\mathbf{m}' \quad (2.3)$$

Posterior density of any specific environmental parameter such as the M-deficit or the duct height can be obtained by marginalizing the n -dimensional PPD as given in (2.3). Joint probability distributions can be obtained using similar integrations. For further details about Bayesian inverse theory see [10, 11].

The posterior probability can be found using Bayes' formula:

$$p(\mathbf{m}|\mathbf{d}) = \frac{\mathcal{L}(\mathbf{m})p(\mathbf{m})}{p(\mathbf{d})} \quad (2.4)$$

with

$$p(\mathbf{d}) = \int_{\mathbf{m}} p(\mathbf{d}|\mathbf{m})p(\mathbf{m})d\mathbf{m}. \quad (2.5)$$

The likelihood function $\mathcal{L}(\mathbf{m})$ will be defined in the next section. The prior $p(\mathbf{m})$ represents the *a priori* knowledge about the environmental parameters, \mathbf{m} , before the experiment. Therefore, it is independent of the experimental results and hence, \mathbf{d} . The evidence appears in the denominator of the Bayes' formula as $p(\mathbf{d})$. It is the normalizing factor for $p(\mathbf{m}|\mathbf{d})$ and it is independent of the parameter vector \mathbf{m} . A non-informative or flat prior assumption will reduce (2.4) to

$$p(\mathbf{m}|\mathbf{d}) \propto \mathcal{L}(\mathbf{m}) \quad (2.6)$$

2.2.2 Likelihood Function

Assuming a zero-mean Gaussian-distributed error, the likelihood function can be written as

$$\begin{aligned} \mathcal{L}(\mathbf{m}) &= (2\pi)^{-N_R/2} |\mathbf{C}_d|^{-1/2} \\ &\times \exp \left[-\frac{(\mathbf{d} - f(\mathbf{m}))^T \mathbf{C}_d^{-1} (\mathbf{d} - f(\mathbf{m}))}{2} \right], \end{aligned} \quad (2.7)$$

where \mathbf{C}_d is the data covariance matrix, $(\cdot)^T$ is the transpose and N_R is the number of range bins used (length of the data vector, \mathbf{d}). Further simplification can be achieved by assuming that the errors are spatially uncorrelated with identical distribution for each data point forming the vector \mathbf{d} . For this case, $\mathbf{C}_d = \nu \mathbf{I}$,

where ν is the variance and \mathbf{I} the identity matrix. Defining an error function $\phi(\mathbf{m})$ by

$$\phi(\mathbf{m}) = |\mathbf{d} - f(\mathbf{m})|^2 = \sum_{i=1}^{N_R} |d_i - f_i(\mathbf{m})|^2, \quad (2.8)$$

the likelihood function can be written as

$$\mathcal{L}(\mathbf{m}) = (2\pi\nu)^{-N_R/2} \exp \left[-\frac{\phi(\mathbf{m})}{2\nu} \right]. \quad (2.9)$$

Therefore, recalling (2.6), the posterior probability density can be expressed as

$$p(\mathbf{m}|\mathbf{d}) \propto \exp \left[-\frac{\phi(\mathbf{m})}{2\nu} \right]. \quad (2.10)$$

The calculation of probabilities of all possible combinations along a predetermined grid is known as the exhaustive search and practically can be used for up to 4 – 5 parameters, depending on the forward modeling CPU speed. However, as n increases further it becomes impractical. Therefore, there is a need for an effective technique that can more efficiently estimate not only the posterior probability distribution but also the multi-dimensional integrals given in (2.1) – (2.3).

2.2.3 Markov Chain Monte Carlo Sampling

MCMC algorithms are mathematically proven to sample the n -dimensional state space in such a way that the PPD obtained using these samples will asymptotically be convergent to the true probability distribution. There are various implementations of MCMC such as the famous Metropolis-Hastings (or simplified Metropolis version) algorithm, which was first introduced in [12] and Gibbs sampling, which was made popular among the image processing community by [13]. They are extensively used in many other fields such as geophysics [11] and ocean acoustics [5, 14, 15].

To have asymptotic convergence in the PPD, a Markov chain sampler must satisfy the “Detailed Balance” [16]. Markov chains with this property are also called reversible Markov chains and it guarantees the chain to have a stationary distribution. MCMC samplers satisfy this detailed balance. Moreover, we can

set up the MCMC such that the desired distribution (PPD) is the stationary distribution. Hence, the sample distribution will converge to the PPD as more and more samples are collected. Global optimizers do not satisfy detailed balance and they usually over-sample the high probability regions since they are designed as point estimators, trying to get to the optimal solution point fast, not to wander around the state space to sample the distribution. On the contrary, an unbiased sampler following MCMC rules will spend just enough time on lower probability regions and the histogram formed from the samples will converge to the true distribution.

Metropolis and Gibbs samplers are selected as the MCMC algorithms to be used here. The working principle for both methods is similar. Assume the i^{th} sample is $\mathbf{m}^i = [m_1^i \ m_2^i \dots \ m_n^i]$. In the n -dimensional parameter space, new MCMC samples are obtained by drawing from n successive 1-D densities. Selection of the next MCMC sample $\mathbf{m}^{i+1} = [m_1^{i+1} \ m_2^{i+1} \dots \ m_n^{i+1}]$ starts with fixing all coordinates except the first one. Then the intermediate point $[m_1^{i+1} \ m_2^i \dots \ m_n^i]$ is selected by drawing a random value from a one-dimensional distribution around m_1^i . The new point, $[m_1^{i+1} \ m_2^i \dots \ m_n^i]$ is then used as the starting point to update the second parameter by drawing a value for m_2 . The next sample \mathbf{m}^{i+1} is formed when all the parameters are updated once successively. The difference between the two methods lies in the selection of the 1-D distributions.

Metropolis Algorithm

In the more general Metropolis-Hastings algorithm, the 1-D distribution can be any distribution. However, in the simplified version, called the Metropolis algorithm, the 1-D distribution has to be symmetric. The most common ones used in practice are the uniform and Gaussian distributions (A variance of $0.2 \times$ search interval is used) centered around the m_i . Likelihood is assumed to be zero outside the search interval. After each 1-D movement, the Metropolis algorithm acceptance/rejection criterion is applied. The criterion to update the j^{th} parameter

can be given as:

$$\begin{aligned}
 a &= \frac{p(m_j^{\text{proposed}})}{p(m_j^i)} \\
 m_j^{i+1} &= \begin{cases} m_j^{\text{proposed}} & (\text{Accept}), \quad \text{if } a > \text{rand}[0,1] \\ m_j^i & (\text{Reject}), \quad \text{else.} \end{cases}
 \end{aligned} \tag{2.11}$$

The probability $p(\mathbf{m}|\mathbf{d})$ for any model vector \mathbf{m} can be calculated using (2.10).

Gibbs Algorithm

For Gibbs sampling, the 1-D distribution is not any random distribution but the conditional pdf at that point itself with all other parameters fixed. Therefore, the j^{th} parameter m_j^{i+1} is drawn from the conditional pdf $p(m_j|m_1^{i+1}m_2^{i+1}\dots m_{j-1}^{i+1}m_{j+1}^i\dots m_n^i)$. For example, the first intermediate point $[m_1^{i+1} m_2^i \dots m_n^i]$ is selected by drawing from the conditional 1-D pdf obtained by fixing all m except m_1 , $p(m_1|m_2^i m_3^i \dots m_n^i)$.

There are two possible advantages in this method. First of all, this method is especially powerful in applications, where 1-D conditional pdf's are known. Secondly, since the samples are selected from the conditional pdf's instead of some random distribution, Metropolis-Hastings acceptance/rejection criterion will always accept any selected point. Unfortunately, these pdf's are not known here and are found using exhaustive search, which makes this method less attractive in RFC applications. For further details see [17] and [18].

Once the algorithm converges (see Section 3.3), we will have a set $\{\mathbf{m}_1, \mathbf{m}_2, \mathbf{m}_3, \dots, \mathbf{m}_N\}$ of N samples that will be used to form the PPD and any other desired quantity as explained in the next section.

2.2.4 Monte Carlo Integration

Monte Carlo integration method can be used to evaluate (2.1) – (2.3). Notice that all of those equations are of the form

$$I = \int g(x)p(x)dx, \quad (2.12)$$

where x is a random variable with a pdf of $p(x)$, and $g(x)$ is some function of x . Monte Carlo integration [16] states that if a large enough set of random x values are drawn from its own pdf, $\{x_1, x_2, x_3, \dots, x_N\}$, the integral can be estimated as:

$$I \approx \frac{1}{N} \sum_{i=1}^N g(x_i). \quad (2.13)$$

One of the biggest advantages of using an MCMC sampler comes from the ease at which the MCMC and the MC integration can be combined. Remembering that MCMC actually samples the n -dimensional posterior distribution, $p(\mathbf{m}|\mathbf{d})$, it will be clear that once MCMC converges, the set of MCMC samples can be directly used to calculate these multi-dimensional integrals.

2.3 Implementation

The most attractive property of the MCMC algorithm is that the result is guaranteed to converge to the true distribution when a large enough set of samples is collected. However, classical Metropolis/Gibbs sampling can be slow computationally and some modifications are needed to make it faster without affecting the end results. There are two main drawbacks of MCMC's that decrease their speed and they are discussed in the following two sections.

2.3.1 Burn-in Phase

The first drawback is related to the distance between the starting point and the high probability regions. Without any prior information, the algorithm would start from a random \mathbf{m} , which may be far from the high probability regions.

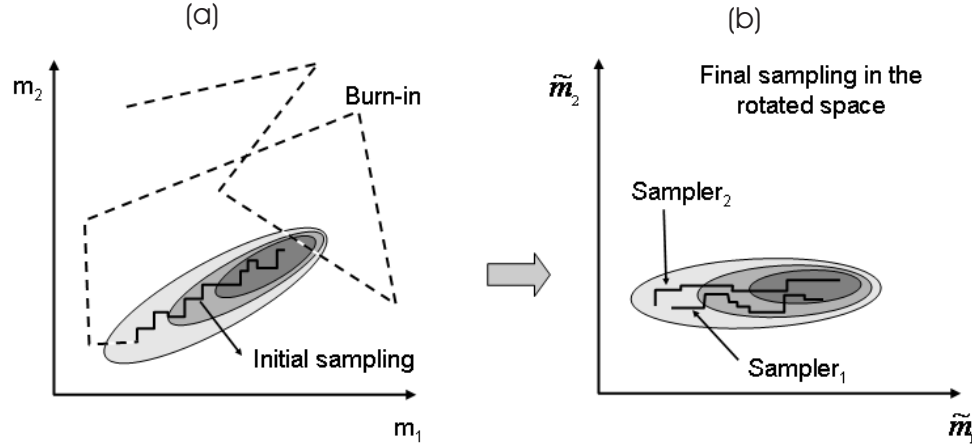


Figure 2.4: Full implementation of the MCMC algorithm: (a) burn-in and initial sampling phases in the original parameter space, and (b) two parallel-running samplers operating on the new parameter landscape after coordinate rotation.

This is a concern since, unlike a global optimizer, it may take a considerable number of iterations for the MCMC to reach the high probability regions. Hence, it must be correctly guided or initialized before the sampling is started. The classical MCMC can be modified to include an initialization phase, which is commonly referred as the “burn-in” phase (Fig. 2.4(a)). In most cases, the burn-in section itself is actually a global optimizer. A genetic algorithm (GA) or a fast cooling simulated annealing (SA) algorithm can be good candidates. Both were used here and gave good results. If a fast cooling SA is to be used, the temperature T should be lowered until it reaches $T = 1$ so that the Boltzmann distribution used for SA actually becomes the likelihood function itself at that temperature [16].

$$p_{SA}(\mathbf{m}) = \exp \left[-\frac{\phi(\mathbf{m})}{2\nu T} \right] \Rightarrow \mathcal{L}(\mathbf{m}) \quad (2.14)$$

2.3.2 Initial Sampling and Coordinate Rotation

The second drawback is based on the effects of inter-parameter correlation. Recalling that there is freedom of movement only in the directions parallel to

parameter axes, it is hard to sample highly correlated PPD's (Fig. 2.4(a)). With only vertical and horizontal movements allowed, it will take many samples to move from one end to the other of the slanted high probability areas, whereas it can be done with a much smaller number of samples in an uncorrelated case.

The remedy lies in a rotation of coordinate in the n -dimensional parameter space [19]. Instead of applying Metropolis sampling in the correlated parameter space, a new set of uncorrelated parameters are defined by applying an orthogonal coordinate transformation that diagonalizes the model covariance matrix \mathbf{C}_m . The rotation matrix \mathbf{R} is found by eigenvalue-eigenvector decomposition of \mathbf{C}_m :

$$\mathbf{C}_m = \mathbf{R} \mathbf{\Lambda} \mathbf{R}^T, \quad \tilde{\mathbf{m}} = \mathbf{R}^T \mathbf{m} \quad (2.15)$$

where $\mathbf{\Lambda}$ is a diagonal matrix containing the eigenvalues of the covariance matrix, \mathbf{R} is the orthonormal rotation matrix, whose columns contain the eigenvectors of \mathbf{C}_m and $\tilde{\mathbf{m}}$ is the rotated model vector. The model covariance matrix is found using samples drawn from the PPD after the burn-in phase. Only a small number of MCMC samples (about 1000) are enough to find \mathbf{C}_m due to its fast converging nature [5, 14]. This is referred as the initial sampling phase. After this phase, the parameter space is rotated before the final sampling phase starts.

2.3.3 Final Sampling Phase and Convergence

The final sampling phase simply is composed of two independent, parallel-running Metropolis (or Gibbs) samplers in the rotated space, sampling the same PPD (Fig. 2.4(b)). The algorithm uses a convergence criterion based on the Kolmogorov-Smirnov (K-S) statistic function D of the marginal posterior distributions [20]. $p(m_j|\mathbf{d})$'s are calculated using (2.3) as each new sample is drawn. A pair of $p(m_j|\mathbf{d})$, one from each sampler, is calculated for each parameter m_j . Then the K-S statistic is calculated for each parameter as:

$$D_j = \max_{m_j} |P_2(m_j|\mathbf{d}) - P_1(m_j|\mathbf{d})|, \quad (2.16)$$

where $P_1(m_j|\mathbf{d})$ and $P_2(m_j|\mathbf{d})$ represent the cumulative marginal distribution functions for the two parallel-running samplers. The simulation is assumed to have converged when the largest D_j term is less than ϵ ($\epsilon = 0.05$ is used here). After the convergence criterion is met, these two independent sets are combined to form a final set twice as large so that the difference between the true distribution and the estimated one is expected to be even less.

To use the likelihood equation (2.9), the error variance ν must be estimated. In this paper, an estimate for ν is calculated using an ML approach. To find the ML estimate of the variance, $\partial\mathcal{L}/\partial\nu = 0$ is solved and evaluated at the ML model estimate $\hat{\mathbf{m}}$. This results in

$$\hat{\nu} = |\mathbf{d} - f(\hat{\mathbf{m}})|^2 / N_R. \quad (2.17)$$

$\hat{\mathbf{m}}$ itself is estimated using a global optimizer, usually the value obtained at the end of the burn-in phase.

Equation (2.17) assumes the measurements at different ranges are uncorrelated, which may not be the case. Gerstoft and Mecklenbräuker [7] suggested replacing N_R with N_{eff} , number of effectively uncorrelated data points. More detailed discussion can be found in [14, 15].

Received clutter power can be calculated as given in [3], in terms of the one-way loss term L in dB as:

$$f(\mathbf{m}) = -2L + 10 \log(r) + C, \quad (2.18)$$

where C is a constant that includes wavelength, radar cross-section (RCS), transmitter power, antenna gain, etc. If these values are known, they can be included into the equation. However, one or more may be unavailable such as the mean RCS or transmitter specifications. An alternative, which is used here, is discarding these constant terms, which is done by subtracting both the mean of the replica clutter $f(\mathbf{m})$ from itself and the mean of the measured clutter \mathbf{d} from itself before inserting them into the likelihood function.

2.3.4 Post-Processing

After the MCMC sampler converges with a set of refractivity parameters $\{\mathbf{m}_1, \mathbf{m}_2, \mathbf{m}_3, \dots, \mathbf{m}_N\}$, a post-processing section is needed to convert the uncertainty in the M-profile into other parameters of interest that could be used by the radar operator, such as the propagation factor and the one-way propagation loss.

Assume an end-user parameter u , which can be expressed as a function of model parameters $u = g(\mathbf{m})$. The posterior probability distribution of u , PPD_u can be simply calculated by drawing a large amount of samples of \mathbf{m} from its own PPD and calculating $g(\cdot)$ for each one. Then this set of $g(\mathbf{m})$ can be used to obtain the PPD_u or perform any other uncertainty analysis of u using (2.1) – (2.3) and MC integration.

Since the usage of an MCMC sampler guarantees that $\{\mathbf{m}_1, \mathbf{m}_2, \mathbf{m}_3, \dots, \mathbf{m}_N\}$ is a large enough set drawn from its own PPD, this set can readily be used to obtain the statistics of u .

2.4 Examples

This section is composed of both synthetic and experimental examples. Four different algorithms, two of which are MCMC, are first tested using synthetic data generated by Terrain Parabolic Equation program (TPEM) [8]. Then the data gathered during the Wallops'98 Space Range Radar (SPANDAR) measurement is analyzed using the Metropolis sampler and GA.

2.4.1 Algorithm Validation

To validate the MCMC algorithms, a comparison with the true distribution is necessary. The true distribution can be obtained by using exhaustive search, however, it is extremely inefficient and demands a large number of forward model runs. Even if only 25 discrete possible values are assumed for each of the 4 parameters used for the model in Fig. 2.2, the state space consists of $25^4 =$

3.9×10^5 (390k) possible states. A simple range-independent tri-linear model with only 4 parameters is used since an exhaustive search would need around 10000k forward model runs for 5 parameters. The number of forward model runs needed for MCMC is proportional to the dimension size so as dimension size increases it requires much fewer samples than the exhaustive search. The selected parameters are the slope and height of the base layer (c_1 & h_1) and the slope and thickness of the inversion layer (c_2 & h_2) as shown in Fig. 2.3. Their test case values and the search bounds are given in Table 2.2. A standard atmosphere with a vertical refractivity gradient (top layer slope) of 0.118 M-units/m is assumed above the inversion layer. Parameters are selected in terms of the heights and slopes instead of the classical heights and widths (such as the frequently used inversion thickness and M-deficit) due to their relatively smaller inter-parameter correlation.

The synthetic data is generated by TPEM at a frequency of 2.84 GHz, antenna 3dB beamwidth of 0.4° , source height of 30.78 m and a radar clutter standard deviation of 10 dB, a typical value reported also in [21]. Inversion is done using four different methods for a range of 10-60 km.

The convergence characteristics of both MCMC algorithms are similar. The results of the initial sampling phase is given in Fig. 2.4.1 in terms of a convergence plot for the model covariance matrix \mathbf{C}_m . The percent error is calculated as the average absolute percent change in all matrix entries of \mathbf{C}_m as the matrix is recalculated while new samples are taken. The matrix converges quickly and for this case, only 250 samples were sufficient to have a good estimate of \mathbf{C}_m .

After the rotation matrix is obtained, two independent Metropolis/Gibbs algorithms run during the final sampling phase until the convergence criterion given in Section 3.3 is met (Fig. 2.6). Dosso [5] reported convergence in 7×10^5 (700k) forward models with a Gibbs sampler and around 100k with a fast Gibbs sampler (FGS). Similarly, Battle *et al.* [15] reported convergence in 63k models using a less strict convergence criterion, again with a FGS. Due to the modifications in the Metropolis/Gibbs algorithms used here, they also can be classified as “fast”

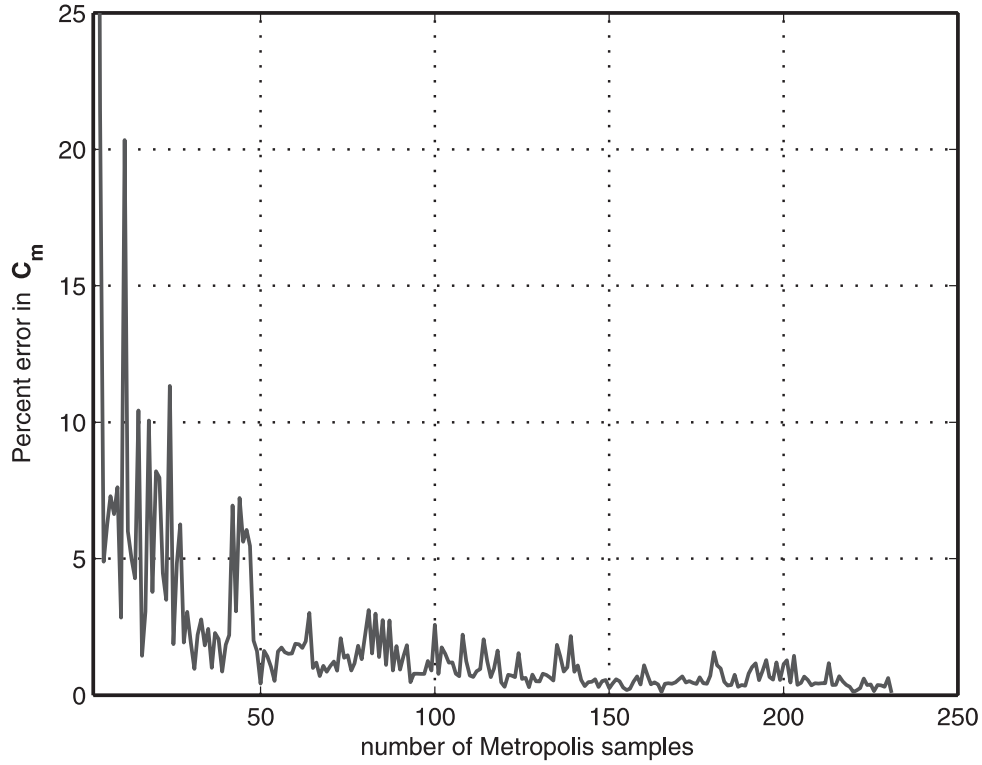


Figure 2.5: Initial sampling phase - convergence of the model covariance matrix in terms of percent error. \mathbf{C}_m later will be used for coordinate rotation.

samplers. Therefore, a typical value of 100k models is in agreement with the previous applications of MCMC algorithms. During the simulations, values as low as 20k models and higher than 150k models were encountered.

The marginal distributions of the four parameters are given Fig. 2.7. Except for exhaustive search, the results for all others are calculated using the MC integration. The exhaustive search result (Fig. 2.7(a)) is obtained with 25 discrete values per parameter and 390k samples whereas both Metropolis (Fig. 2.7(b)) and Gibbs (Fig. 2.7(c)) samplers use approximately 70k samples and the genetic algorithm (Fig. 2.7(d)) uses less than 10k samples. The results of the Metropolis algorithm and GA are also summarized in Table 2.2. The MATLAB GA toolbox [22] is used for GA results. It uses 3 isolated populations of size 40 each with a

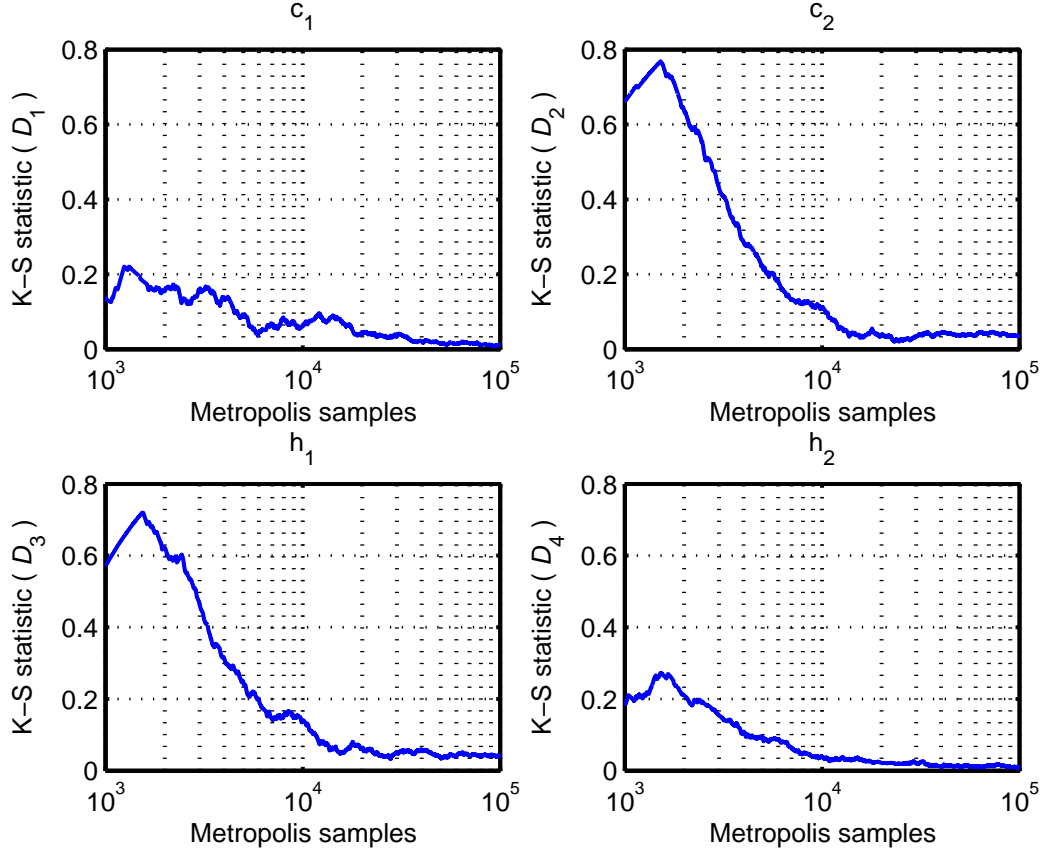


Figure 2.6: Final sampling phase - Kolmogorov-Smirnov statistic D for each parameter. Used for the convergence of the posterior probability density.

migration rate of 0.025 per 10 generations, a mutation rate of 0.10 and a cross-over fraction of 0.8.

All four algorithms have almost identical ML estimates for the parameters. However, it should be noted that MCMC samplers converged after collecting nearly 7 times more samples than GA. On the other hand, the distributions obtained from the MCMC samplers are closer to the true distributions given by exhaustive search.

Marginal and 2-D posterior distributions obtained by the Metropolis sampler are given in Fig. 2.8. The diagonal pdf's are the 1-D marginal pdf's and the off-diagonal plots are the 2-D marginal pdf's, where the 50, 75, and 95% highest posterior density regions (HPD) are plotted, with the ML solution points (white

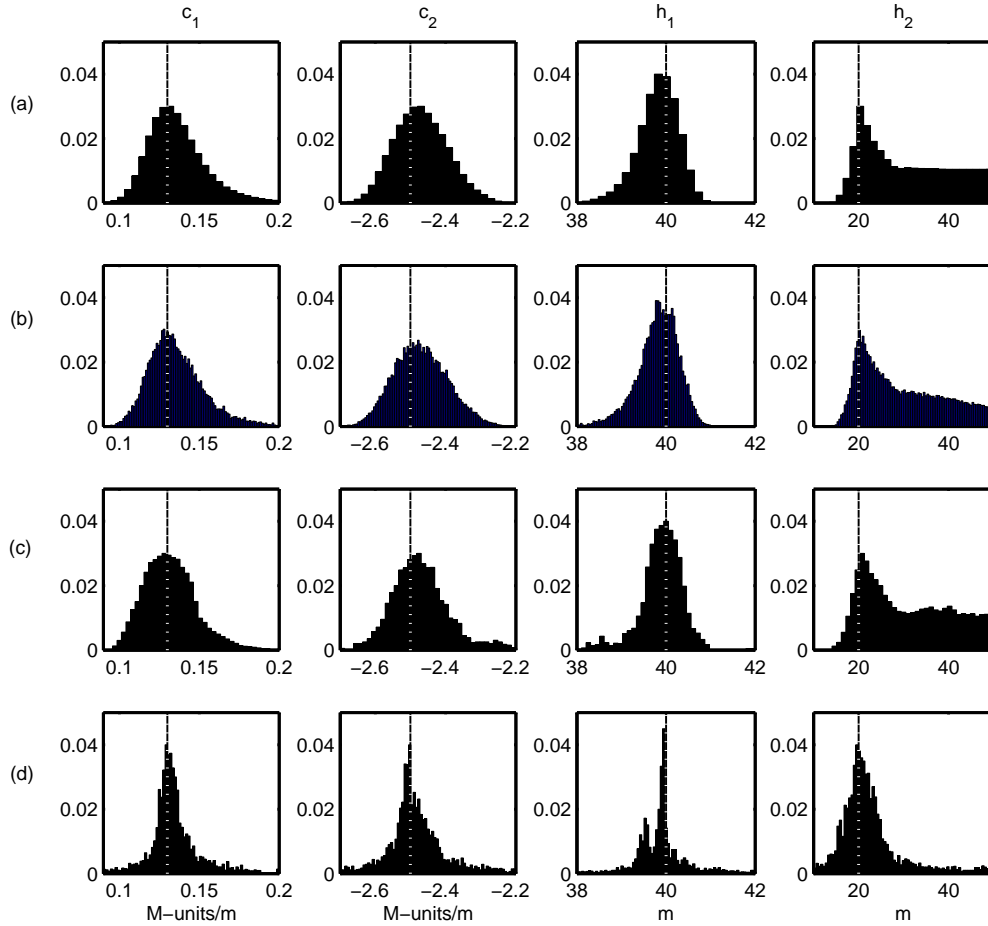


Figure 2.7: Marginal posterior probability distributions for the synthetic test case. Vertical lines show the true values of the parameters. (a) exhaustive search, (b) Metropolis algorithm, (c) Gibbs algorithm, and (d) genetic algorithm.

crosses). In Bayesian statistics, credibility intervals and HPD regions are used to analyze the posterior distributions. They are very similar to the confidence interval and their definitions can be found in [23].

2.4.2 Wallops Island Experiment

The Metropolis sampler is used to analyze the data collected from the Wallops Island 1998 experiment conducted by Naval Surface Warfare Center, Dahlgren Division (Fig. 2.9). The radar clutter data gathered by Space Range

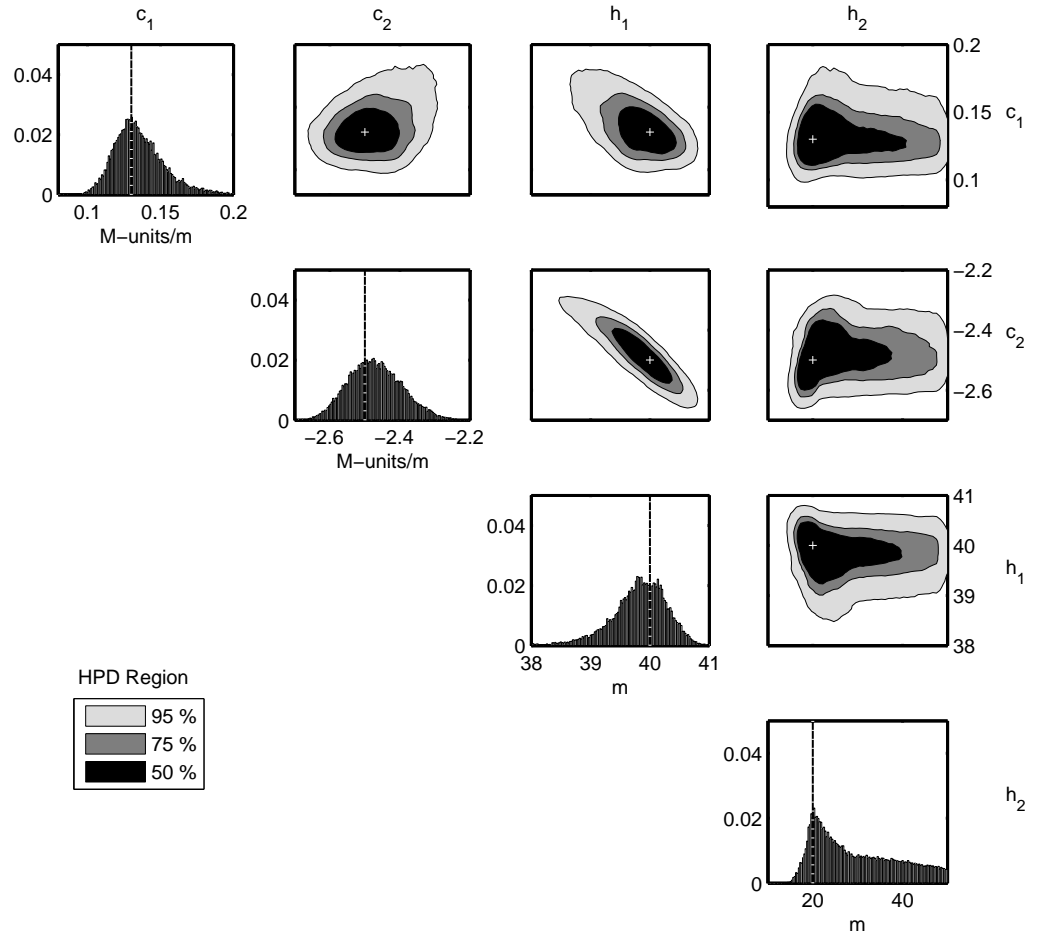


Figure 2.8: Both 1-D marginal (diagonal) and 2-D marginal (upper diagonal) PPD's for the synthetic test case obtained by the Metropolis algorithm. Vertical lines (in 1-D plots) and crosses (in 2-D plots) show the true values of the parameters.

Radar (SPANDAR) is inverted using the Metropolis algorithm and the results are compared with helicopter measurements. Data used in the inversion was taken during a surface-based ducting event on April 2, 1998 [3, 24] at a frequency of 2.84 GHz, power of 91.4 dBm, 3dB beamwidth of 0.4° , antenna gain of 52.8 dB, an MSL height of 30.78 m, VV polarization and with 600 m range bins. Only data between 10-60 km are used in the inversion. The results are summarized in Table 2.3.

The same 4-parameter model used in the synthetic test case is selected.

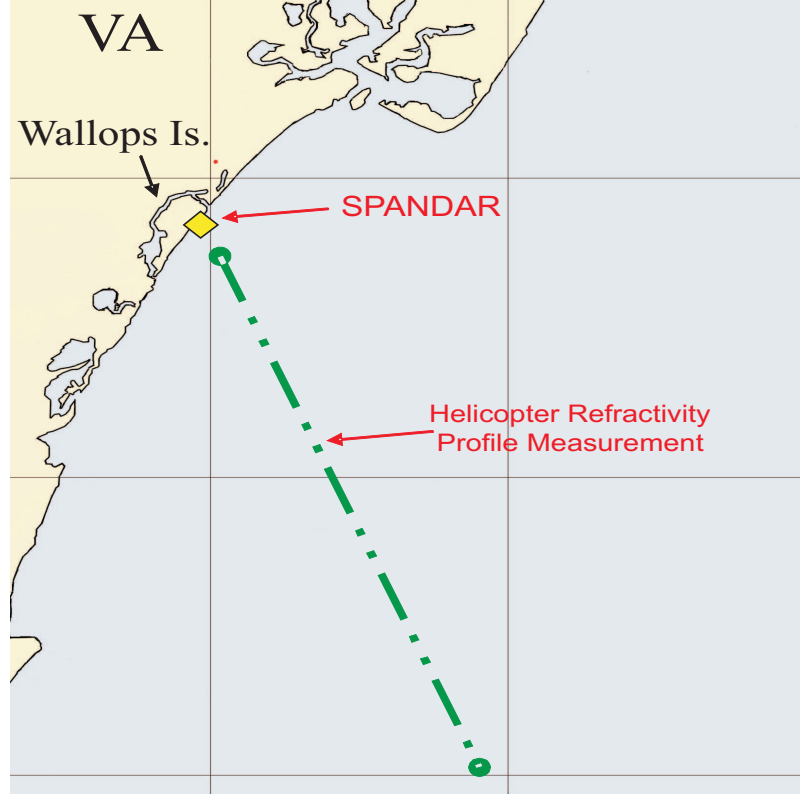


Figure 2.9: Wallops '98 Experiment: SPANDAR radar and the helicopter measurements (37.83° N, 75.48° W)

The marginal distributions obtained by Metropolis and GA in Fig. 2.10 use 80k and 10k samples respectively. Fig. 2.11 shows the 1-D and 2-D marginal PPD plots obtained by the Metropolis algorithm.

The helicopter measurements at different ranges can be seen in Fig. 2.12(a). Profiles measured at 10, 20, 30, 40, and 50 km are all plotted in Fig. 2.12(b) together with HPD regions obtained from the post-processing of the 80k Metropolis samples. These HPD regions show the regions where the values of the tri-linear M-profile at various altitudes are expected to be. Therefore, it roughly can be compared to the mean of the helicopter M-profiles measured at different ranges. This mean helicopter profile is plotted together with the ML solution obtained from the Metropolis sampler in Fig. 2.12(c).

The improvement obtained by the inversion is analyzed in Fig. 2.13. The

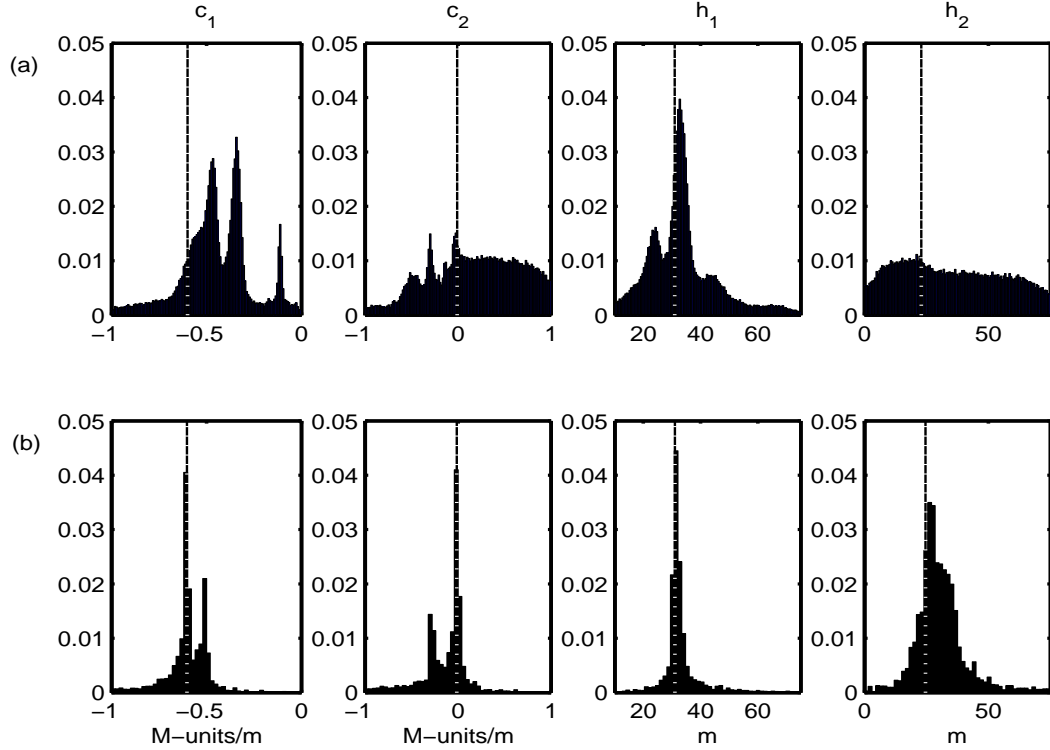


Figure 2.10: Marginal posterior probability distributions obtained using SPAN-DAR data. (a) Metropolis algorithm and (b) genetic algorithm. Vertical lines show the estimated optimum values of the parameters.

coverage diagrams (dB) in Fig. 2.13 (a)-(c) are obtained using a standard atmospheric assumption, helicopter refractivity profile measurements, and the Metropolis inversion results. Fig. 2.13 (d)-(e) are difference plots and are calculated by subtracting the dB coverage diagrams obtained by two different methods. Fig. 2.13 (d) is the difference between the standard atmosphere and the helicopter results, whereas Fig. 2.13 (e) is the difference between the Metropolis inversion and the helicopter results. The improvement inside the duct ($h < 60$ m) easily can be noticed. However, the results outside the duct are not as good. This is an expected result since the inversion is done using the radar measured sea surface reflected clutter caused by the electromagnetic duct. No signal outside the duct is used and hence the inversion algorithm has poor accuracy outside the duct.

In Fig. 2.14, the clutter power vs. range plots are given. The relative

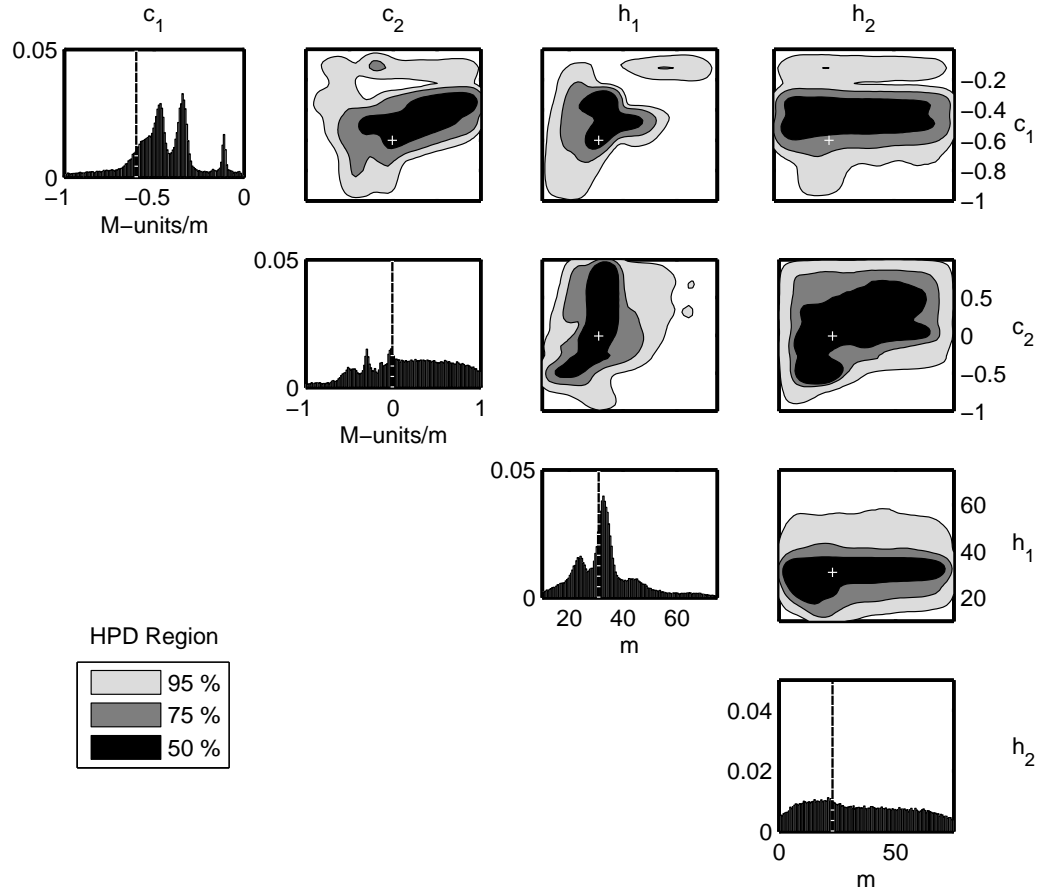


Figure 2.11: Both 1-D marginal (diagonal) and 2-D marginal (upper diagonal) PPD's obtained from the SPANDAR data obtained by the Metropolis algorithm. Vertical lines (in 1-D plots) and crosses (in 2-D plots) show the optimum values of the parameters.

clutter return measured by SPANDAR is plotted together with the clutter found using the Metropolis ML estimate, $\hat{\mathbf{m}}$, and the clutter obtained using the range-varying helicopter profile. Surface layer evaporation ducting was appended to the bottom of the helicopter refractivity profiles, with the evaporation duct heights being less than 5 meters. Then, this profile (Fig. 2.12 (a)) is simulated using the parabolic equation model to estimate the helicopter clutter. Misfits can be explained by the range independent assumption of the simple tri-linear M-profile, which cannot exactly duplicate the real radar clutter. Details of errors associated

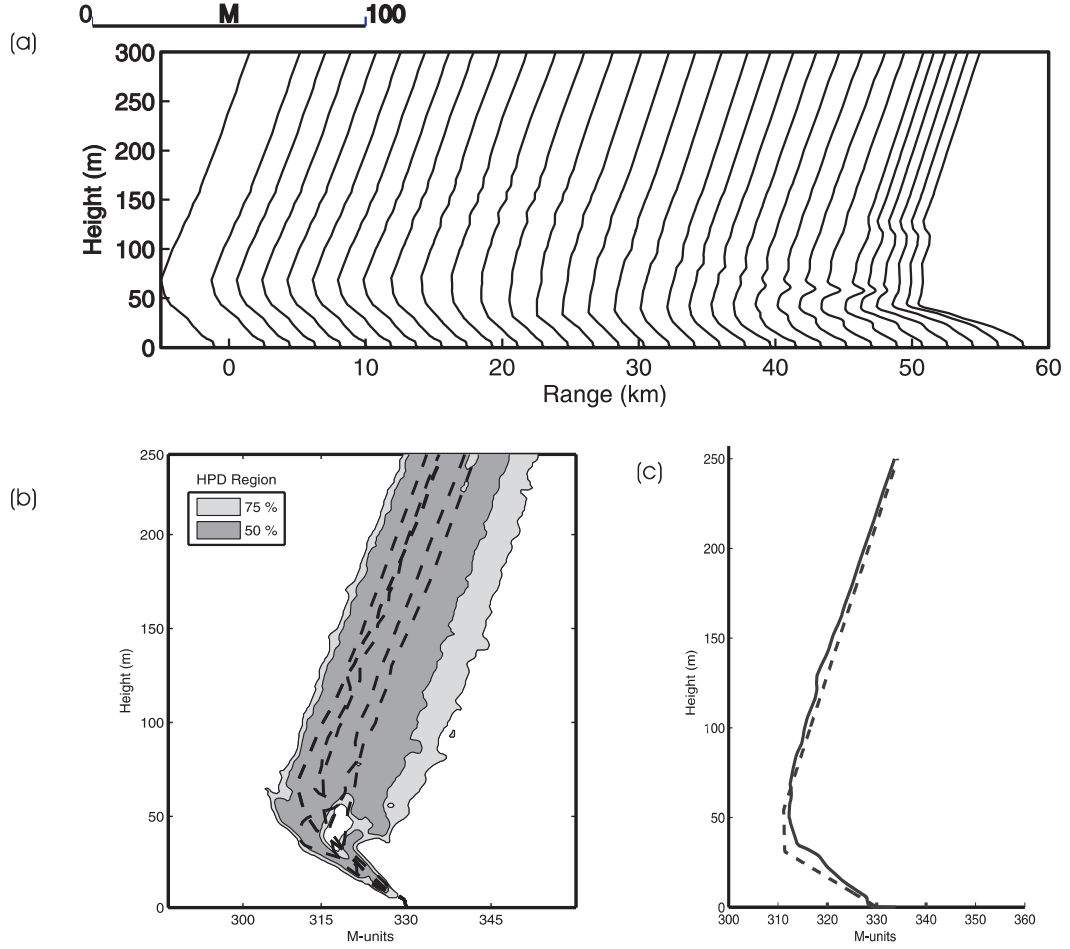


Figure 2.12: M-profiles 0-60km: (a) helicopter measurements at different ranges, (b) helicopter profiles (dashed) at 10, 20, 30, 40, 50 km together with 50% and 75% HPD regions for the range independent model, and (c) range-independent maximum likelihood solution (dashed line) and mean of the profiles measured at different ranges (solid line).

with the range independent assumption can be found in [25].

The PPD of the environmental parameters can be used to get PPD's of parameters-of-interest. This easily can be done by post-processing the 80k Metropolis samples of the refractivity model parameters. Posterior densities for propagation factor (F) at a range of 60 km with height values above MSL of 28 m and 180 m are given in Fig. 2.15 (a) and (b), respectively. These two height values specifically are selected to compare the quality of estimates inside and outside of

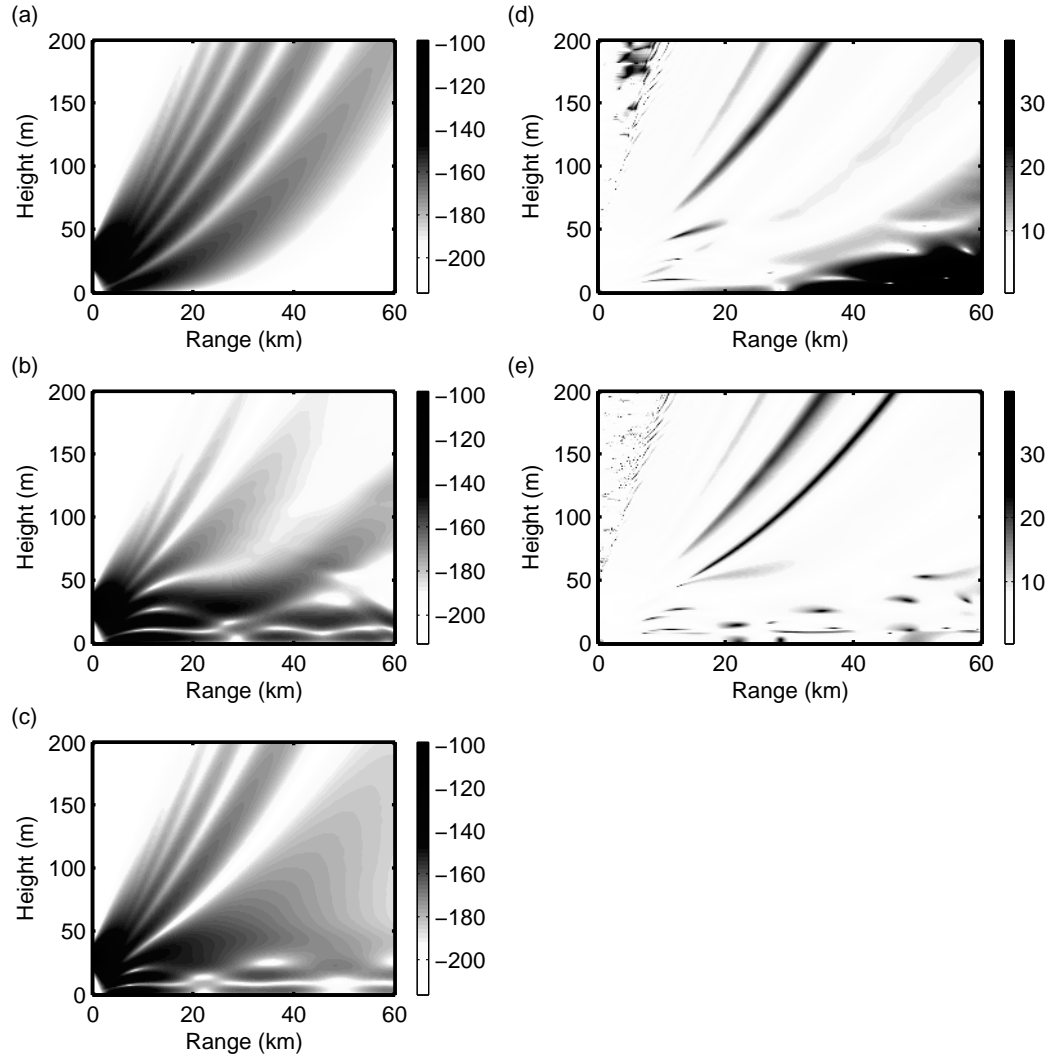


Figure 2.13: Coverage diagrams (dB). One-way propagation loss for: (a) standard atmosphere (0.118 M-units/m), (b) helicopter-measured refractivity profile, and (c) Metropolis inversion result. The difference (dB) between (d) helicopter and standard atmosphere results and (e) helicopter and Metropolis inversion results.

the duct. As expected, F in case (a), which is inside the duct, has a much smaller variance, whereas the uncertainty in case (b) is much larger.

Finally, Fig. 2.15 (c) shows the effects of uncertainty in the environmental parameters on establishing a successful communication link. Assume that the transmitter-receiver pair requires a propagation loss less than 135 dB to attain the

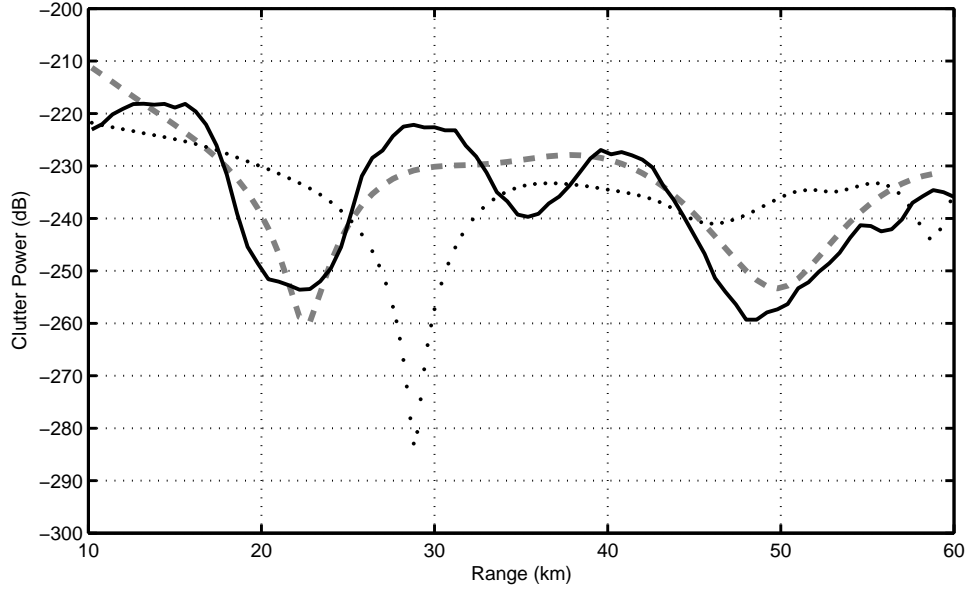


Figure 2.14: Clutter power vs. range plots. Clutter measured by SPAN-DAR (solid), the predicted clutter obtained using the Metropolis ML solution $\hat{\mathbf{m}}$ (dashed), and the predicted clutter obtained using the helicopter-measured refractivity profile (dotted).

necessary SNR to operate in this environment. The diagram shows the probability of establishing a successful link in an environment known to an accuracy of $p(\mathbf{m}|\mathbf{d})$ as a coverage area HPD plot. The results are given as 70, 80, and 90% HPD regions. As expected, the link can be maintained over an extended range inside the duct.

2.5 Conclusion

A method for estimation of the radio refractivity from radar clutter using Markov Chain Monte Carlo (MCMC) samplers with a likelihood-based Bayesian inversion formulation has been introduced. This approach enables us to obtain full n -dimensional posterior probability distributions for the unknown parameters as well as the maximum likelihood solution itself.

Comparisons with exhaustive search and genetic algorithm results show that MCMC samplers require more samples than a classical global optimizer but

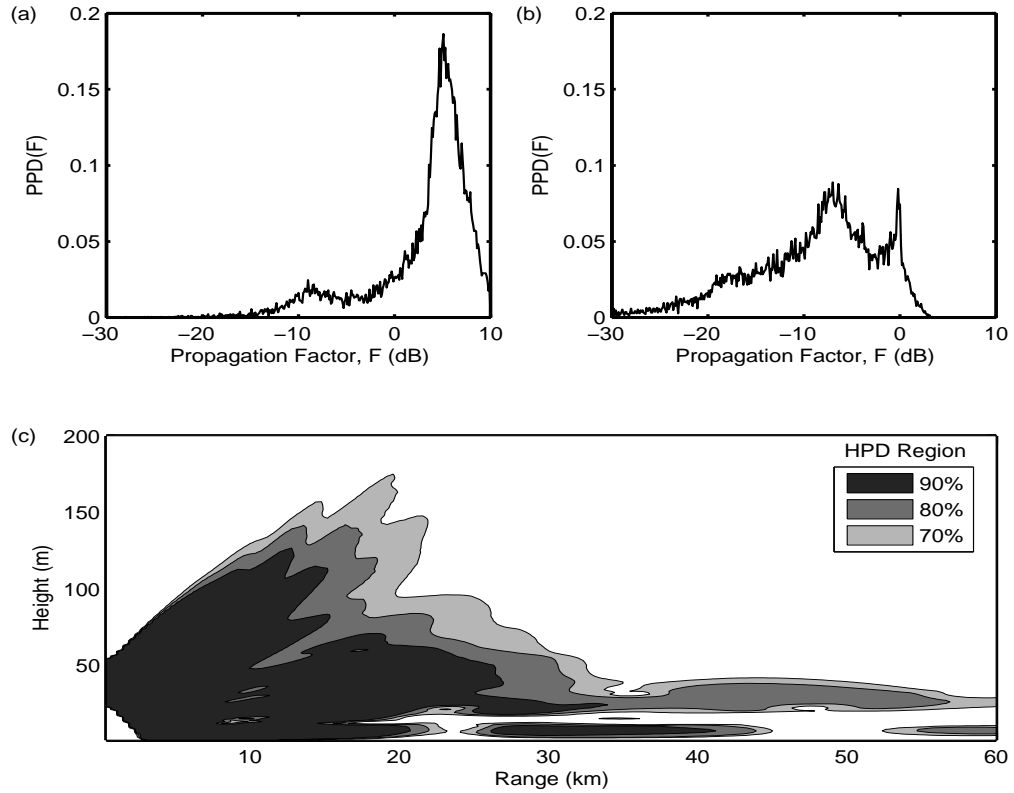


Figure 2.15: PPD for propagation factor F at range 60 km with altitudes of (a) 28 m and (b) 180 m above MSL. (c) PPD of the coverage area for the given communication link.

are better in estimating probability distributions. The need for a relatively large number of forward model runs limits its usage as a near-real time M-profile estimator. However, it can be used together with a fast global optimizer, which will do the near-real time inversion. The MCMC sampler will then provide the credibility intervals and the uncertainties, which may not be needed frequently.

One immediate benefit of the method is the ability to assess the quality of the inversion and obtain highest posterior density (HPD) plots for other parameters that could be of interest to an end-user, such as the one-way propagation loss, propagation factor for different heights and ranges, or variability in the coverage diagrams. They easily can be obtained by post-processing the Metropolis samples

of the refractivity parameters.

2.6 Acknowledgment

The authors would like to thank Ted Rogers, SPAWAR, San Diego, CA, for providing the SPANDAR'98 clutter maps and Daniel Dockery, John Hopkins University, Applied Physics Laboratory, Baltimore, MD, for providing the helicopter refractivity measurements.

The text of this chapter is in full a reprint of the material as it appears in Caglar Yardim, Peter Gerstoft, and William S. Hodgkiss, "Estimation of radio refractivity from radar clutter using Bayesian Monte Carlo analysis," *IEEE Trans. on Antennas and Propagation*, vol. 54, pp. 1318-1327, doi:10.1109/TAP.2006.872673, 2006. The dissertation author was the primary researcher and author, and the co-authors listed in this publication directed and supervised the research which forms the basis for this chapter.

Table 2.1: Notation

| | |
|----------------------------|---|
| \mathbf{d} | Measured radar clutter data vector |
| \mathbf{m} | Refractivity (M-profile) model parameter vector |
| $f(\cdot)$ | Forward model (split-step FFT parabolic equation) |
| $f(\mathbf{m})$ | Replica radar clutter vector that would be observed in an environment characterized by \mathbf{m} |
| $\phi(\mathbf{m})$ | Error function |
| n | Number of model parameters |
| N_R | Number of data points collected at different ranges |
| N | Number of Metropolis/Gibbs samples |
| N_{eff} | Number of effective data points |
| \mathbf{C}_d | Data covariance matrix |
| ν | Error variance |
| $\hat{\nu}$ | Error variance estimate |
| $\hat{\mathbf{m}}$ | Model vector GA estimate |
| D | Kolmogorov-Smirnov (K-S) statistic |
| $p(\mathbf{m} \mathbf{d})$ | Posterior probability density, PPD |
| $\mathcal{L}(\mathbf{m})$ | Likelihood function |
| $p(\mathbf{m})$ | Prior function |
| $p(\mathbf{d})$ | Evidence function |
| $P(m_i \mathbf{d})$ | Cumulative marginal distribution function |
| \mathbf{C}_m | Model covariance matrix |
| $\mathbf{\Lambda}$ | Diagonal matrix containing eigenvalues, λ_i |
| \mathbf{R} | Rotation matrix |
| $\tilde{\mathbf{m}}$ | Rotated model parameter vector |
| T | Simulated annealing temperature |
| r | Range |
| L | One-way propagation loss |
| F | Propagation factor |

Table 2.2: Synthetic data case: GA estimates and Metropolis algorithm results

| Parameter | Units | Search Limits | | True Value | GA Estimate | Metropolis ML Estimate | Mean | STD | 90% Credib. Interv. | |
|-----------|-----------|---------------|------|------------|-------------|------------------------|--------|-------|---------------------|--------|
| | | L. | U. | | | | | | L. | U. |
| c_1 | M-units/m | 0 | 0.25 | 0.13 | 0.132 | 0.128 | 0.1363 | 0.019 | 0.111 | 0.171 |
| c_2 | M-units/m | -3.5 | -1 | -2.5 | -2.504 | -2.503 | -2.47 | 0.077 | -2.59 | -2.34 |
| h_1 | m | 25 | 50 | 40 | 39.93 | 40.05 | 39.80 | 0.147 | 39.938 | 40.488 |
| h_2 | m | 0 | 50 | 20 | 19.86 | 19.96 | 29.65 | 9.184 | 18.375 | 46.750 |

Table 2.3: Wallops island experiment (clutter map 17): GA estimates and Metropolis algorithm results

| Parameter | Units | Search Limits | | GA Estimate | Metropolis ML Estimate | Mean | STD | 90% Credibility Intervals | |
|-----------|-----------|---------------|-------|-------------|------------------------|--------|-------|---------------------------|-------|
| | | Lower | Upper | | | | | Lower | Upper |
| c_1 | M-units/m | -1 | 0 | -0.603 | -0.604 | -0.444 | 0.186 | -0.79 | -0.11 |
| c_2 | M-units/m | -1 | 1 | -0.014 | -0.010 | -0.180 | 0.475 | -0.61 | 0.89 |
| h_1 | m | 10 | 75 | 31.00 | 30.98 | 33.76 | 11.95 | 16.79 | 59.63 |
| h_2 | m | 0 | 75 | 24.63 | 22.93 | 34.41 | 20.50 | 4.69 | 68.66 |

Bibliography

- [1] S. Vasudevan and J. Krolik. Refractivity estimation from radar clutter by sequential importance sampling with a Markov model for microwave propagation. *Proc. ICASSP*, pages 2905–2908, 2001.
- [2] R. Anderson, S. Vasudevan, J. Krolik, and L. T. Rogers. Maximum *a posteriori* refractivity estimation from radar clutter using a Markov model for microwave propagation. In *Proc. IEEE International Geoscience and Remote Sensing Symposium*, volume 2, pages 906–909, Sydney, Australia, 2001.
- [3] Peter Gerstoft, L. T. Rogers, J. Krolik, and W. S. Hodgkiss. Inversion for refractivity parameters from radar sea clutter. *Radio Science*, 38 (3):1–22, 2003. doi:10.1029/2002RS002640.
- [4] Peter Gerstoft, W. S. Hodgkiss, L. T. Rogers, and M. Jablecki. Probability distribution of low altitude propagation loss from radar sea-clutter data. *Radio Science*, 39:1–9, 2004. doi:10.1029/2004RS003077.
- [5] S. E. Dosso. Quantifying uncertainty in geoacoustic inversion I. a fast Gibbs sampler approach. *J. Acoust. Soc. Am.*, 111 (1):129–142, 2002.
- [6] L. Ted Rogers, Michael Jablecki, and Peter Gerstoft. Posterior distributions of a statistic of propagation loss inferred from radar sea clutter. *Radio Science*, 40 (6):1–14, 2005. doi:10.1029/2004RS003112.
- [7] Peter Gerstoft and C. F. Mecklenbräuker. Ocean acoustic inversion with estimation of *a posteriori* probability distributions. *J. Acoust. Soc. Am.*, 104 (2):808–819, 1998.
- [8] Amalia E. Barrios. A terrain parabolic equation model for propagation in the troposphere. *IEEE Trans. Antennas Propagat.*, 42 (1):90–98, 1994.
- [9] M. Levy. *Parabolic Equation Methods for Electromagnetic Wave Propagation*. The Institution of Electrical Engineers, London, United Kingdom, 2000.
- [10] Steven M. Kay. *Fundamentals of Statistical Signal Processing - Volume I: Estimation Theory*. Prentice-Hall, New Jersey, 1993.

- [11] M. K. Sen and P. L. Stoffa. Bayesian inference, Gibbs' sampler and uncertainty estimation in geophysical inversion. *Geophys. Prosp.*, 44:313–350, 1996.
- [12] N. Metropolis, A. W. Rosenbluth, M. N. Rosenbluth, A. H. Teller, and E. Teller. Equation of state calculations by fast computing machines. *J. of Chemical Physics*, 21:1087–1092, 1953.
- [13] S. Geman and D. Geman. Stochastic relaxation, Gibbs distributions, and the Bayesian restoration of images. *IEEE Trans. Pattern Anal. Machine Intell.*, 6:721–741, 1984.
- [14] S. E. Dosso and P. L. Nielsen. Quantifying uncertainty in geoacoustic inversion II. application to broadband, shallow-water data. *J. Acoust. Soc. Am.*, 111 (1):143–159, 2002.
- [15] David J. Battle, P. Gerstoft, W. S. Hodgkiss, W. A. Kuperman, and P. L. Nielsen. Bayesian model selection applied to self-noise geoacoustic inversion. *J. Acoust. Soc. Am.*, 116 (4):2043–2056, oct 2004.
- [16] J. J. K. Ó Ruanaidh and W. J. Fitzgerald. *Numerical Bayesian Methods Applied to Signal Processing*. Statistics and Computing Series. Springer–Verlag, New York, 1996.
- [17] K. Mosegaard and M. Sambridge. Monte Carlo analysis of inverse problems. *Inverse Problems*, 18 (3):29–54, 2002.
- [18] David J. C. MacKay. *Information Theory, Inference and Learning Algorithms*. Cambridge University Press, Cambridge, United Kingdom, 2003.
- [19] M. D. Collins and L. Fishman. Efficient navigation of parameter landscapes. *J. Acoust. Soc. Am.*, 98:1637–1644, 1995.
- [20] W. H. Press, S. A. Teukolsky, W. T. Vetterling, and B.P. Flannery. *Numerical Recipes in C*. Cambridge University Press, Cambridge, United Kingdom, second edition, 1995.
- [21] Kenneth D. Anderson. Radar detection of low-altitude targets in a maritime environment. *IEEE Trans. Antennas Propagat.*, 43(6):609–613, june 1995.
- [22] David E. Goldberg. *Genetic Algorithms in Search, Optimization & Machine Learning*. Addison-Wesley, 1989.
- [23] George E. P. Box and George C. Tiao. *Bayesian Inference in Statistical Analysis*. Addison–Wesley, New York, 1992.
- [24] L. Ted Rogers, C. P. Hattan, and J. K. Stapleton. Estimating evaporation duct heights from radar sea echo. *Radio Science*, 35 (4):955–966, 2000. doi:10.1029/1999RS002275.

- [25] Julius Goldhirsh and Daniel Dockery. Propagation factor errors due to the assumption of lateral homogeneity. *Radio Science*, 33(2):239–249, 1998. doi:10.1029/97RS03321.

Statistical Maritime Radar Duct Estimation Using a Hybrid Genetic Algorithms – Markov Chain Monte Carlo Method

This paper addresses the problem of estimating the lower atmospheric refractivity (M-profile) under non-standard propagation conditions frequently encountered in low altitude maritime radar applications. This is done by statistically estimating the duct strength (range and height-dependent atmospheric index of refraction) from the sea-surface reflected radar clutter. These environmental statistics can then be used to predict the radar performance.

In previous work, genetic algorithms (GA) and Markov chain Monte Carlo (MCMC) samplers were used to calculate the atmospheric refractivity from returned radar clutter. Although GA is fast and estimates the maximum *a posteriori* (MAP) solution well, it poorly calculates the multi-dimensional integrals required to obtain the means, variances and underlying posterior probability distribution functions (PPD) of the estimated parameters. More accurate distributions and integral calculations can be obtained using MCMC samplers, such as the Metropolis-

Hastings (M-H) and Gibbs sampling (GS) algorithms. Their drawback is that they require a large number of samples relative to the global optimization techniques such as GA and become impractical with increasing number of unknowns.

A hybrid GA-MCMC method based on the nearest neighborhood algorithm (NA) is implemented in this paper. It is an improved GA method which improves integral calculation accuracy through hybridization with a MCMC sampler. Since the number of forward models is determined by GA, it requires fewer forward model samples than a MCMC, enabling inversion of atmospheric models with a larger number of unknowns.

3.1 Introduction

In many maritime regions of the world, such as the Mediterranean, Persian Gulf, East China Sea, and California Coast, atmospheric ducts are common occurrences. They result in various anomalies such as significant variations in the maximum operational radar range and increased sea clutter. Hence, radar systems operating in these environments would benefit from knowing the effects of the environment on their system performance. This requires knowledge of the atmospheric refractivity, which is usually represented by the modified refractivity (M-profile) in the radar community [1].

Evaporation and surface-based ducts are associated with increased sea clutter due to the heavy interaction between the sea surface and the electromagnetic signal trapped within the duct. However, this unwanted clutter is a rich source of information about the environment and can be used to determine the local atmospheric conditions. This can be a valuable addition to other more conventional techniques such as radiosondes, rocketsondes, microwave refractometers and meteorological models such as the Coupled Ocean/Atmospheric Mesoscale Prediction System (COAMPS) that give M-profile forecasts [1–4]. In a Bayesian framework, the results of one or several of these techniques and regional duct statis-

tics [5] can be coupled with the clutter inversion to improve the overall estimation quality. An attractive feature of inferring refractivity from sea surface clutter is that it does not use additional hardware or extra meteorological/electromagnetic measurements. It extracts the information from the radar clutter obtained during normal radar operation, which usually is readily available both as a function of range, direction and time. For a fast inversion algorithm, a near-real-time M-profile structure is obtained. The need for a fast algorithm that updates the environmental estimates at intervals of 30 min. or less is evident from [6], where the RMS error in propagation factor exceeds 6 dB after 30 min., due to temporal decorrelation.

Various techniques that estimate the M-profile using radar clutter return are proposed by [7], [8, 9], [10], [11], [12], and [13]. Most of these refractivity from clutter (RFC) techniques use an electromagnetic fast Fourier transform (FFT) split-step parabolic equation (SSPE) approximation to the wave equation [14, 15], whereas some also make use of ray-tracing techniques. While the paper by [7] exclusively deals with evaporation duct estimation, other techniques are applicable to both evaporation, surface-based and mixed type of ducts that contain both an evaporation section and an surface-based type inversion layer. [13] exploits the inherent Markovian structure of the FFT parabolic equation approximation and uses a particle filtering approach, whereas [10] uses rank correlation with ray tracing to estimate the M-profile.

In contrast, [8, 9] and [12] use global parameterization within a Bayesian framework. Since the unknown model parameters are defined as random variables in a Bayesian framework, the inversion results will be in terms of the means, variances and marginal, as well as the n -dimensional joint posterior probability distributions, where n represents the number of unknown duct parameters. This gives the user not only the ability to obtain the maximum *a posteriori* (MAP) solution, but also the prospect of performing statistical analysis on the inversion results and the means to convert these environmental statistics into radar performance statistics. These statistical calculations can be performed by taking multi-

dimensional integrals of the joint PPD. [8] uses genetic algorithms to estimate the MAP solution. However, no statistical analysis is performed since classical GA is not suitable for the necessary integral calculations. While [9] uses importance sampling, [12] uses Markov chain Monte Carlo (MCMC) samplers to perform the MC integration [16, 17]. Although they provide the means to quantify the impact of uncertainty in the estimated duct parameters, they require large numbers of forward model runs and hence they lack the speed to be near-real-time methods and are not suitable for models with large numbers of unknowns.

In this paper, a hybrid GA-MCMC technique is implemented. The method reduces the number of forward model runs required to perform the RFC inversion, while still being able to perform MC integration. It is first tested on the synthetic data used by [12] with a four-parameter, range-independent, tri-linear M-profile model (Fig. 3.1). Then data collected during the 1998 Wallops island experiment (Wallops'98) [8] is analyzed using a sixteen-parameter range-dependent atmospheric model to show the capabilities and limitations of the method. An evaporative duct structure is not appended in this work but it can be done by introducing a Jeske-Paulus (JP) [18, 19] or Liu-Katsaros-Businger (LKB) [20] profile using one or more extra evaporation duct parameters, depending on the conditions.

3.2 Model Formulation

For electromagnetic propagation purposes, the environment can be uniquely represented by the range and height-dependent index of refraction, which itself is a complex function of temperature, humidity, and pressure [21]. Therefore, the term environmental parameters will be used exclusively for the M-profile parameters henceforth. To formulate the problem, a classical Bayesian framework is adopted, where the M-profile model and the radar measured sea-surface clutter data are denoted by the vectors \mathbf{m} and \mathbf{d} , respectively. An electromagnetic FFT-SSPE is used to propagate the field in an environment given by \mathbf{m} and obtain synthetic clutter

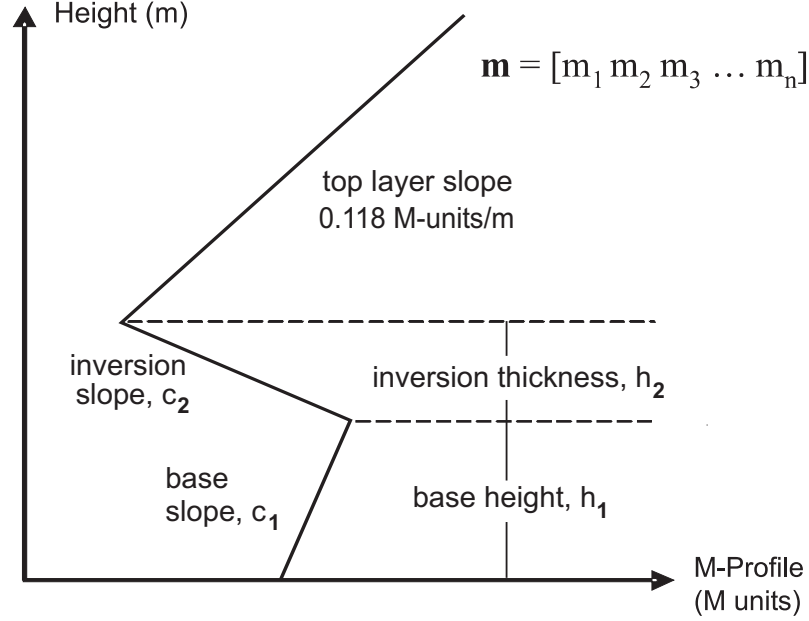


Figure 3.1: Four-parameter range-independent tri-linear M-profile.

returns $f(\mathbf{m})$. Since the unknown environmental parameters \mathbf{m} are assumed to be random variables, the solution to the inversion is given by their joint posterior probability distribution function (PPD or $p(\mathbf{m}|\mathbf{d})$). Bayes' formula can be used to write the PPD as

$$p(\mathbf{m}|\mathbf{d}) = \frac{\mathcal{L}(\mathbf{m})p(\mathbf{m})}{\int_{\mathbf{m}'} \mathcal{L}(\mathbf{m}')p(\mathbf{m}')d\mathbf{m}'}, \quad (3.1)$$

where $p(\mathbf{m})$ is the prior probability distribution function (pdf) of the parameters. Any information obtained from other methods and regional duct statistics can be incorporated in this step as a prior belief. Since this paper investigates the ability to infer M-profiles using RFC, a uniform prior is used. However, it is possible to include statistical meteorological priors from studies such as [5], for some of the parameters (e.g. the duct height).

Assuming a zero-mean Gaussian error between the measured and modeled clutter, the likelihood function is given by

$$\begin{aligned} \mathcal{L}(\mathbf{m}) &= (2\pi)^{-N_R/2} |\mathbf{C}_d|^{-1/2} \\ &\times \exp \left[-\frac{(\mathbf{d} - f(\mathbf{m}))^T \mathbf{C}_d^{-1} (\mathbf{d} - f(\mathbf{m}))}{2} \right], \end{aligned} \quad (3.2)$$

where \mathbf{C}_d is the data error covariance matrix, $(\cdot)^T$ is the transpose and N_R is the number of range points used (length of the data vector, \mathbf{d}). Further simplification can be achieved by assuming that the errors are spatially uncorrelated with identical distribution for each data point forming the vector \mathbf{d} . For this case, $\mathbf{C}_d = \nu \mathbf{I}$, where ν is the variance and \mathbf{I} the identity matrix. Then the equation can be simplified to

$$\mathcal{L}(\mathbf{m}) = (2\pi\nu)^{-N_R/2} \exp\left[-\frac{\phi(\mathbf{m})}{2\nu}\right], \text{ where} \quad (3.3)$$

$$\phi(\mathbf{m}) = (\mathbf{d} - f(\mathbf{m}))^T (\mathbf{d} - f(\mathbf{m})). \quad (3.4)$$

The maximum likelihood (ML) estimate for the error variance can be found by solving $\partial\mathcal{L}/\partial\nu = 0$, which results in

$$\hat{\nu}_{ML} = \frac{\phi(\mathbf{m})}{N_R}. \quad (3.5)$$

After inserting it back into the likelihood function, $\mathcal{L}(\mathbf{m})$ finally can be reduced to

$$\mathcal{L}(\mathbf{m}) = \left[\frac{N_R}{2\pi e \phi(\mathbf{m})} \right]^{N_R/2}, \text{ and} \quad (3.6)$$

$$p(\mathbf{m}|\mathbf{d}) \propto p(\mathbf{m}) \left[\frac{N_R}{2\pi e \phi(\mathbf{m})} \right]^{N_R/2}. \quad (3.7)$$

Having defined the posterior density, any statistical information about the unknown environmental and radar parameters can now be calculated by taking these multi-dimensional integrals:

$$\mu_i = \int \dots \int m'_i p(\mathbf{m}'|\mathbf{d}) d\mathbf{m}' \quad (3.8)$$

$$\sigma_i^2 = \int \dots \int (m'_i - \mu_i)^2 p(\mathbf{m}'|\mathbf{d}) d\mathbf{m}' \quad (3.9)$$

$$p(m_i|\mathbf{d}) = \int \dots \int \delta(m'_i - m_i) p(\mathbf{m}'|\mathbf{d}) d\mathbf{m}' \quad (3.10)$$

where μ_i , σ_i^2 , $p(m_i|\mathbf{d})$ are posterior means (Bayesian minimum mean square error (MMSE) estimate), variances, and marginal PPD's of M-profile parameters.

Probability distributions of parameters of interest to a radar operator are calculated in a similar fashion. Assume that u is such a parameter-of-interest

(e.g. propagation factor), which naturally is some function $u = g(\mathbf{m})$ of the radar environment \mathbf{m} . A statistical analysis of u can be carried out by transformation of random variables. The classical transformation formula

$$p(u|\mathbf{d}) = \frac{p(\mathbf{m}|\mathbf{d})}{|J(\mathbf{m})|}, \quad (3.11)$$

where $J(\mathbf{m})$ represents the Jacobian of the transformation, can be written in integral form [22]

$$p(u|\mathbf{d}) = \int \dots \int \delta(u - g(\mathbf{m}')) p(\mathbf{m}'|\mathbf{d}) d\mathbf{m}', \quad (3.12)$$

in the same form as (3.8)–(3.10). This form is preferred since it enables the evaluation of desired quantities with MC integration.

3.3 The Hybrid GA-MCMC Method

To improve the lack of accuracy in GA and lack of speed in MCMC, a hybrid method based on the nearest neighborhood (NA) algorithm [23–26] is adopted here. This method effectively converts the samples gathered during a typical global optimization run (e.g. GA) into a form that can be used in MC integration. Then it uses a fast MCMC to compute these integrals.

3.3.1 Monte Carlo Integration and Genetic Algorithms

Notice that all of the integrals in (3.8)–(3.10) and (3.12) are of the form

$$I = \int g(x) p(x) dx, \quad (3.13)$$

where x is a random variable with a pdf of $p(x)$, and $g(x)$ is some function of x . These multi-dimensional integrals can be estimated numerically using the Monte Carlo integration technique [16]. Assuming a large number of random x values are drawn from a sampling distribution $p_s(x)$, $\{x^1, x^2, x^3, \dots, x^{N_s}\}$, the integral I can be estimated as

$$I \simeq \frac{\sum_{i=1}^{N_s} \frac{p(x^i) g(x^i)}{p_s(x^i)}}{\sum_{i=1}^{N_s} \frac{p(x^i)}{p_s(x^i)}}. \quad (3.14)$$

By introducing a weight function the integral can be approximated as

$$w(x^i) \triangleq \frac{p(x^i)}{p_s(x^i)}, \quad (3.15)$$

$$I \simeq \frac{\sum_{i=1}^{N_s} w(x^i)g(x^i)}{\sum_{i=1}^{N_s} w(x^i)}. \quad (3.16)$$

This is the well known importance sampling formula, where $p_s(x)$ is usually selected to be a uniform or Gaussian density. The main drawback of this approach is the slow convergence and relatively low accuracy resulting from the difference between the parameter pdf $p(x)$ and the sampling pdf $p_s(x)$. The best result is obtained if $p_s(x) = p(x)$, which is used by MCMC techniques such as Metropolis-Hastings [27, 28] and Gibbs samplers [29].

Importance sampling is used for RFC inversion by [9], where the prior $p(\mathbf{m})$ is used as the sampling density. However, the results depend on how close $p(\mathbf{m})$ is to $p(\mathbf{m}|\mathbf{d})$. Both Metropolis and Gibbs samplers are used by [12] with $p_s(\mathbf{m}) = p(\mathbf{m}|\mathbf{d})$. A drawback of these techniques is the necessity to run many forward modeling runs. Many global optimizers such as the classical GA do not have a $p_s(x)$. Every run will result in a different distribution concentrated around the higher density regions. However, due to its speed, it is desirable to use GA in MC integration. Such an approach requires a technique that estimates the integrals (3.8)–(3.10) and (3.12) using an ensemble of GA samples without a $p_s(x)$.

3.3.2 Voronoi Decomposition

A sampling density $p_s(x)$ that is an approximation to $p(\mathbf{m}|\mathbf{d})$, is created using the information gathered from the ensemble of GA samples. Then this approximate PPD $\hat{p}(\mathbf{m}|\mathbf{d})$ is used to calculate the Bayesian integrals by replacing (3.15)–(3.16) with

$$w(\mathbf{m}^i) = \frac{p(\mathbf{m}^i|\mathbf{d})}{\hat{p}(\mathbf{m}^i|\mathbf{d})} \simeq 1 \quad (3.17)$$

$$I \simeq \frac{1}{N_s} \sum_{i=1}^{N_s} g(\mathbf{m}^i). \quad (3.18)$$

$\hat{p}(\mathbf{m}|\mathbf{d})$ is obtained by using Voronoi decomposition (or Dirichlet tessellation) of the n -dimensional model space [30,31]. It creates a convex n -dimensional polytope (a polygon if $n = 2$, a polyhedron if $n = 3$) called a Voronoi cell (or Dirichlet domain) around the nearest neighborhood of each GA point. For a given set of GA samples there exists a unique set of corresponding Voronoi cells that tessellates the model space. This structure is adaptable and if points are changed, removed or added, the cells rearrange themselves, shrink and enlarge to reflect the changes. Therefore, even if the ensemble of GA samples change with every independent simulation, Voronoi lattice will adjust and likely provide accurate Bayesian integral calculations.

For nearest neighborhood calculations a weighted L_2 -norm is used to compute the distances. The weight removes the units of the parameters, specifically between the M-layer slopes (M-units/m) and layer thicknesses (m). If available, the prior model covariance matrix can be used as the norm weight. Since no *a priori* information is used, the weight is only used to scale each parameter so that all parameters lie within [0,1] range, contributing equally to norm calculations. Therefore, with an initial set of GA samples $\{\mathbf{m}^1, \mathbf{m}^2, \mathbf{m}^3, \dots, \mathbf{m}^{N_{GA}}\}$ without a $p_s(\mathbf{m})$,

$$\|\mathbf{m} - \mathbf{m}^i\|_W^2 = (\mathbf{m} - \mathbf{m}^i)^T W (\mathbf{m} - \mathbf{m}^i), \quad (3.19)$$

$$V_i = \left\{ \mathbf{m} : i = \arg\min_{i'} \|\mathbf{m} - \mathbf{m}^{i'}\|_W \right\}, \quad (3.20)$$

$$\hat{p}(\mathbf{m} \in V_i | \mathbf{d}) = p(\mathbf{m}^i | \mathbf{d}), \quad (3.21)$$

where W is the weight and V_i is the i th Voronoi cell centered at the i th GA sample \mathbf{m}^i . $\hat{p}(\mathbf{m}|\mathbf{d})$ is constant inside the cell, effectively discretizing the original PPD into N_{GA} possible levels. Similar to an A/D converter, it will convert the true “analog” PPD into a “digitized” approximation. The only difference is that, this A/D converter is n -dimensional, and hence, discrete levels are n -dimensional polytopes.

With this assumption, $\hat{p}(\mathbf{m}|\mathbf{d})$ is known at any point anywhere in the

entire search space and there is no need for any further forward model runs.

3.3.3 MCMC (Gibbs) Resampling

Now that a sampling density $p_s(\mathbf{m}) = \hat{p}(\mathbf{m}|\mathbf{d})$ is defined, the next step is drawing samples from this PPD to compute (3.18) for any desired function $g(\cdot)$. Unlike classical MCMC, this MCMC sampler will not suffer from the high number of forward model runs required for MCMC because it operates on the approximate PPD, requiring no forward modeling.

The perfect MCMC sampler for this task is the Gibbs sampler (GS) [12, 16, 29] and is also used in the neighborhood algorithm [24]. Therefore, the term GS will be used instead of the MCMC henceforth. GS gets samples by updating one parameter at a time in a circulatory fashion and it uses the local conditional 1-D PPD to update each parameter. After all of the parameters are updated once, the result will form the next Gibbs sample. This is a particularly fast algorithm since the Metropolis acceptance/rejection criterion used in MCMC samplers is always met and every proposed point is accepted. The difficulty is that, it requires the knowledge of conditional 1-D PPD's, which often are not available for many inversion problems. However, here the conditional is available via Voronoi cells.

A simple example in Fig. 3.2 illustrates the approach with only two unknown parameters. Voronoi cells are constructed around each GA sample (stars) to create the approximate PPD where $\hat{p}(\mathbf{m}|\mathbf{d})$ is constant in each polygon. To obtain the next Gibbs sample (diamonds) first the local 1-D conditional probability density is calculated along the line intersecting the original Gibbs sample. The local conditional density $p(m_1|m_2, \mathbf{d})$ for the first Gibbs sample (PPD along AA') is plotted above the Voronoi diagram. Since the conditional PPD only changes at the cell boundaries, computation of the intersection points with AA' is sufficient to extract the local PPD. This lets us use the Voronoi decomposition without actually having to estimate the Voronoi cell structures or calculate their vertices. Afterwards, a sample is drawn from this simple 1-D PPD and the parameter m_1 is

updated accordingly. To complete the cyclic updating of each parameter, parameter m_2 is also updated using the local conditional PPD $p(m_2|m_1, \mathbf{d})$ (PPD along BB'), plotted on the right-hand side of the Voronoi diagram.

The intersection between Voronoi cells and the conditional line is calculated using the procedure given by [23]. Two neighboring Voronoi cells V_i and V_j intersecting the conditional line are given in Fig. 3.3. They are created around their corresponding cell centers (GA samples \mathbf{m}^i and \mathbf{m}^j) and Gibbs sampler is updating along the k th-axis by sampling from $\hat{p}(m_k|\forall m_l, l \neq k, \mathbf{d})$. The boundary can be calculated using the fact that the distances from both cell centers \mathbf{m}^i and \mathbf{m}^j to the boundary point \mathbf{b}^{ij} must be same by the definition of nearest neighborhood. Hence, using $W = I$,

$$\|\mathbf{m}^i - \mathbf{b}^{ij}\|^2 = \|\mathbf{m}^j - \mathbf{b}^{ij}\|^2, \quad (3.22)$$

$$(d_\perp^i)^2 + (m_k^i - b_k^{ij})^2 = (d_\perp^j)^2 + (m_k^j - b_k^{ij})^2, \quad (3.23)$$

$$b_k^{ij} = \frac{1}{2} \left[m_k^i + m_k^j + \frac{(d_\perp^i)^2 - (d_\perp^j)^2}{m_k^i - m_k^j} \right], \quad (3.24)$$

where d_\perp 's represent the distances of the cell centers (GA points) to the current conditional line, subscripts show the current axis components of the n -dimensional vectors, superscripts show the Voronoi cell index (or GA point index), and b_k^{ij} is the k th component of the boundary point \mathbf{b}^{ij} , defined by the intersection of V_i , V_j , and the local conditional line. The method is summarized by the following steps:

1. *GA*: Run a classical GA, minimizing the misfit $\phi(\mathbf{m})$, save all the populations (sampled model vectors) and their likelihood values. MAP solution is obtained as the best fit model vector.
2. *Voronoi Decomposition and Approximate PPD*: Using the GA samples $\{\mathbf{m}^i\}$ and their corresponding $p(\mathbf{m}^i|\mathbf{d})$ construct the Voronoi cell structure and create the approximate PPD, $\hat{p}(\mathbf{m}|\mathbf{d})$.

3. *Gibbs Resampling*: Run a fast GS on the approximate PPD. No forward modeling is needed.
4. *MC Integral Calculations*: Calculate the Bayesian minimum mean square estimate (MMSE), variance and posterior distributions of desired environmental parameters, statistics for the end-user parameters, such as propagation loss L , propagation factor F , coverage diagrams, statistical radar performance prediction, such as the probability of detection and false alarm using (3.8) – (3.10), and (3.12) in the form of (3.18) as a MC integration.

The accuracy of the results depends mostly on the quality of the approximate PPD, which means that, GA should gather enough samples from the entire n -dimensional search space to allow the hybrid algorithm to construct an adequate n -dimensional mesh. Due to the approximation of the PPD, the method can not guarantee convergence unlike MCMC samplers which are guaranteed to converge as more samples are collected.

3.4 Examples

3.4.1 Synthetic Data

The method is first tested on the synthetic data given by [12]. In that paper, the PPD was estimated using exhaustive search, GA only, and MCMC only. Radar system and environmental parameters are given in Table 3.1. A typical four-parameter range-independent tri-linear profile (Fig. 3.1) is used with the unknown environment parameters and the selected upper and lower limits given in Table 3.2. The unknown model parameters are the slope and height of the base layer (c_1 and h_1) and the slope and thickness of the inversion layer (c_2 and h_2). Since the RFC is insensitive to the M-profile parameters above the duct, the top layer slope corresponds to standard atmosphere.

1-D marginal model parameter PPD's are given in Fig. 3.4 for (a) exhaustive search, (b) Metropolis-Hastings sampler (conventional MCMC), (c) pure

Table 3.1: System Parameters

| Simulation Parameter | Value |
|--------------------------------------|-------------------|
| Frequency | 2840 MHz |
| 3dB beamwidth | 0.4° |
| Source height | 30.78 m |
| Polarization | VV |
| Duct type | SBD only |
| Top layer slope | 0.118 M-units/m |
| Range bin width | 600 m |
| Environmental Model: Synthetic data | |
| Number of parameters | 4 |
| M-profile model type | Range independent |
| Inversion range interval | 10–60 km |
| Clutter standard deviation | 10 dB |
| Environmental Model: Wallops’98 data | |
| Number of parameters | 16 |
| M-profile model type | Range dependent |
| Inversion range interval | 10–70 km |
| M-profile defined at | 0, 20, 40, 60 km |

Table 3.2: Synthetic data case: Model Parameters

| Model Parameter | Units | True Value | Lower Bound | Upper Bound |
|--------------------|-----------|------------|----------------|----------------|
| c_1 | M-units/m | 0.13 | 0 | 0.25 |
| c_2 | M-units/m | −2.5 | −3.5 | −1 |
| h_1 | m | 40 | 0 | 50 |
| h_2 | m | 20 | 0 | 50 |

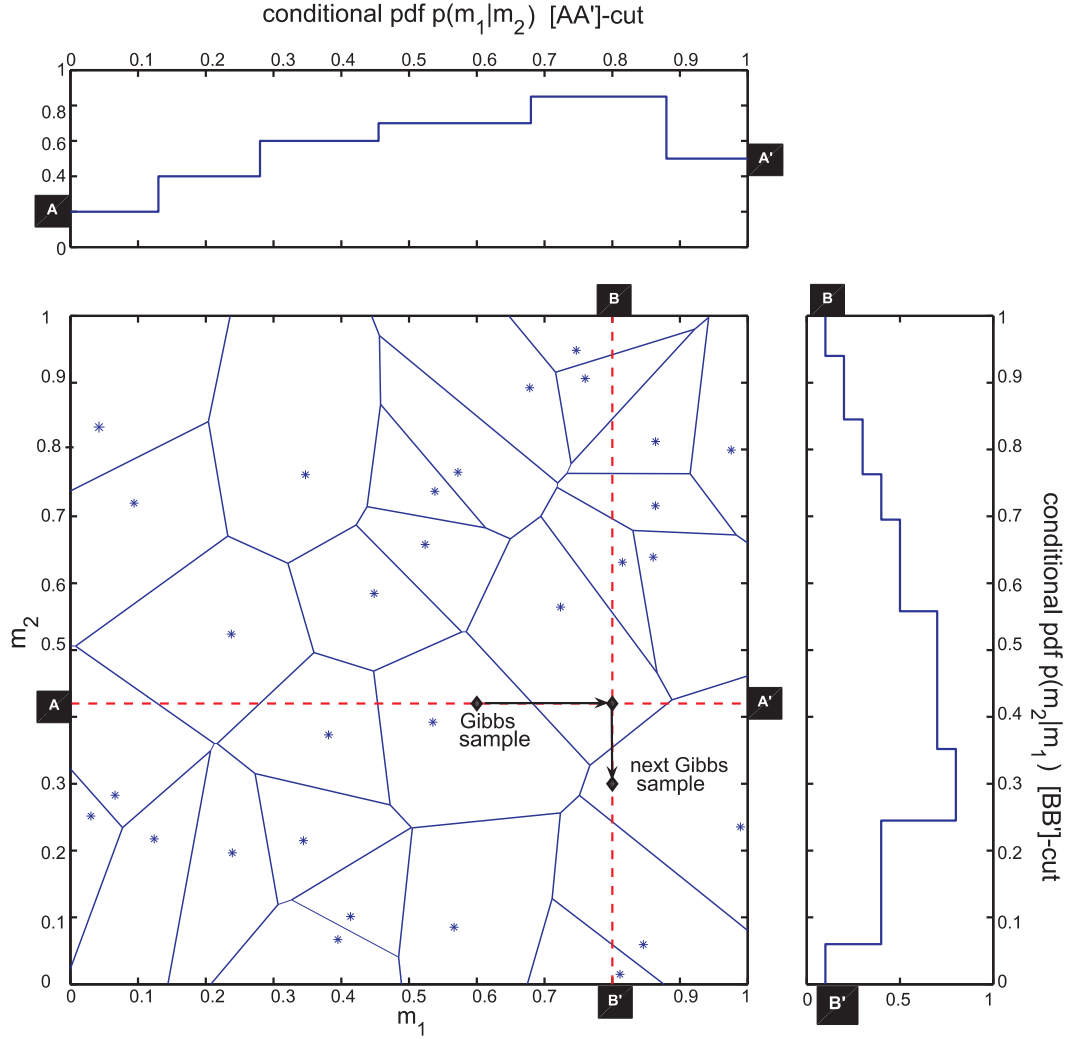


Figure 3.2: Voronoi cells and a single GS step for a simple 2 parameter search space. Conditional PPD's used in the Gibbs step for the given conditional cut lines (AA' and BB') are shown on the top and to the right of the Voronoi diagram. GA and Gibbs samples are represented by (*) and (♦) , respectively.

GA, and (d) hybrid GA-MCMC method, respectively. Exhaustive search results are assumed to have a dense enough grid to give the true distributions and will be used as the benchmark. As expected, the Gibbs sampler results are close to the true distribution but requires 70×10^3 (70k) samples to converge. The GA uses 15k samples (5k is enough to get the MAP solution). The distributions are clearly not accurate, however, as a global optimizer it does its job of minimizing $\phi(\mathbf{m})$ and obtaining MAP very fast. The GA sample histograms presented here are not

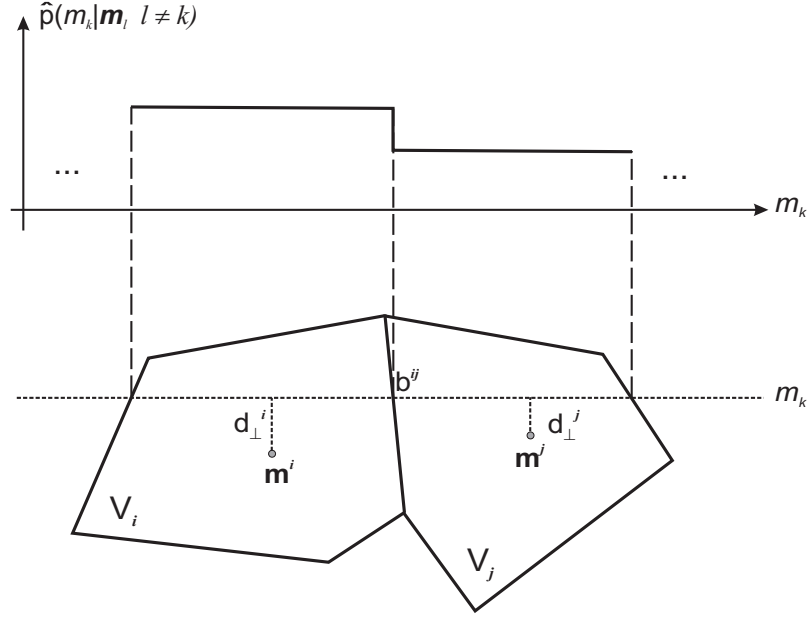


Figure 3.3: Two adjacent Voronoi cells V_i and V_j intersecting a conditional line in the k th dimension. \mathbf{m}^i and \mathbf{m}^j are the corresponding GA samples. The conditional approximate PPD which is constant except for the cell boundary intersection is given above the Voronoi cell structure.

unique. Every GA run will result in a different set of curves, without any specific sampling density $p_s(\mathbf{m}|\mathbf{d})$. The hybrid method actually uses the 15k GA samples obtained in (c) to perform the Voronoi decomposition. When a fast Gibbs resampling is performed on the approximate PPD, results comparable to the conventional MCMC solution is obtained. A Gibbs resampling of just 20k samples is sufficient to calculate the MC integral accurately (40k is used in (d)). It should be noted that (d) is extracted using the forward model samples obtained in (c). All information about the search space comes from the GA samples and the hybrid method makes the information hidden in the GA set available for MC integration through Voronoi decomposition.

Figs. 3.5 provides further comparison between the benchmark exhaustive search and the hybrid method results. The off-diagonal plots are the 2-D marginal posterior densities, while 1-D parameter PPD's are given in diagonal plots. The results are given in terms of highest posterior density (HPD) regions [32]. Full

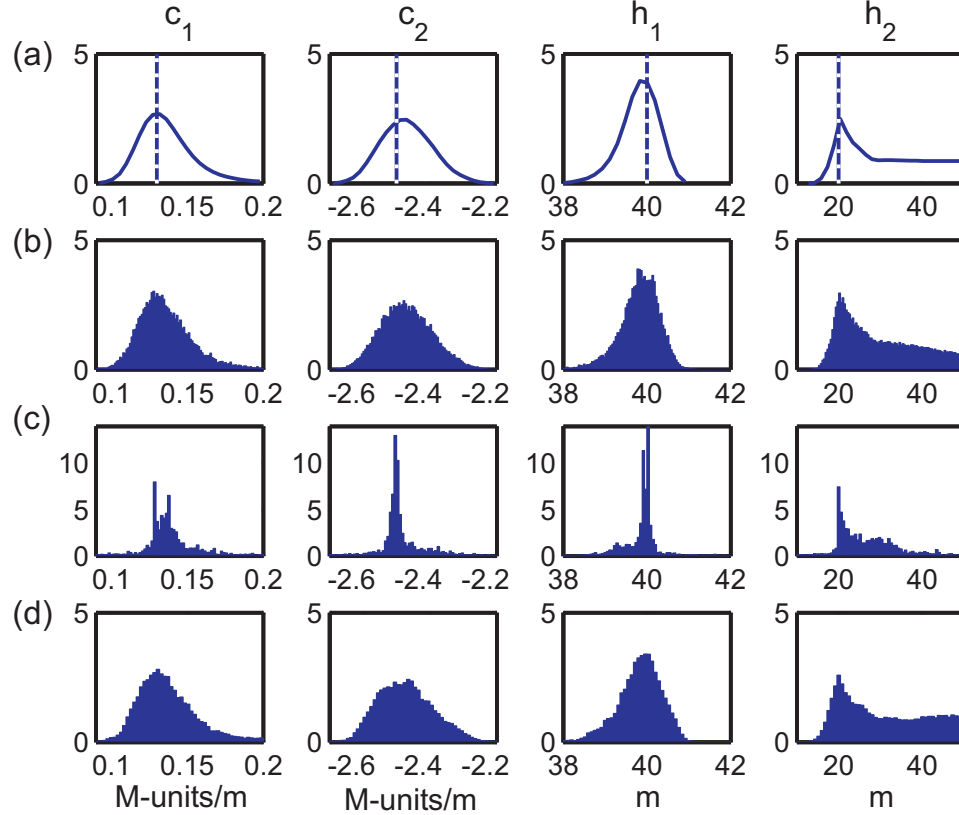


Figure 3.4: Marginal posterior probability distributions for the synthetic test case. Vertical lines show the true values of the parameters. (a) Exhaustive search, (b) Metropolis sampler (MCMC), (c) GA, and (d) hybrid GA-MCMC using 15k GA and 40k Gibbs samples.

Bayesian solutions in terms of posterior densities may be important in many cases and give information about the inversion quality. These marginal distributions and the inter-parameter correlations shown in 2-D plots may also help in understanding the underlying physics. For example the last parameter, inversion layer thickness, shows a highly non-Gaussian behavior with a high posterior probability from 15 m to 50 m. The physical explanation is that, since the selected inversion layer is very strong it will trap all of the EM signal provided that the layer has at least a certain thickness (25 m in these plots). Therefore, having an environment with a thicker inversion layer will not affect the sea clutter, so any model with $h_2 > 25$ m appears as equally likely in the plot. Hence, just using the mean (MMSE) or MAP solutions may be misleading and can have significant errors. Also notice how

some parameters are strongly correlated, such as the inversion layer slope c_2 and the base layer height h_1 .

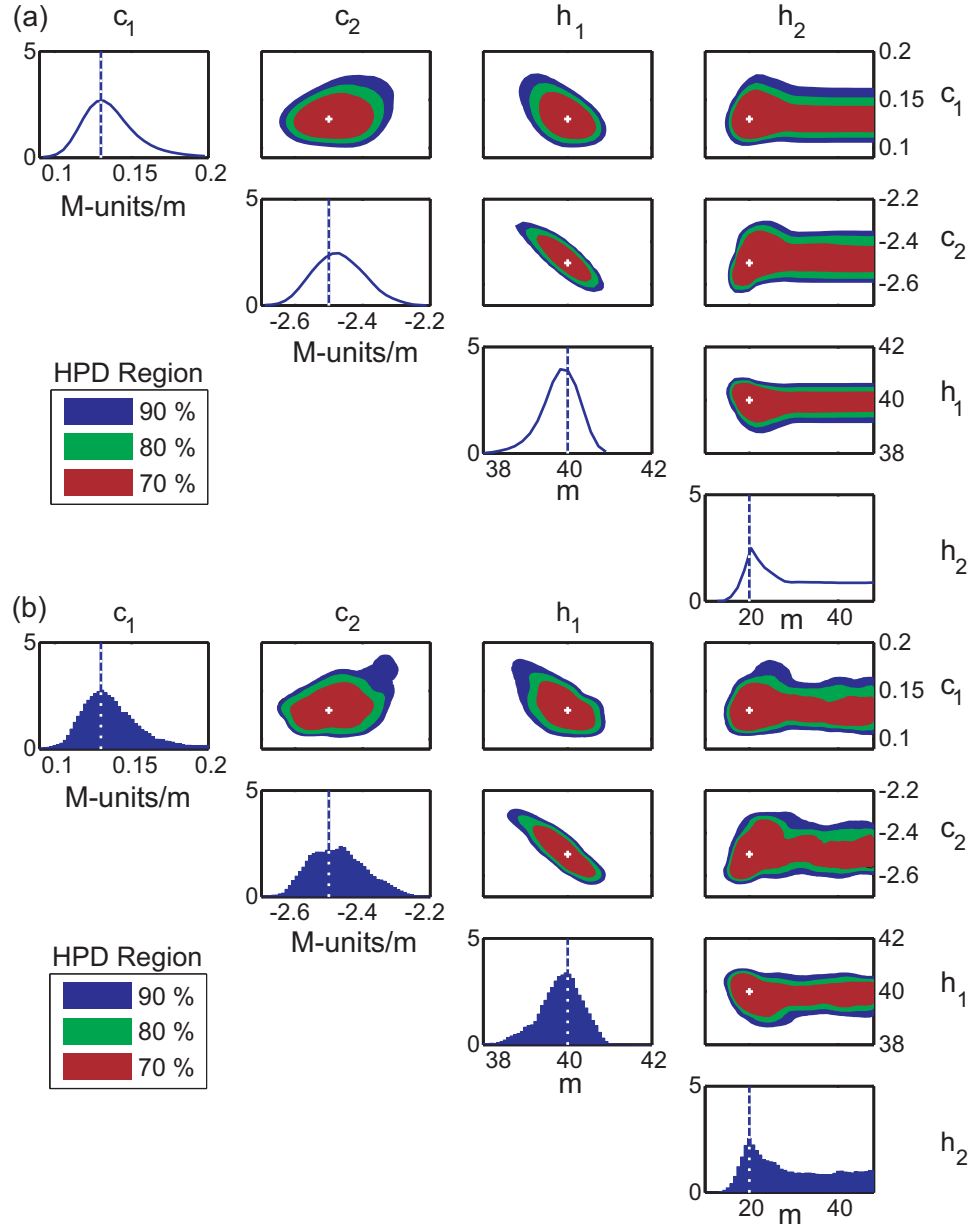


Figure 3.5: Both 1-D marginal (diagonal) and 2-D marginal (upper diagonal) PPD's for the synthetic test case obtained by (a) exhaustive search and (b) hybrid GA-MCMC. Vertical lines (in 1-D plots) and crosses (in 2-D plots) show the true values of the parameters.

One drawback of the hybrid method is a lack of rigorous convergence criterion. Because of its MCMC nature, the resampling converges to the sampling

density. However, it is sampling the approximate density $\hat{p}(\mathbf{m}|\mathbf{d})$, not the real $p(\mathbf{m}|\mathbf{d})$. Therefore, two separate conditions must be met simultaneously for the convergence of the hybrid method:

1. *Convergence in GA*: The set of GA samples converges when $\hat{p}(\mathbf{m}|\mathbf{d})$ obtained from the Voronoi decomposition of the GA sample set is close enough to the real PPD to yield sufficiently accurate MC integral calculations, assuming a perfect Gibbs resampling.
2. *Convergence in GS*: The set of Gibbs samples obtained during the resampling phase converges if the sample histograms obtained by this set is close to $\hat{p}(\mathbf{m}|\mathbf{d})$.

Hence, a poor Gibbs resampling after a perfect Voronoi decomposition or a perfect Gibbs resampling on a poor Voronoi lattice may both end up with poor estimates.

Fig. 3.6 shows how the estimated 1-D marginal PPD's evolve to their true distributions with increasing GA samples for a fixed number of Gibbs samples (40k). The metric (D) used to check the quality of the inversion result is calculated for each parameter as:

$$D_j = \max_{m_j} |P(m_j|\mathbf{d}) - P_{\text{TRUE}}(m_j|\mathbf{d})|, \quad (3.25)$$

where $P(m_j|\mathbf{d})$ and $P_{\text{TRUE}}(m_j|\mathbf{d})$ represent the cumulative marginal distribution functions of the j th model parameter for the hybrid method and the exhaustive search result, respectively. This metric is similar to the Kolmogorov-Smirnov test statistic [33]. Similarly, Fig. 3.7 explores the effect of the number of Gibbs samples in the resampling phase for a fixed Voronoi decomposition obtained from 15k GA points. Note how quickly the 1-D marginals obtained by GS converge to the approximate marginal PPD (about 5k is enough) as long as $\hat{p}(\mathbf{m}|\mathbf{d})$ is a good Voronoi approximation to the real PPD.

The convergence plots for the hybrid method are given on Fig. 3.8. Fig. 3.8 (a) is obtained by performing multiple inversions using GA sample sizes varying

from 10 to 25k. For each GA size the inversion is repeated 40 times and the mean D value is used. Note how D improves as GA sample size is increased. Since an adequate number of Gibbs samples are used in the resampling phase, most of the error comes from the difference between the true and the approximate PPD's. Fig. 3.8 (b) shows the convergence in GS with different Gibbs sample sizes varying from 10 to 200k. Again each simulation is repeated 40 times and the mean D is used. Given enough samples, the Gibbs sampling converges to the Voronoi-approximated PPD. Due to the inherent residual between the Voronoi approximate and the real PPD, increasing the GS sample size (here past about 20k) will not improve convergence.

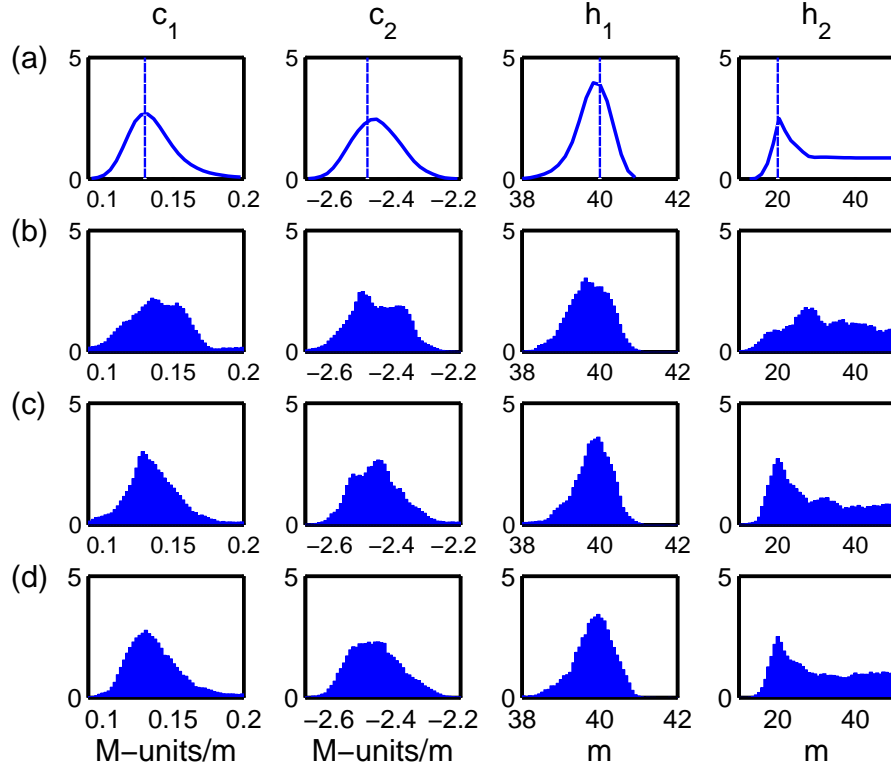


Figure 3.6: Convergence in GA: Effect of GA sample size on 1-D marginal posterior densities for a 40k Gibbs sample size. Distributions calculated using (a) exhaustive search (true distribution) and the hybrid method with (b) 1k, (c) 5k, and (d) 15k GA samples. Vertical lines represent the true values.

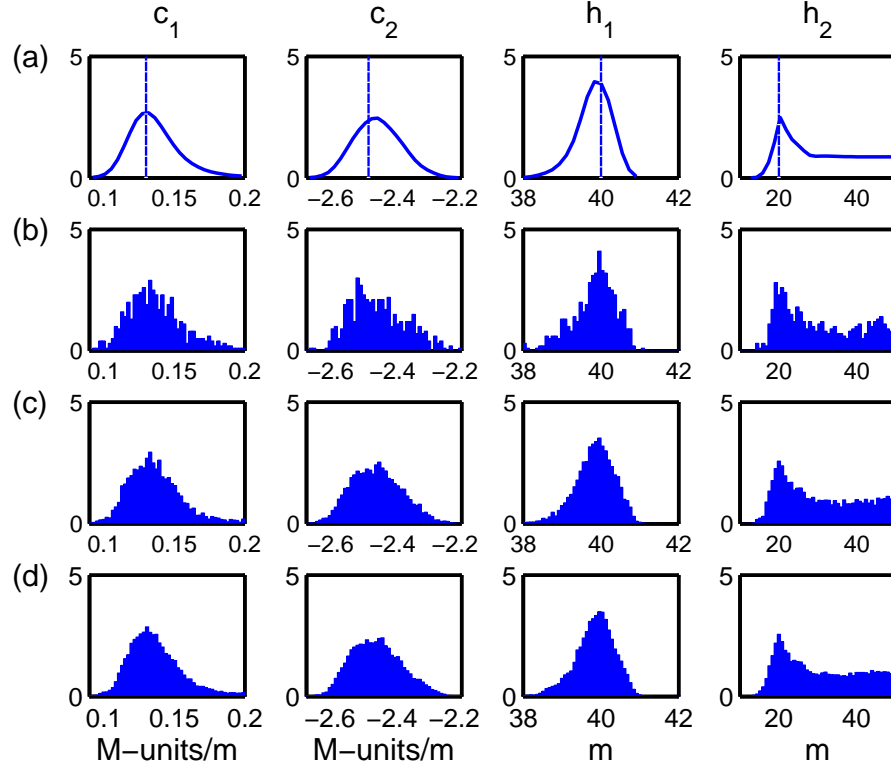


Figure 3.7: Convergence in GS: Effect of GS sample size on 1-D marginal posterior densities for a 15k GA sample size. Distributions calculated using (a) exhaustive search (true distribution) and the hybrid method with (b) 1k, (c) 5k, and (d) 20k Gibbs samples. Vertical lines represent the true values.

3.4.2 Wallops'98 Data

To further demonstrate the capabilities and limitations of the hybrid method, a range-dependent environmental model comprising of sixteen parameters is employed during the inversion of the 1998 Wallops island experiment data collected by the Naval Surface Warfare Center, Dahlgren Division. The radar clutter was gathered by the Space Range Radar (SPANDAR). Radar and environmental model parameters are both provided in Table 3.1. Range dependent M-profiles were measured by a helicopter provided by the Johns-Hopkins University, Applied Physics Laboratory (JHU-APL). Data used in the inversion was taken during a surface-based ducting event on April 2, 1998 [7, 8].

A range dependent inversion is achieved by defining vertical, four pa-

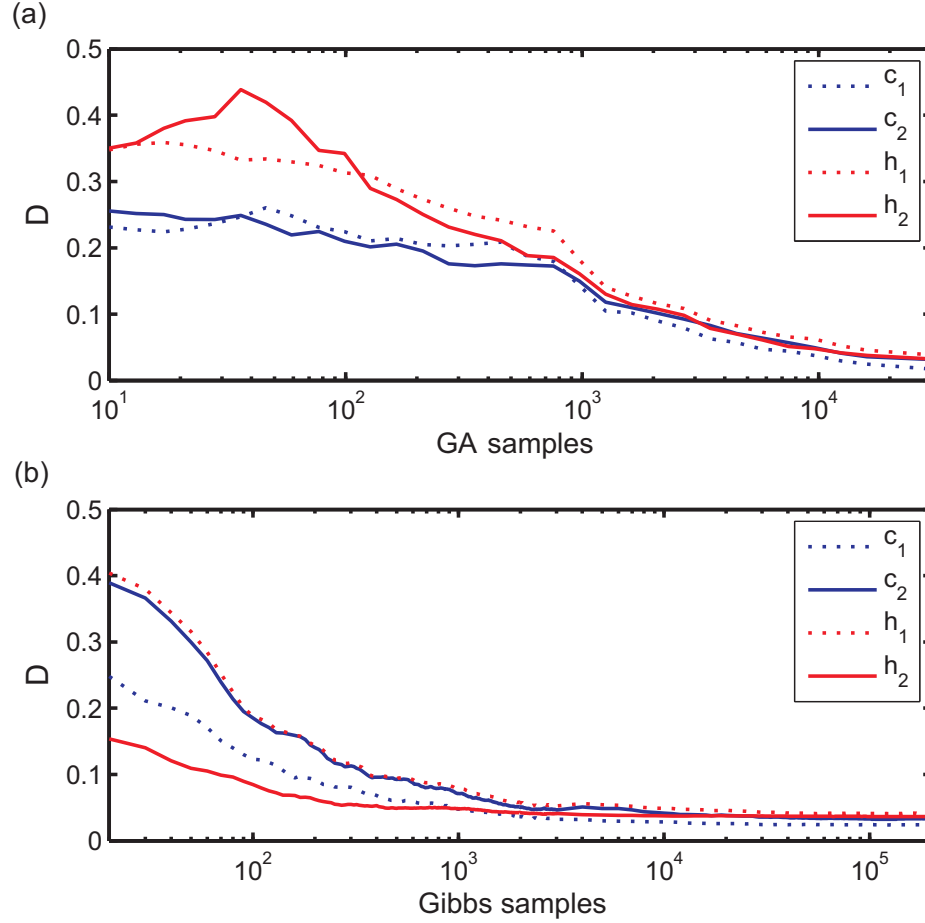


Figure 3.8: Convergence of the hybrid method. D for each parameter as a function of (a) GA sample size for a 40k Gibbs sample size and (b) Gibbs sample size for a 15k GA sample size .

parameter tri-linear M-profiles at certain ranges (0, 20, 40, and 60 km) and linearly interpolating the parameters in between, see Fig. 3.9. Slopes for both the first and the second layers can be negative and positive to give more flexibility in the modeling. Hence, they are only referred to by their layer numbers. Layer slopes at different ranges can vary independent of each other. On the contrary, a Markovian structure is used for the layer heights with a maximum of 30 m variation relative to the height value at the previous range.

It has been shown by [34] that for ranges larger than 30 km, the lateral homogeneity assumption can result in significant errors. They suggest using multiple profiles for long range applications. In the paper by [35], it is suggested

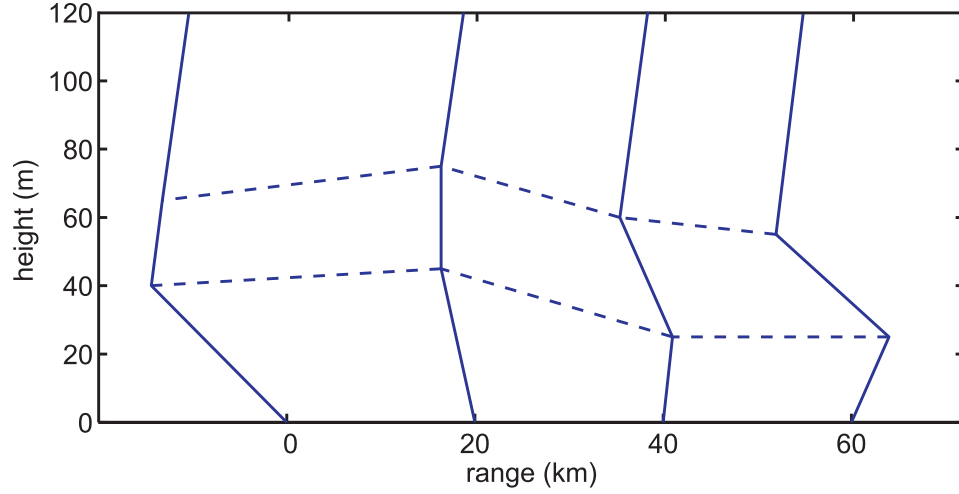


Figure 3.9: An example of range-dependent sixteen parameter M-profile with four parameters per 20 km. Vertical profile at any given range is calculated by linear interpolation of both the slopes and the layer thicknesses.

that a range independent assumption for long ranges leads to significant errors in propagation factor 40% of the time and the results by [34] are optimistic. Hence, in this work a range-dependent approach with multiple profiles, each 20 km apart, is adopted. The parameters and their bounds are given in Table 3.3 along with the MAP solution obtained by GA. Lower and upper bounds are selected in consistency with [6] and [36].

Inversion results are given in Figs. 3.10 – 3.13. Estimated range-dependent M-profile (MAP solution) is given in Fig. 3.10(a). This solution is similar to the ones obtained by [8] and [13] and agrees well with the helicopter measured profile (Fig. 3.10(a)). Although the helicopter profiles give a good approximation to the environment, they might not represent ground truth at the time the clutter is measured. These profiles are collected while the helicopter flies in and out radially along 150° azimuth with a saw-tooth up-and-down motion to measure the range-height dependent refractivity. Each measurement takes about 25 min., comparable to the 30 min.-limit by [6]. For the analyzed case the helicopter fly-time is between 13:19–13:49pm EST and the clutter return is measured at 13:40pm EST. The sharp gradient around 60 km range disappears at the next helicopter measurement taken

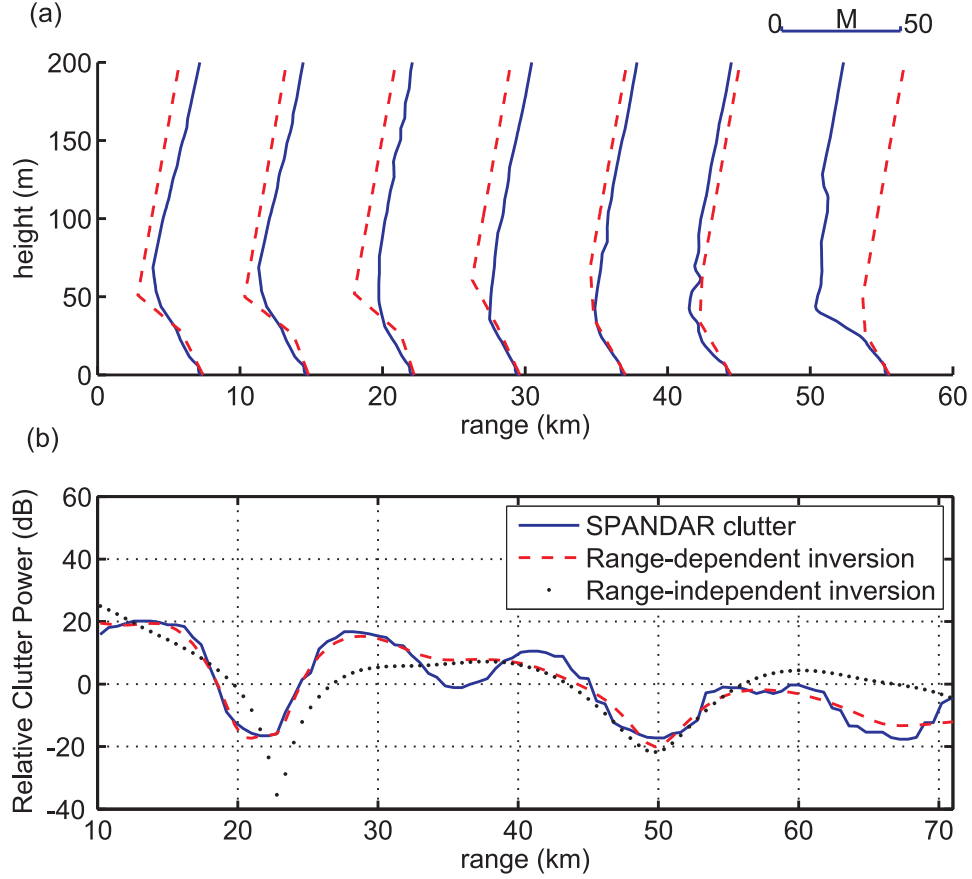


Figure 3.10: Inversion results for the Wallops island experiment. (a) estimated (dashed lines) and helicopter measured (solid lines) profiles at various ranges and (b) clutter measured by SPANDAR together with the clutter that would have been obtained from the estimated range-dependent and range-independent environments.

between 13:51–14:14pm EST [8]. So there are discrepancies between helicopter-measured and clutter-inferred profiles. In fact, the absolute mean error at 0–70 km between the helicopter and SPANDAR clutter is quite large (11.9 dB). This error value drops to 6.8 and 2.6 dB, respectively between the SPANDAR and the range-independent profile and between the SPANDAR and the range-dependent profile clutter returns. As expected, the range-dependent profile matches the relative clutter power of the SPANDAR radar (Fig. 3.10(b)) better than the range independent inversion [12] due to the increased degrees of freedom.

The environmental posterior density is given in Fig. 3.11(a). Since the

full PPD is 16-D, only 1-D (diagonal plots) and 2-D (upper diagonal) marginal densities calculated using (3.10) are given. Some of the parameters such as m_{10} , m_{13} , and m_{14} have a highly non-Gaussian marginals, while others such as m_2 , m_3 , and m_9 have Gaussian-like features. The highly skewed 1-D marginals given for m_{10} and m_{14} are encountered frequently with the refractivity slope pdf's. The reason is that the slope very rarely exceeds values such as 0.3–0.4 M-units/m and usually is concentrated around values such as 0.118 M-units/m (standard atmosphere) and 0.13 M-units/m. This creates a sharp peak for the positive end of the spectrum since the negative slope values can be in excess of the -2 M-units/m, usually with a quickly decreasing probability. The result is a pdf structure similar to the ones obtained here. In fact [9] uses such a pdf as prior density to do importance sampling.

Only 13 out of 16 parameters are given in Fig. 3.11(a). The height parameters of the second layers m_8 , m_{12} , and m_{16} are omitted, as they are not important (see discussion about Fig.3.4. Since clutter is mostly due to the EM signal trapped inside the duct, it mostly contains information about the parameters inside the duct, making the second layer heights poorly determined except for very close ranges. To demonstrate this, normalized error function $\phi(\mathbf{m})/\phi(\mathbf{m}_{MAP})$ for various conditional planes are given in Fig. 3.11(b). These curves are obtained by fixing other parameters to their MAP values and calculating $\phi(\mathbf{m})$ while varying only two parameters at a time. Except for the bottom plots all the plots show quickly varying complex patterns whereas the last ones are flat since the horizontal axis for these is either m_8 , m_{12} , or m_{16} (second layer heights). Some plots such as m_1 vs. m_{12} have zero likelihood regions since the height parameters which are Δh at 20, 40, and 60 km cannot be less than values that would make the actual layer thickness negative.

Therefore, only 13 parameters are used in the resampling phase. This decreases computation time and reduces misleading results. For a uniformly distributed parameter the hybrid method will require much larger numbers of initial

GA samples. This can be explained using the conditional plot of m_1 vs. m_{16} in Fig. 3.11(b). Assume we have only two samples on the plane with $[m_1^1, m_{16}^1] = [-1.5 \ -20]$ and $[m_1^2, m_{16}^2] = [-0.5 \ 20]$. The first sample m^1 has a low likelihood whereas m^2 has a much higher value, entirely due to the difference in m_1 . Hence, resampling after Voronoi decomposition of this sparsely sampled space will result in a non-uniform marginal for m_{16} . An interesting observation is that the other parameter m_1 is affected much less severely and indeed increasing the number of samples slightly will be enough to obtain an accurate PPD for m_1 , whereas m_{16} will require much denser Voronoi cell structures. This can be problematic as the dimension size is increased. A sparse mesh will result in poor results for the uniformly distributed parameters with minimal effect on the results for other parameters. However in RFC, due to the physics of the inversion problem, we know *a priori* the uniformly distributed parameters and do not include them.

The environmental statistics can be projected into statistics for user parameters (see Section II). One typical parameter of interest to an end-user is the propagation factor F. The results in Fig. 3.12 are obtained from the parameter PPD in Fig. 3.11. It shows the PPD for F at ranges (a) 18, (b) 40, and (c) 60 km. Contour plots show the PPD of F for height values between 0–200 m, with the MAP solution (dashed white). Horizontal lines represent the three altitudes analyzed in detail in the small plots shown next to the color plots. Comparison of plots at the same range and different altitudes reveals some important aspects of RFC.

First, the propagation factor PPDs inside the duct (at 20 m) are sharper than those outside the duct (100 and 180 m). This is expected since we used the sea clutter which is usually affected only by the lower portions of the atmosphere to infer the environment. The PPDs do also become flatter with increasing range. Note how the error made by using the standard atmospheric assumption (black dashed lines) increases with range, especially inside the duct. At $[H, R] = [20 \text{ m}, 18 \text{ km}]$ all three curves (MAP, helicopter profile, and standard atmosphere)

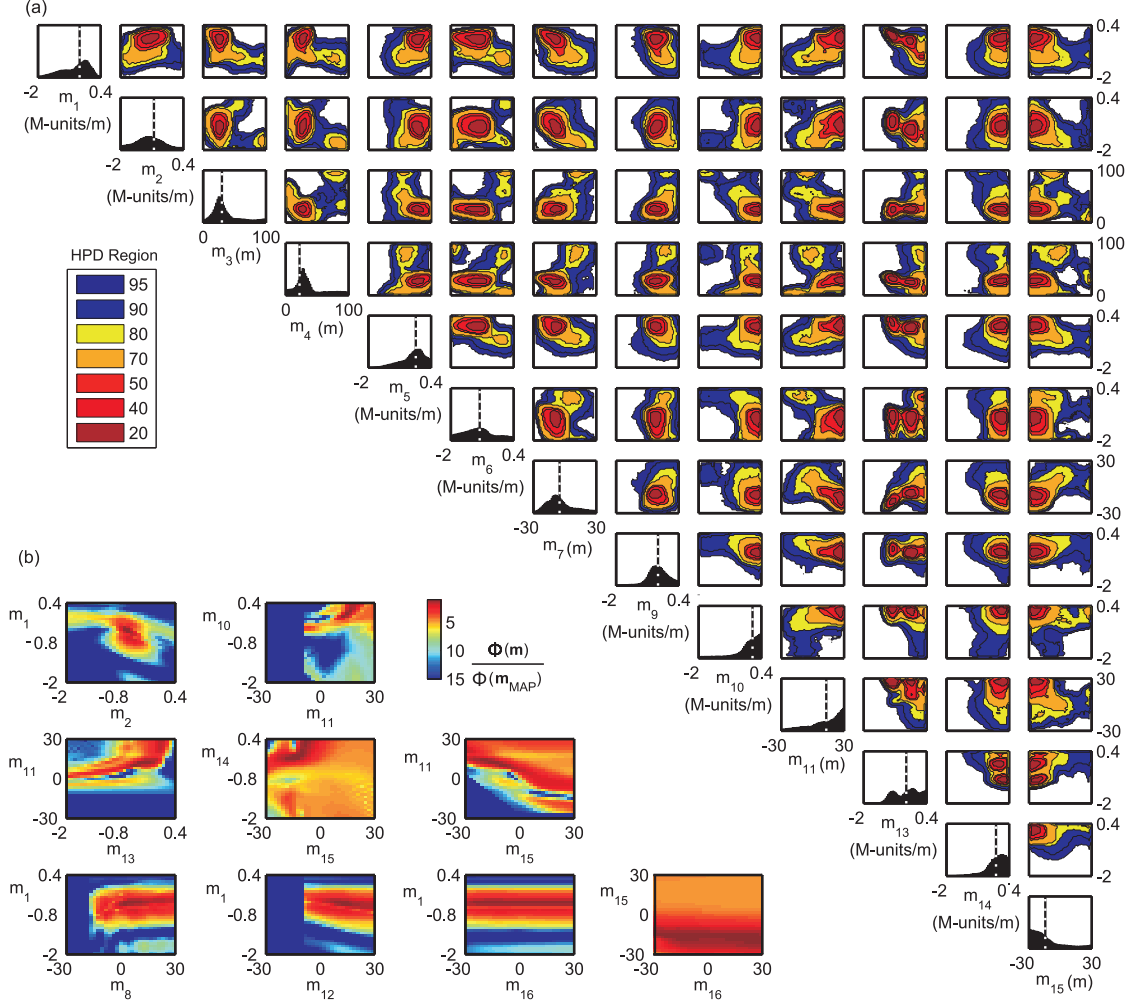


Figure 3.11: Marginal and conditional distributions. (a) 1-D (diagonal) and 2-D (upper diagonal) posterior probability distributions in terms of percent HPD, for the range-dependent SPANDAR data inversion. 13 parameters (m_1-7 , m_9-11 , m_{13-15}) out of 16 are given. Vertical lines in the 1-D plots show the GA MAP solution. (b) Normalized error function for various conditional planes. Each 2-D plot is obtained by fixing the other 14 parameters to their MAP values.

are almost identical whereas standard atmospheric assumption leads to more than 40 dB error for $[H, R] = [20 \text{ m}, 60 \text{ km}]$ while MAP and helicopter profile comply with the underlying PPD. Finally, the difference between the helicopter profile and MAP tends to be larger outside the duct.

Similar results are obtained for F at two altitudes in Fig. 3.13 at (a) 20 m and (b) 100 m, inside and outside the duct, respectively. Color plots again show

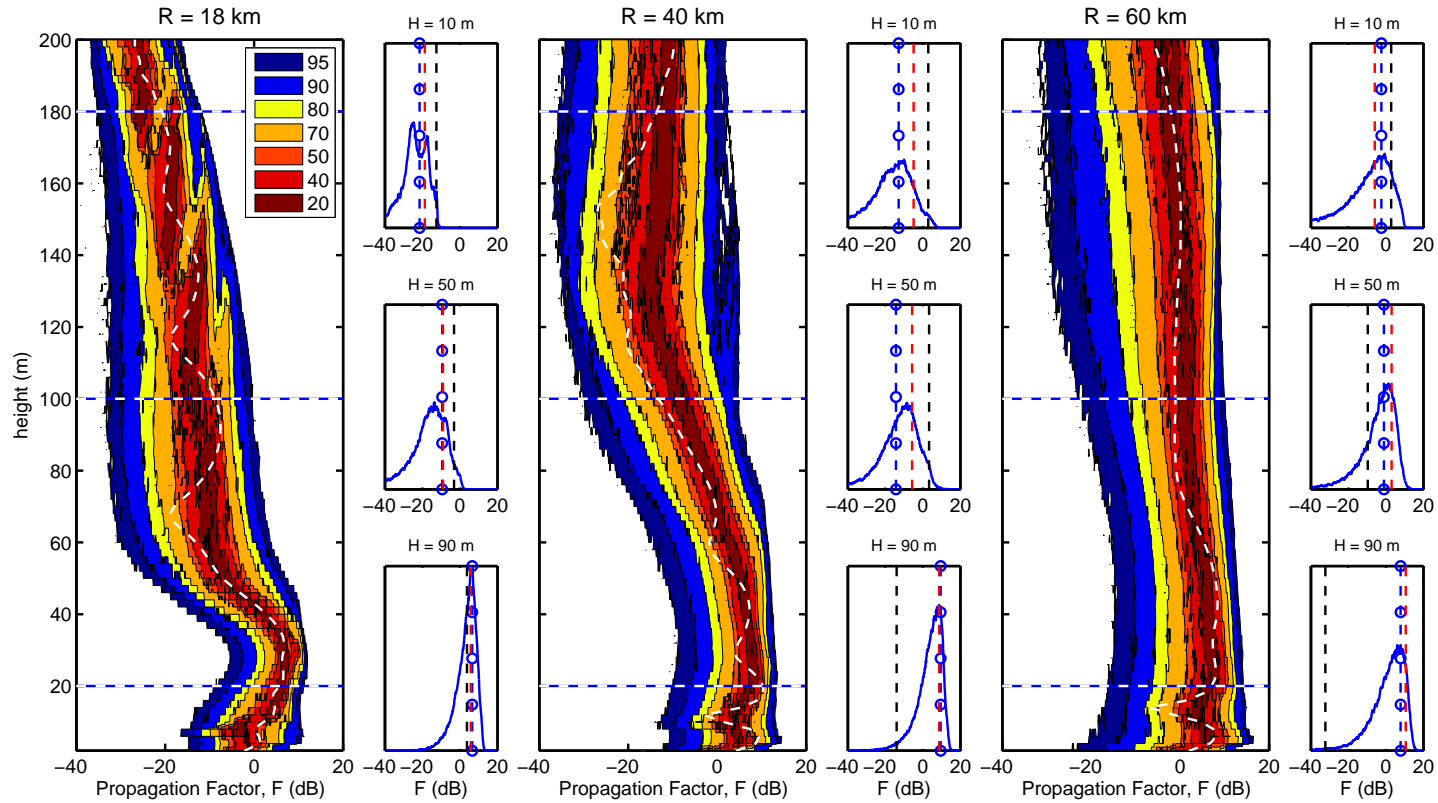


Figure 3.12: Posterior probability densities for propagation factor F at three different ranges: (a) 18, (b) 40, and (c) 60 km. Color plots show the PPD of F for height values between 0 m and 200 m in terms of percent HPD, with the MAP solution (dashed white). Horizontal lines represent the three altitudes analyzed in detail in the small plots shown next to the color plots at heights 180, 100, and 20 m, respectively from top to bottom. Vertical lines in the small plots represent the values of F at the corresponding height and range for the MAP solution (blue line with circles), helicopter measurement (red), and standard atmospheric assumption (black).

Table 3.3: Wallops'98 Experiment: Model Parameters

| Model Parameter | Units | MAP Estimate | Lower Bound | Upper Bound |
|----------------------------------|-----------|-----------------|----------------|----------------|
| m_1 : c_1 at 0 km | M-units/m | -0.404 | -2 | 0.4 |
| m_2 : c_2 at 0 km | M-units/m | -0.721 | -2 | 0.4 |
| m_3 : h_1 at 0 km | m | 29.98 | 0 | 100 |
| m_4 : h_2 at 0 km | m | 21.94 | 0 | 100 |
| m_5 : c_1 at 20 km | M-units/m | -0.185 | -2 | 0.4 |
| m_6 : c_2 at 20 km | M-units/m | -0.895 | -2 | 0.4 |
| m_7 : Δh_1 at 20 km | m | -5.03 | -30 | 30 |
| m_8 : Δh_2 at 20 km | m | 3.02 | -30 | 30 |
| m_9 : c_1 at 40 km | M-units/m | -0.391 | -2 | 0.4 |
| m_{10} : c_2 at 40 km | M-units/m | 0.060 | -2 | 0.4 |
| m_{11} : Δh_1 at 40 km | m | 13.18 | -30 | 30 |
| m_{12} : Δh_2 at 40 km | m | 9.94 | -30 | 30 |
| m_{13} : c_1 at 60 km | M-units/m | -0.373 | -2 | 0.4 |
| m_{14} : c_2 at 60 km | M-units/m | -0.098 | -2 | 0.4 |
| m_{15} : Δh_1 at 60 km | m | -14.25 | -30 | 30 |
| m_{16} : Δh_2 at 60 km | m | -14.27 | -30 | 30 |

the PPD of F for ranges between 0 km and 90 km in terms of percent HPD, with the dashed white line showing the MAP solution. The increase in the variance of F as a function of range can clearly be seen for both inside and outside the duct cases. The variance of 100 m case is also larger than the 20 m case as also witnessed in Fig. 3.12. It should be noted that the helicopter and MAP solution results almost always conform with the underlying density even when they are not same. Plots such as these can be used by the radar operator to update radar performance or even be included in detection algorithms as a fluctuation in the returned signal due to the atmosphere, similar to the Swerling models [1].

3.5 Conclusion

A hybrid genetic algorithm – Markov chain Monte Carlo (GA-MCMC) method has been used for statistical maritime radar performance estimation under non-standard propagation conditions. Statistical refractivity-from-clutter (RFC)

inversion is used to gather information about the environment, such as the range-dependent vertical structure of the atmospheric index of refraction, and then these environmental uncertainties are used to estimate parameters-of-interest to be used by the radar operator.

As a forward model, a fast Fourier transform split-step parabolic equation (FFT-SSPE) approximation to the wave equation was used to propagate the electromagnetic signal in complex environments. The hybrid method uses fewer forward model calculations than a classical MCMC while obtaining more accurate distributions than GA. This enables inclusion of more unknown parameters and range-dependent atmospheric models. The capabilities of the technique were illustrated for a sixteen dimensional range-dependent inversion.

3.6 Acknowledgment

The authors would like to thank Ted Rogers, SPAWAR, San Diego, CA, for providing the SPANDAR clutter maps and Daniel Dockery, John Hopkins University, Applied Physics Laboratory, Baltimore, MD, for providing the helicopter refractivity measurements. This work was supported by the Office of Naval Research under grant N00014-05-1-0369.

The text of Chapter Three is in full a reprint of the material as it appears in Caglar Yardim, Peter Gerstoft, and William S. Hodgkiss, "Statistical maritime radar duct estimation using a hybrid genetic algorithms - Markov chain Monte Carlo method," *Radio Science*, in press 2007. The dissertation author was the primary researcher and author, and the co-authors listed in this publication directed and supervised the research which forms the basis for this chapter.

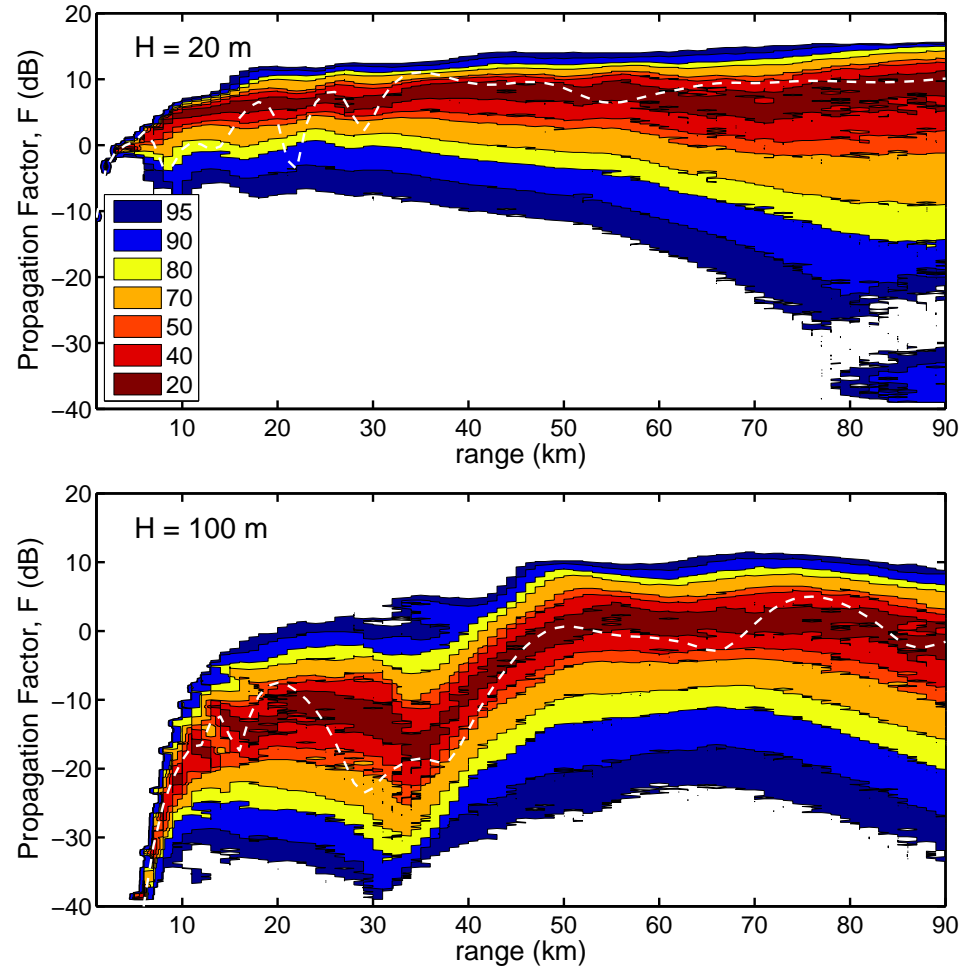


Figure 3.13: Posterior probability densities for propagation factor F at (a) 20 and (b) 100 m altitudes. Color plots show the PPD of F for ranges between 0–90 km in terms of percent HPD, with the dashed white line showing the MAP solution.

Bibliography

- [1] Merrill I. Skolnik. *Introduction to Radar Systems*. McGraw–Hill, New York, third edition, 2001.
- [2] J. R. Rowland and S. M. Babin. Fine-scale measurements of microwave profiles with helicopter and low cost rocket probes. *Johns Hopkins APL Tech. Dig.*, 8 (4):413–417, 1987.
- [3] E. R. Thews. Timely prediction of low-altitude radar performance in operational environments using *in situ* atmospheric refractivity data. *IEE Proc.*, 137 (F-2):89–94, 1990.
- [4] Richard M. Hodur. The naval research laboratory’s coupled ocean/atmosphere mesoscale prediction system (COAMPS). *Monthly Weather Review*, 125(7):1414–1430, 1996.
- [5] Steven M. Babin. Surface duct height distributions for Wallops island, Virginia, 1985–1994. *Journal of Applied Meteorology*, 35 (1):86–93, 1996.
- [6] L. Ted Rogers. Effects of variability of atmospheric refractivity on propagation estimates. *IEEE Trans. Antennas Propagat.*, 44 (4):460–465, 1996.
- [7] L. Ted Rogers, C. P. Hattan, and J. K. Stapleton. Estimating evaporation duct heights from radar sea echo. *Radio Science*, 35 (4):955–966, 2000. doi:10.1029/1999RS002275.
- [8] Peter Gerstoft, L. T. Rogers, J. Krolik, and W. S. Hodgkiss. Inversion for refractivity parameters from radar sea clutter. *Radio Science*, 38 (3):1–22, 2003. doi:10.1029/2002RS002640.
- [9] Peter Gerstoft, W. S. Hodgkiss, L. T. Rogers, and M. Jablecki. Probability distribution of low altitude propagation loss from radar sea-clutter data. *Radio Science*, 39:1–9, 2004. doi:10.1029/2004RS003077.
- [10] Amalia Barrios. Estimation of surface-based duct parameters from surface clutter using a ray trace approach. *Radio Science*, 39 RS6013:1–15, 2004. doi:10.1029/2003RS002930.

- [11] L. Ted Rogers, Michael Jablecki, and Peter Gerstoft. Posterior distributions of a statistic of propagation loss inferred from radar sea clutter. *Radio Science*, 40 (6):1–14, 2005. doi:10.1029/2004RS003112.
- [12] Caglar Yardim, Peter Gerstoft, and William S. Hodgkiss. Estimation of radio refractivity from radar clutter using Bayesian Monte Carlo analysis. *IEEE Trans. Antennas Propagat.*, 54(4):1318–1327, 2006.
- [13] S. Vasudevan, R.H. Anderson, S. Kraut, P. Gerstoft, L.T. Rogers, and J.L. Krolik. Recursive Bayesian electromagnetic refractivity estimation from radar sea clutter. *Radio Science*, in press.
- [14] Amalia E. Barrios. A terrain parabolic equation model for propagation in the troposphere. *IEEE Trans. Antennas Propagat.*, 42 (1):90–98, 1994.
- [15] M. Levy. *Parabolic Equation Methods for Electromagnetic Wave Propagation*. The Institution of Electrical Engineers, London, United Kingdom, 2000.
- [16] J. J. K. Ó Ruanaidh and W. J. Fitzgerald. *Numerical Bayesian Methods Applied to Signal Processing*. Statistics and Computing Series. Springer–Verlag, New York, 1996.
- [17] David J. C. MacKay. *Information Theory, Inference and Learning Algorithms*. Cambridge University Press, Cambridge, United Kingdom, 2003.
- [18] H. Jeske. State and limits of prediction methods of radar wave propagation conditions over the sea. *Modern Topics in Microwave Propagation and AirSea Interaction*, A. Zanca, Ed., pages 130–148, 1973.
- [19] R. A. Paulus. Practical application of an evaporation duct model. *Radio Science*, 20 (4):887–896, 1985.
- [20] W. T. Liu, K. B. Katsaros, and J. A. Businger. Bulk parameterization of air-sea exchanges of heat and water vapor including the molecular constraints at the interface. *J. Atmos. Sci.*, 36:1722–1735, 1979.
- [21] John Cook and Stephen Burk. Potential refractivity as a similarity variable. *Boundary-Layer Meteorology*, 58(1–2):151–159, 1992.
- [22] Chen-Fen Huang, Peter Gerstoft, and William S. Hodgkiss. Validation of statistical estimation of transmission loss in the presence of geoacoustic inversion uncertainty. *J. Acoust. Soc. Am.*, 120 (4):1932–1941, 2006.
- [23] Malcolm Sambridge. Geophysical inversion with a neighborhood algorithm - I. searching a parameter space. *Geophys. J. Int.*, 138:479–494, 1999.
- [24] Malcolm Sambridge. Geophysical inversion with a neighborhood algorithm - II. appraising the ensemble. *Geophys. J. Int.*, 138:727–746, 1999.

- [25] Malcolm Sambridge. Finding acceptable models in nonlinear inverse problems using a neighbourhood algorithm. *Inverse Problems*, 17:387–403, 2001.
- [26] Malcolm Sambridge. An ensemble view of earth’s inner core. *Science*, 299(5606):529–530, 2003.
- [27] N. Metropolis, A. W. Rosenbluth, M. N. Rosenbluth, A. H. Teller, and E. Teller. Equation of state calculations by fast computing machines. *J. of Chemical Physics*, 21:1087–1092, 1953.
- [28] W.K. Hastings. Monte Carlo sampling methods using Markov chains and their applications. *Biometrika*, 57:97–109, 1970.
- [29] S. Geman and D. Geman. Stochastic relaxation, Gibbs distributions, and the Bayesian restoration of images. *IEEE Trans. Pattern Anal. Machine Intell.*, 6:721–741, 1984.
- [30] Georgy Voronoi. Nouvelles applications des paramètres continus à la théorie des formes quadratiques. *Journal für die Reine und Angewandte Mathematik*, 133:97–178, 1908.
- [31] Atsuyuki Okabe, Barry Boots, Kokichi Sugihara, and Sung Nok Chiu. *Spatial Tessellations - Concepts and Applications of Voronoi Diagrams*. John Wiley & Sons, New York, 2 edition, 2000.
- [32] George E. P. Box and George C. Tiao. *Bayesian Inference in Statistical Analysis*. Addison–Wesley, New York, 1992.
- [33] W. H. Press, S. A. Teukolsky, W. T. Vetterling, and B.P. Flannery. *Numerical Recipes in C*. Cambridge University Press, Cambridge, United Kingdom, second edition, 1995.
- [34] Julius Goldhirsh and Daniel Dockery. Propagation factor errors due to the assumption of lateral homogeneity. *Radio Science*, 33(2):239–249, 1998. doi:10.1029/97RS03321.
- [35] Ian M. Brooks, Andreas K. Gorocho, and David P. Rogers. Observations of strong surface radar ducts over the Persian gulf. *Journal of Applied Meteorology*, 38:1293–1310, 1999.
- [36] E. E. Gossard and R. G. Strauch. *Radar Observations of Clear Air and Clouds*. Elsevier, New York, 1983.

Tracking Refractivity From Clutter

This paper addresses the problem of tracking the spatial and temporal lower atmospheric variations in maritime environments. The evolution of the range and height-dependent index of refraction is tracked using the sea clutter return from sea-borne radars operating in the region. A split-step fast Fourier transform based parabolic equation approximation to the wave equation is used to compute the clutter return in complex environments with varying index of refraction. In addition, regional statistics are incorporated as prior densities, resulting in a highly nonlinear and non-Gaussian tracking problem. Tracking algorithms such as the extended Kalman, unscented Kalman and particle filters are used for tracking both evaporative and surface-based electromagnetic ducts frequently encountered in marine environments. The tracking performances and applicability of these techniques to different types of refractivity-from-clutter problems are studied using the posterior Cramér-Rao lower bound. Track divergence statistics are analyzed. The results show that while the tracking performance of the Kalman filters is comparable to the particle filters in evaporative duct tracking, it is limited by the high non-linearity of the parabolic equation for the surface-based duct case. Particle filters, on the other hand, prove to be very promising in tracking a wide

range of environments including the abruptly changing ones.

4.1 Introduction

Non-standard electromagnetic propagation due to formation of lower atmospheric sea ducts is a common occurrence in maritime radar applications. Under these conditions, some fundamental system parameters of a sea-borne radar can deviate significantly from their original values specified assuming standard-air (0.118 M-units/m) conditions. These include the variation in the maximum operational range, creation of regions where the radar is practically blind (radar holes), and increased sea surface clutter. Therefore, it is important to predict the real-time 3-D environment the radar is operating in so that the radar operator will at least know the true system limitations and in some cases even compensate for them.

The environment is characterized by the modified refractivity profile (M-profile) and there are many techniques that measure or predict the lower atmospheric index of refraction. Some of the conventional techniques include radiosondes and rocketsondes that estimate the index of refraction by measuring the vertical temperature, humidity and pressure profiles, microwave refractometers that measure the index of refraction using cavity resonators, and meteorological models such as the Coupled Ocean/Atmospheric Mesoscale Prediction System (COAMPS) that give M-profile forecasts [1–3]. There also are other techniques that can refer the refractivity using lidar [4] and GPS [5] measurements.

However, it also is possible to predict the duct properties using the radar itself. When launched at a low elevation angle, the electromagnetic signal will be trapped within the duct which can be taken as a range-dependent leaky waveguide bounded from below by the sea surface. This will result in multiple reflections and strong interaction with the surface which in turn will result in an increase in the sea clutter, forming clutter rings. This normally unwanted portion of the received signal then can be used to infer the environment that gives such a clutter

structure. These techniques can be classified as refractivity-from-clutter (RFC) techniques [6–14]. More detailed discussions about the differences between various RFC schemes can be found in [12, 13].

This paper is a natural extension to these previous RFC methods which compute the 2-D range and height-dependent M-profile for a given azimuth direction. Instead of inverting the environmental parameters for a given azimuth and time, the emphasis here is on tracking both the temporal and spatial evolutions of duct parameters. Throughout this paper, the term spatial evolution is used to represent the evolution of the 2-D M-profile with the rotating azimuth angle of the radar. This is achieved by employing tracking filters. The problem is formulated in a Kalman framework, where the clutter for a given environment is calculated using a split-step fast Fourier transform (FFT) based parabolic equation (PE) approximation to the wave equation [15]. This introduces a high level of nonlinearity in the measurement equation. The problem then is solved by using the following three algorithms [16–18]:

1. Extended Kalman filter (EKF), where the measurement equation is linearized using the first order Taylor series expansion.
2. Unscented Kalman filter (UKF), where the nonlinearity in the parabolic equation is kept but the probability density functions (pdf) are restricted to be Gaussian.
3. Particle filter (PF) or sequential Monte Carlo (SMC), which uses a sequential importance resampling (SIR) or bootstrap filter to track the nonlinear, non-Gaussian system.

4.2 Theory

Two equations are necessary to fully characterize the dynamic system; one that describes the evolution of the lower atmosphere and another that governs

the propagation of the electromagnetic signal in this environment. At a time step k , these equation can be given as:

$$\mathbf{x}_k = \mathbf{F}\mathbf{x}_{k-1} + \mathbf{v}_{k-1} \quad (4.1)$$

$$\mathbf{y}_k = \mathbf{h}(\mathbf{x}_k) + \mathbf{w}_k \quad (4.2)$$

where \mathbf{F} is a known linear function of the state vector \mathbf{x}_k , $\mathbf{h}(\cdot)$ is a known non-linear function of the measurement vector \mathbf{y}_k , \mathbf{v}_k and \mathbf{w}_k are the process and the measurement noise vectors, respectively with

$$\begin{aligned} \mathbb{E}\{\mathbf{v}_k \mathbf{v}_i^T\} &= \mathbf{Q}_k \delta_{ki} & \mathbb{E}\{\mathbf{v}_k \mathbf{w}_i^T\} &= \mathbf{0} \quad \forall i, k \\ \mathbb{E}\{\mathbf{w}_k \mathbf{w}_i^T\} &= \mathbf{R}_k \delta_{ki}. \end{aligned} \quad (4.3)$$

The state vector \mathbf{x}_k is composed of the n_x parameters that describe the complex environment at the step index k . The state vector is constructed depending on the type of the duct (evaporation/surface-based duct (SBD)/mixed) and the appropriate model (range-dependent/independent). The process noise \mathbf{v}_k is taken as a zero-mean Gaussian pdf. The prior density $p(\mathbf{x}_o)$ usually is constructed using the regional statistics. This density must be Gaussian for the Kalman filters. It can be any distribution for the PF. For temporal tracking, k usually is in terms of minutes and for spatial tracking it is in terms of azimuth angle of the rotating radar.

Equation (4.1) is the state equation for the stochastic environmental model. \mathbf{F} is the linear state transition matrix which will be taken as the identity matrix following Section 4.2.2. The main assumption is that the environment is changing slowly compared to the step index. Although the M-profile is not expected to vary considerably in short intervals, sudden fluctuations can occur and the filters will require larger \mathbf{Q}_k to perform adequately in these environments.

Equation (4.2) is the measurement equation and it relates the environment given by \mathbf{x}_k to the radar clutter power \mathbf{y}_k through a highly nonlinear $\mathbf{h}(\cdot)$ function which uses a split-step FFT-PE, see Section 4.2.3. Usually, the nonlinearity is less severe for evaporative ducts, however the degree of nonlinearity and hence

the filter performance still heavily depends on the current location of \mathbf{x}_k on the state-space. \mathbf{w}_k is the logarithm of the sea surface clutter radar cross section (RCS). There are many successful models for the sea clutter distribution. The selection of the appropriate model depends mainly on the grazing angle, radar resolution and sea roughness. Some of the commonly used models include the Rayleigh, Weibull, log-normal and K-distributed sea clutter [19, 20]. Since the Kalman framework requires Gaussian distributions, the model can only be constructed if the RCS is selected as log-normal even if this may not be the most suitable selection among the densities mentioned above. The PF does not have such restrictions and any pdf can be used. However, since it is desirable to compare these filters under the same set of assumptions, sea clutter is taken as log-normal. Note that no other noise terms are used, so all the variation in the signal is represented by the additive \mathbf{w}_k in the logarithmic domain. This assumption is made due to the dominant effect of the increased sea clutter resulting from the entrapment of the electromagnetic signal inside the duct. However, this assumption may have to be modified for a low SNR system. Alternatively, one can use a measurement equation based on the formulation given in [12].

4.2.1 Creation of the 2-D Modified Refractivity Profile from State Variables

Surface-based ducts (SBD) are represented by the commonly used tri-linear M-profiles. Each tri-linear profile requires four parameters: slope and thickness of the base (c_1, h_1) and inversion layers (c_2, h_2). The top layer slope is taken to be constant at 0.118 M-units/m. For range-dependent profiles, the M-profile parameters are defined at n_r range intervals and the values at other ranges are calculated using a cubic fit. Hence, the number of state parameters $n_x = 4n_r$. The

2-D M-profile is calculated using the following procedure:

$$\mathbf{x}_k = [\mathbf{m}_1^T \ \mathbf{m}_2^T \ \dots \ \mathbf{m}_{n_r}^T]^T \quad (4.2.4)$$

$$\mathbf{m}_i = [c_1(r_i) \ c_2(r_i) \ h_1(r_i) \ h_2(r_i)]^T, \quad i = 1, \dots, n_r \quad (4.2.5)$$

$$M(z, r) = M_0 + \begin{cases} \tilde{c}_1 z & \text{if } z \leq \tilde{h}_1 \\ \tilde{c}_1 \tilde{h}_1 + \tilde{c}_2 (z - \tilde{h}_1) & \text{if } \tilde{h}_1 \leq z \leq \tilde{h}_2 \\ \tilde{c}_1 \tilde{h}_1 + \tilde{c}_2 \tilde{h}_2 & \text{if } z \geq \tilde{h}_2 \\ +0.118(z - \tilde{h}_1 - \tilde{h}_2), & \end{cases} \quad (4.2.6)$$

where M_0 is the base refractivity usually taken as 330 M-units/m, \mathbf{m}_i represent the trilinear profiles at n_r different ranges defined in the state vector, \tilde{c}_1 , \tilde{c}_2 , \tilde{h}_1 , and \tilde{h}_2 parameters obtained by a cubic fit for range r .

Evaporative ducts are represented using only the evaporative duct height, which is true when the air and sea temperatures are almost identical with a neutrally buoyant boundary layer. Range-dependence is similarly achieved by defining the duct height at various ranges and interpolating in between using cubic fit. Hence, the number of state parameters $n_x = n_r$ for evaporative duct problems. The 2-D evaporative duct is constructed using the log-linear evaporative duct formula given in [21]:

$$\mathbf{x}_k = [h_d(r_1) \ h_d(r_2) \ \dots \ h_d(r_{n_r})]^T \quad (4.2.7)$$

$$M(z, r) = M_0 + c_o \left(z - \tilde{h}_d \log \frac{z + z_o}{z_o} \right), \quad (4.2.8)$$

where \tilde{h}_d represents the duct height obtained by a cubic fit at range r , the constant c_o and the roughness factor z_o are taken as 0.13 and 1.5×10^{-4} , respectively.

State vector for a mixed type range-dependent/independent duct is created using 4+1 (SBD+evaporation) parameters at each of the n_r ranges. Then the evaporative M-profile is appended to the bottom of the trilinear SBD profile.

4.2.2 State Equation – Environmental Model

The spatial and temporal evolution of the environmental parameters are taken as a first order autoregressive (AR) process with an exponentially decay-

ing autocorrelation function. This structure is selected after the analysis of the helicopter data collected during the Wallops'98 experiment. A helicopter from John Hopkins University (JHU) measured the 2-D M-profile on a fixed path at 150° azimuth from the Space Range Radar (SPANDAR) several times on April 02, 1998 and these measurements are processed into 10 2-D helicopter profiles. Each helicopter profile takes about 24 minutes to measure and is composed of vertical M-profiles every 1.852 km (1 nautical mile) out to 60 km. Therefore, the variation in the M-profiles unfortunately is a combination of both spatial and temporal fluctuations. The variation in two successive M-profiles in range in any given helicopter profile is assumed to be purely spatial to obtain an approximation to the spatial autocorrelation. In other words, the mean helicopter flight time of 40 seconds between two successive M-profiles is ignored.

The best trilinear fit for each of these vertical M-profiles is computed (Fig. 4.1) for each helicopter profile. The autocorrelation for each parameter is calculated using the Yule-Walker method. It also is assumed that these parameters are stationary random processes and hence the spatial autocorrelation only depends on the distance between the two vertical profiles. For the spatial and temporal step sizes used in this paper, the results provided an autocorrelation between 0.97 and 1 for both the layer slopes and thicknesses. The standard deviation for the layer slopes and thicknesses are also observed to vary between 5-100 M-units/km and 1-10 m, respectively for these 10 profiles. However, it should be noted that these values are by no means general. From many previous experiments such as the Variability of Coastal Atmospheric Refractivity (VOCAR) [22], it is known that these values are strong functions of region, season, time of the day and mesoscale atmospheric processes. For example, experiments indicate that Santa Ana-induced (warm and dry offshore winds in Southern and Baja California) SBDs typically have higher spatial variability than the subsidence-induced SBDs [23]. It has been known that duct parameters such as the duct height can stay stable for days, followed by rapid fluctuations [24]. Spatial variability also has similarly chal-

lenging and dynamic patterns as shown during the Wallops'2000 experiment [25]. Hence, different environmental models may be necessary for different applications or regions. One solution can be using multiple models created by observing the most common patterns in the region of interest.

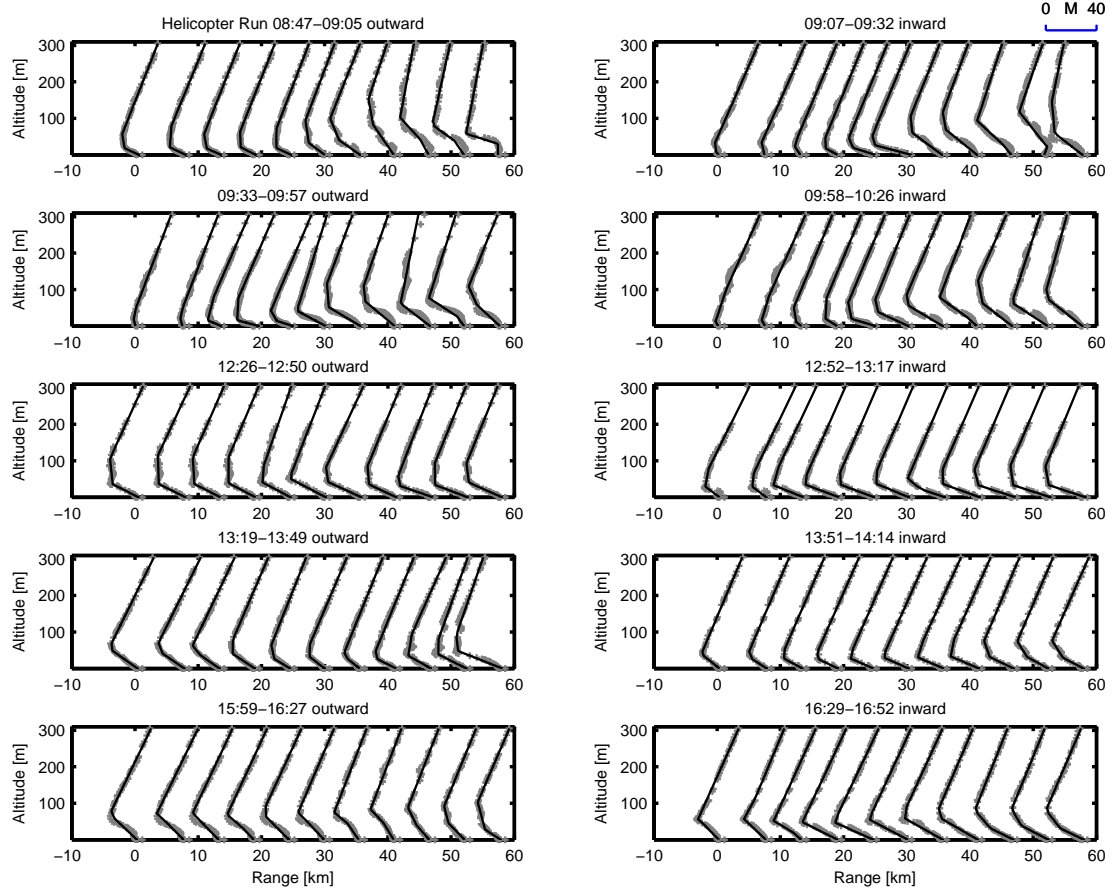


Figure 4.1: Ten 2-D M-profiles measured by JHU helicopter, Wallops'98 experiment (gray) and best trilinear profile fit for each measurement (black).

4.2.3 Measurement Equation – Propagation Model

The measurement equation provides \mathbf{y}_k , the radar clutter power in dB, for an environment described by the state vector \mathbf{x}_k . First the field is propagated

in range using the following recursive split-step FFT PE formula [26]

$$u_k(z, r + \Delta r) = \exp \left[ik_o \Delta r M(\mathbf{x}_k) 10^{-6} \right] \times \mathfrak{F}^{-1} \left\{ \exp \left[i \Delta r \left(\sqrt{k_o^2 - k_z^2} - k_o \right) \right] \mathfrak{F} \{ u_k(z, r) \} \right\} \quad (4.2.9)$$

where $u_k(z, r)$ is the vertical electromagnetic field at range r at step index k , k_o and k_z are the wavenumber and its vertical component, Δr is the range increment in PE, \mathfrak{F} and \mathfrak{F}^{-1} are the Fourier and inverse Fourier transforms and $M(\mathbf{x}_k)$ is the 2-D M-profile $M(z, r)$ computed in Section 4.2.1. Following [7], the clutter power \mathbf{P}_c for low grazing angles can be calculated using

$$\mathbf{P}_c = c \mathbf{L}^{-2}(\mathbf{x}_k) r \sigma^\circ \quad (4.2.10)$$

where c accounts for the constant terms in the radar equation, $\mathbf{L}(\mathbf{x}_k)$ is the one way propagation loss obtained from the electromagnetic field $u_k(z, r)$ calculated at the effective scattering height given as 0.6 times the mean wave height [27] and σ° is the normalized sea surface RCS.

The measurement equation (4.2) can be obtained by representing (4.2.10) in dB with the following definitions

$$\mathbf{y}_k = 10 \log(\mathbf{P}_c) \quad \mathbf{w}_k = 10 \log(\sigma^\circ) \quad (4.2.11)$$

$$\mathbf{h}(\mathbf{x}_k) = -20 \log \mathbf{L}(\mathbf{x}_k) + 10 \log(cr) \quad (4.2.12)$$

where the measurement noise \mathbf{w}_k is additive Gaussian since σ° is the sea surface RCS with log-normal pdf. For tracking the environment there probably will be periods of minutes between two measurements and the quantities above actually will be averaged over the interval, which may reduce significantly the log-normal measurement noise.

4.3 Tracking Algorithms

4.3.1 Extended Kalman Filter

Since the tracking problem given in (4.1)–(4.2) is nonlinear with non-Gaussian densities, a Kalman filter (KF) cannot be used. Instead, an extended Kalman filter (EKF) [28] is used by locally linearizing the equations using the first terms in the Taylor series expansions of the nonlinear transformations (such as \mathbf{h}) and hoping that the nonlinearities are mild enough that EKF will perform well. Since the pdfs are Gaussian and equations are linearized, it is necessary to propagate only the mean and covariance as in the KF. However, due to this approximation, the EKF cannot claim the optimality enjoyed by the KF for linear-Gaussian systems. The EKF has been implemented successfully in a large number of applications such as radar and sonar target tracking applications and its speed and ease of implementation makes the EKF the filter of choice. Therefore, the EKF is the first filter tested in the RFC tracking problem.

Extended Kalman Filter Equations

For EKF used in this dissertation, the mean and covariance of the underlying Gaussian density is recursively calculated as follows:

$$\hat{\mathbf{x}}_{k|k-1} = \mathbf{F}\hat{\mathbf{x}}_{k-1|k-1} \quad (4.3.13)$$

$$\mathbf{P}_{k|k-1} = \mathbf{Q}_{k-1} + \mathbf{F}\mathbf{P}_{k-1|k-1}\mathbf{F}^T \quad (4.3.14)$$

$$\hat{\mathbf{x}}_{k|k} = \hat{\mathbf{x}}_{k|k-1} + \mathbf{K}_k (\mathbf{y}_k - \mathbf{h}(\hat{\mathbf{x}}_{k|k-1})) \quad (4.3.15)$$

$$\mathbf{P}_{k|k} = \mathbf{P}_{k|k-1} - \mathbf{K}_k \mathbf{S}_k \mathbf{K}_k^T, \quad (4.3.16)$$

where

$$\mathbf{S}_k = \hat{\mathbf{H}}_k \mathbf{P}_{k|k-1} \hat{\mathbf{H}}_k^T + \mathbf{R}_k \quad (4.3.17)$$

$$\mathbf{K}_k = \mathbf{P}_{k|k-1} \hat{\mathbf{H}}_k^T \mathbf{S}_k^{-1} \quad (4.3.18)$$

$$\hat{\mathbf{H}}_k = [\nabla_{\mathbf{x}_k} \mathbf{h}^T(\hat{\mathbf{x}}_{k|k-1})]^T. \quad (4.3.19)$$

4.3.2 Unscented Kalman Filter

To alleviate some of the linearization problems confronting the EKF, the unscented Kalman filter (UKF) [29,30] has been introduced. Unlike the EKF which enforces linearity, this filter approaches the problem from a different perspective by enforcing Gaussianity and keeping the nonlinearity. This still enables the filter to carry all the necessary information by propagating only the mean and covariance as does the KF. It uses an unscented transformation (UT) that enables the propagation of the mean and variance through nonlinear functions. The UKF represents initial densities using only a few predetermined particles called the sigma points. These particles are chosen deterministically by the UT algorithm and they can describe accurately the mean and covariance of a pdf. As the random variable undergoes a nonlinear transformation, these particles are propagated through this nonlinear function and used to reconstruct the new mean and covariance using the UT weights. Hence, unlike the EKF, they can compute accurately the mean and covariance to at least second order (third if the initial density is Gaussian) of the nonlinearity. Although it is fast relative to more advanced techniques, derivative-free, and an improvement over the EKF, there still are two possible weaknesses. The first is that the nonlinearity may be so severe that it may require an even higher order accuracy than the UKF can provide to correctly capture the mean and covariance. The other is that the densities may be highly non-Gaussian so that the first two moments will not be sufficient even if they can be calculated correctly. The UKF used throughout this work is summarized in the next section.

Unscented Kalman Filter Equations

The UKF uses the following recursive formulation where $2n_x + 1$ sigma points $\{\mathcal{X}^i\}_{i=0}^{2n_x}$ and their corresponding weights W^i are generated and used with the unscented transform (UT) to perform the mean ($\hat{\mathbf{x}}_k$) and covariance (\mathbf{P}_k) calculations required in the Kalman framework. The UT weights are given in terms of the scaling parameter $\lambda = \alpha^2(n_x + \kappa) - n_x$ and prior knowledge parameter β

where α is used to control the spread of the sigma points around the mean and κ is the secondary scaling parameter. α , β , and κ are taken as 0.1, 2, and 0, respectively in this paper. UT weights and sigma points are generated using

$$\mathcal{X}_{k-1}^0 = \hat{\mathbf{x}}_{k-1|k-1} \quad (4.3.20)$$

$$\begin{aligned} W_m^0 &= \frac{\lambda}{n_x + \lambda} \\ W_{cov}^0 &= W_m^0 + \beta + 1 - \alpha^2 \\ \mathcal{X}_{k-1}^i &= \hat{\mathbf{x}}_{k-1|k-1} \pm \left(\sqrt{(n_x + \kappa) \mathbf{P}_{k-1|k-1}} \right)_i \\ W_m^i &= W_{cov}^i = \frac{0.5}{n_x + \lambda} \quad i = 1, 2, \dots, 2n_x \end{aligned} \quad (4.3.21)$$

where $(\sqrt{\cdot})_i$ is the i th column of the matrix square root. The prediction step is composed of

$$\mathcal{X}_{k|k-1}^i = \mathbf{F} \mathcal{X}_{k-1}^i, \quad (4.3.22)$$

$$\mathcal{Y}_{k|k-1}^i = \mathbf{h}(\mathcal{X}_{k|k-1}^i) \quad (4.3.23)$$

$$\hat{\mathbf{x}}_{k|k-1} = \sum_{i=0}^{2n_x} W_m^i \mathcal{X}_{k|k-1}^i, \quad (4.3.24)$$

$$\hat{\mathbf{y}}_{k|k-1} = \sum_{i=0}^{2n_x} W_m^i \mathcal{Y}_{k|k-1}^i \quad (4.3.25)$$

$$\mathbf{P}_{k|k-1} = \mathbf{Q}_{k-1} + \sum_{i=0}^{2n_x} W_{cov}^i [\mathcal{X}_{k|k-1}^i - \hat{\mathbf{x}}_{k|k-1}] [\mathcal{X}_{k|k-1}^i - \hat{\mathbf{x}}_{k|k-1}]^T \quad (4.3.26)$$

and the update step uses

$$\begin{aligned} \mathbf{P}_{xy} &= \sum_{i=0}^{2n_x} W_{cov}^i [\mathcal{X}_{k|k-1}^i - \hat{\mathbf{x}}_{k|k-1}] [\mathcal{Y}_{k|k-1}^i - \hat{\mathbf{y}}_{k|k-1}]^T \\ \mathbf{P}_{yy} &= \sum_{i=0}^{2n_x} W_{cov}^i [\mathcal{Y}_{k|k-1}^i - \hat{\mathbf{y}}_{k|k-1}] [\mathcal{Y}_{k|k-1}^i - \hat{\mathbf{y}}_{k|k-1}]^T \\ \mathbf{K}_k &= \mathbf{P}_{xy} (\mathbf{P}_{yy} + \mathbf{R}_k)^{-1} \end{aligned} \quad (4.3.27)$$

$$\hat{\mathbf{x}}_{k|k} = \hat{\mathbf{x}}_{k|k-1} + \mathbf{K}_k (\mathbf{y}_k - \hat{\mathbf{y}}_{k|k-1}) \quad (4.3.28)$$

$$\mathbf{P}_{k|k} = \mathbf{P}_{k|k-1} - \mathbf{K}_k (\mathbf{P}_{yy} + \mathbf{R}_k) \mathbf{K}_k^T. \quad (4.3.29)$$

4.3.3 Particle Filter

The last algorithm used in this paper is the Sequential Monte Carlo (SMC) or the particle filter (PF). This filter does not come with any inherent assumptions and is used for many nonlinear, non-Gaussian tracking problems [31]. The main difference with Kalman type filters is that, since no Gaussian assumption is made, propagating the mean and covariance is not sufficient. Instead the PF propagates an ensemble of particles to represent the densities. These particles are selected randomly by MC runs. Compared with the sigma points of the UKF, a much larger number of particles are needed to represent the pdf. Therefore, the PF can perform much better than its KF variants but it does this with an order of magnitude increase in the computational burden. There are many different variants of the PF such as the regularized particle filter (RPF), Markov chain Monte Carlo step particle filter (MCMC-PF), auxiliary (ASIR) and classical sequential importance resampling (SIR) particle filter [32].

The SIR algorithm is used throughout this work. Normally, degeneracy can be a problem for the SIR algorithm, especially for low process noise systems. However, due the environmental uncertainty in the model (Section 4.2.2), \mathbf{Q}_k is selected relatively large, thus mostly eliminating the need for more complex particle filters with improved sample diversity. The SIR algorithm [33] is summarized in the next section.

Sequential Importance Resampling Filter Equations

The SIR algorithm uses N particles $\{\mathcal{X}^i\}_{i=1}^N$ to represent the pdf at each step k . The filter has the predict and update sections just as in a KF but the SIR filter will use these sections to propagate the particles instead of mean and covariance calculations.

The initial set of particles $\{\mathcal{X}_o^i\}_{i=1}^N$ are sampled from the prior $p(\mathbf{x}_o)$. The SIR filter uses the importance sampling density as the transitional prior $p(\mathbf{x}_k|\mathbf{x}_{k-1})$. Therefore, the prediction step consists of sampling from this pdf. Then the normal-

ized weight W_k^i of each particle is calculated from its likelihood function evaluation. The update step includes the resampling section where a new set of N particles is generated from the parent set according to the weights of the parent particles. Hence, a single iteration of the recursive SIR algorithm can be summarized as:

$$\{\mathcal{X}_{k|k-1}^i\}_{i=1}^N \sim p(\mathbf{x}_k|\mathbf{x}_{k-1}) \quad (4.3.30)$$

$$W_k^i = \frac{p(\mathbf{y}_k|\mathcal{X}_{k|k-1}^i)}{\sum_{i=1}^N p(\mathbf{y}_k|\mathcal{X}_{k|k-1}^i)} \quad (4.3.31)$$

$$\begin{aligned} \{\mathcal{X}_{k|k}^i\}_{i=1}^N &= \text{Resample} \left[W_k^i, \{\mathcal{X}_{k|k-1}^i\}_{i=1}^N \right] \\ s.t. \quad \Pr \left\{ \mathcal{X}_{k|k}^i = \mathcal{X}_{k|k-1}^j \right\} &= W_k^j \end{aligned} \quad (4.3.32)$$

4.3.4 Posterior Cramér-Rao Lower Bound

It usually is not possible to have an optimal estimator with minimum mean square error (MMSE) for the nonlinear filtering problems such as RFC. All the techniques used in this paper also are sub-optimal techniques. Therefore, it is desirable to have a tool that not only can assess the performances of these sub-optimal techniques but also provide a limit to achievable performance for a given environment.

In a classical non-Bayesian framework, the Cramér-Rao Lower Bound (CRLB), which is the inverse of the Fisher information matrix (FIM), is commonly used. In a Bayesian framework this instead can be replaced by the posterior Cramér-Rao Lower Bound (PCRLB) introduced by van Trees [34]. Since this paper exclusively works with PCRLB, it will henceforth be referred to simply as CRLB.

Any filter that achieves a mean square error (MSE) equal to the CRLB is called an efficient estimator. For a linear and Gaussian system, the Kalman filter is an efficient estimator. It may not be possible to attain the CRLB for a nonlinear, non-Gaussian system.

Let \mathbf{J}_k be the inverse of the CRLB_k as a $(n_x \times n_x)$ filtering information matrix so that the MSE of any filter estimate at tracking step index k will be bounded as

$$\mathbb{E} \left\{ (\hat{\mathbf{x}}_{k|k} - \mathbf{x}_k) (\hat{\mathbf{x}}_{k|k} - \mathbf{x}_k)^T \right\} \geq \mathbf{J}_k^{-1}, \quad (4.3.33)$$

where $\hat{\mathbf{x}}_{k|k}$ is the estimate of \mathbf{x}_k given its previous history $\{\mathbf{x}_0, \mathbf{x}_1, \dots, \mathbf{x}_{k-1}\}$ and the set of measurements $\{\mathbf{y}_1, \mathbf{y}_2, \dots, \mathbf{y}_k\}$. A computationally efficient way of computing this CRLB recursively for discrete-time nonlinear filtering problems is [35]:

$$\mathbf{J}_k = \mathbf{D}_{k-1}^{22} - [\mathbf{D}_{k-1}^{12}]^T (\mathbf{J}_{k-1} + \mathbf{D}_{k-1}^{11})^{-1} \mathbf{D}_{k-1}^{12} \quad (4.3.34)$$

where

$$\mathbf{D}_{k-1}^{11} = -\mathbb{E} \left\{ \nabla_{\mathbf{x}_{k-1}} [\nabla_{\mathbf{x}_{k-1}} \log p(\mathbf{x}_k | \mathbf{x}_{k-1})]^T \right\} \quad (4.3.35)$$

$$\mathbf{D}_{k-1}^{12} = -\mathbb{E} \left\{ \nabla_{\mathbf{x}_k} [\nabla_{\mathbf{x}_{k-1}} \log p(\mathbf{x}_k | \mathbf{x}_{k-1})]^T \right\} \quad (4.3.36)$$

$$\begin{aligned} \mathbf{D}_{k-1}^{22} = & -\mathbb{E} \left\{ \nabla_{\mathbf{x}_k} [\nabla_{\mathbf{x}_k} \log p(\mathbf{x}_k | \mathbf{x}_{k-1})]^T \right\} \\ & - \mathbb{E} \left\{ \nabla_{\mathbf{x}_k} [\nabla_{\mathbf{x}_k} \log p(\mathbf{y}_k | \mathbf{x}_k)]^T \right\}. \end{aligned} \quad (4.3.37)$$

Note that the computations only require $(n_x \times n_x)$ matrices and the computation cost is independent of the step index k .

The RFC tracking problem with the system of equations defined in (4.1) – (4.2) has a linear state equation and both of the random noise sequences \mathbf{v} and \mathbf{w} are additive and Gaussian. Therefore, the above equations can be reduced to

$$\begin{aligned} \mathbf{D}_{k-1}^{11} &= \mathbf{F}^T \mathbf{Q}_{k-1}^{-1} \mathbf{F} \\ \mathbf{D}_{k-1}^{12} &= -\mathbf{F}^T \mathbf{Q}_{k-1}^{-1} \\ \mathbf{D}_{k-1}^{22} &= \mathbf{Q}_{k-1}^{-1} + \mathbb{E} \left\{ \mathbf{H}_k^T \mathbf{R}_k^{-1} \mathbf{H}_k \right\}, \end{aligned} \quad (4.3.38)$$

where

$$\mathbf{H}_k = [\nabla_{\mathbf{x}_k} \mathbf{h}^T(\mathbf{x}_k)]^T \quad (4.3.39)$$

is the Jacobian of $\mathbf{h}(\mathbf{x})$ evaluated at its true value \mathbf{x}_k . Unfortunately the expectation in (4.3.38) has to be evaluated numerically. The recursion in (4.3.34) is initiated by using the prior probability $p(\mathbf{x}_o)$ to compute \mathbf{J}_o as

$$\mathbf{J}_o = -\mathbf{E} \left\{ \nabla_{\mathbf{x}_o} [\nabla_{\mathbf{x}_o} \log p(\mathbf{x}_o)]^T \right\} = \mathbf{P}_o^{-1}, \quad (4.3.40)$$

where \mathbf{P}_o is the covariance of the prior density, assuming it is Gaussian.

4.4 Examples

This section is composed of three examples covering tracking of both the evaporative and surface-based ducts. Throughout the examples, issues such as the performance limitations, filter efficiencies, divergence characteristics, and CPU time comparisons are addressed. These three case studies are:

1. Temporal tracking of a fixed path, range-independent surface-based duct (SBD) for performance comparison of the EKF, UKF, and PF with respect to the CRLB.
2. Divergence analysis of the EKF, UKF and PF for a typical temporal range-independent SBD tracking problem.
3. Temporal tracking of a range-dependent littoral evaporation duct. Comparison with the SBD tracking.

4.4.1 Case Study I: Temporal Tracking of a Range-Independent Surface-Based Duct

This example is used to compare the tracking performances of the EKF, UKF and PF and compute their efficiencies using the numerically computed CRLB. The range-independent SBD is selected from the environmental library of the Advanced Refractive Effect Prediction System (AREPS) [36]. The Bahrain radiosonde station in the Persian Gulf is used for the simulation (Fig. 4.2). The

Table 4.1: Case Study I: Comparison of Tracking Algorithms and CRLB Radiosonde Station Bahrain, Persian Gulf

| Station | | Environment | |
|-------------------------|----------|--|---------------------|
| Longitude | 50°36'E | Duct Type | Surface-based Duct |
| Latitude | 26°18'N | Month | Mar/Apr/May Average |
| Elevation | 2 m | Time | Day/Night Average |
| Marsden Square | 103 | Occurrence | 59% Day / 75% Night |
| Radar | | c_1 | 0.050 M-units/m |
| Frequency | 2.84 GHz | c_2 | -0.221 M-units/m |
| Height | 15 m | h_1 | 43 m |
| Range Bin | 600 m | h_2 | 77 m |
| Simulation Parameters | | | |
| Monte Carlo Runs | | 100 | |
| Track Length, k_{max} | | 30 min – 1 measurement/min | |
| Initial Covariance | | $\mathbf{P}_o = \text{diag}\{(10 \text{ M-units/km})^2, (3 \text{ m})^2\}$ | |
| State Noise Covariance | | $\mathbf{Q}_k = \text{diag}\{(3 \text{ M-units/km})^2, (1 \text{ m})^2\}$ | |
| Measurement Noise | | $\mathbf{R}_k = \text{diag}\{(5 \text{ dB})^2\}$, log-normal RCS | |

station, average environment, radar and simulation parameters are given in Table 4.1. The state vector \mathbf{x} has four parameters representing the layer thicknesses and slopes of the range-independent SBD M-profile as defined in Section 4.2.1. The layer slopes are given in M-units/m while the RMS errors and standard deviations in the slope estimates are given in M-units/km. The fact that the SBD (excluding evaporative and elevated ducts) is present 67% of the time makes the estimation and tracking of these atmospheric ducts a high priority in the Persian Gulf. The same frequency as that of the Space Range Radar (SPANDAR) [7, 25] is used. The height is set to 15 m, a typical value for a naval radar. New clutter data is provided every minute ($\Delta k=1$ min.) and an overall track length of 30 min. is used. The log-normal sea clutter is assumed to have a standard deviation of 5 dB [19]. The values of \mathbf{Q}_k , \mathbf{P}_o , \mathbf{R}_k are selected in accordance with the values obtained in Section 4.2.2.

The CRLB and the filter performances are calculated using Monte Carlo analysis. First, 100 environmental parameter trajectories are created from the state equation (4.1) with starting values randomly selected from the prior density. Then, \mathbf{D}_{k-1}^{22} in (4.3.38) is calculated using

$$\mathbf{D}_{k-1}^{22} = \mathbf{Q}_{k-1}^{-1} + \frac{1}{N_{MC}} \sum_{j=1}^{N_{MC}} \nabla \mathbf{h}(\mathbf{x}_k^j) \mathbf{R}_k^{-1} [\nabla \mathbf{h}(\mathbf{x}_k^j)]^T. \quad (4.4.41)$$

Each of these 100 environmental trajectories also is tracked using the EKF, UKF and PF. The results are given in Fig. 4.2 and Table 4.2. The performance metrics are:

$$\eta_k(i) = \mathbf{J}_k^{-1/2}(i, i) / \text{RMS}_k(i) \quad (4.4.42)$$

$$\text{RTAMS}(i) = \left[\sum_{k=k_1}^{k_2} \sum_{j=1}^{N_{MC}} \frac{(\hat{\mathbf{x}}_k^j(i) - \mathbf{x}_k^j(i))^2}{(k_2 - k_1 + 1)N_{MC}} \right]^{1/2} \quad (4.4.43)$$

$$\text{Improv.} = \frac{\text{RTAMS}_{EKF} - \text{RTAMS}_{filter}}{\text{RTAMS}_{EKF}} \quad (4.4.44)$$

where $\mathbf{x}_k^j(i)$ is the i th parameter of the true state vector \mathbf{x} at time index k for the j th MC run, RMS_k and η_k are the root mean square error and the filter efficiency at step k , RTAMS is the root time averaged mean square error [32] calculated for the interval $[k_1, k_2]$, and (4.4.44) is used to calculate the performance improvement of a filter with respect to the EKF. RTAMS is calculated for the 5-30 min. interval so that the initial variation will not affect the performance calculations.

The results in Fig. 4.2 show that Kalman filters suffer due to their inherent approximations. The measurement equation is highly nonlinear for most of the state space and linearization (EKF) clearly does not work. Since the UKF does not assume linearity, it enjoys an average of 36% improvement over the EKF results. However, a pure Gaussian assumption and high nonlinearity also results in poor UKF estimates with only 12% efficiency. All the particle filters used in this case perform better than both of the Kalman filters. The PF with 5000 particles has an average error of only 1.6%, very close to the value of 1.4% predicted by the CRLB. It is 77% efficient and enjoys a 84% improvement over the EKF. Note that PF

Table 4.2: Performance Comparison for Case Study I

| Method | RMS Error After 30 min. | | | | | | RTAMS | | | | Average % |
|----------------------|-------------------------|-------|-------|-------|------------|------------|--------------|-------|-------|-------|-------------|
| | c_1 | c_2 | h_1 | h_2 | Avg. Error | Average | c_1 | c_2 | h_1 | h_2 | Improvement |
| | (M-units/km) | | (m) | | (%) | η (%) | (M-units/km) | | (m) | | Over EKF |
| EKF | 12.7 | 20.5 | 3.36 | 11.01 | 14.2 | 8 | 11.7 | 18.8 | 3.03 | 9.48 | - |
| UKF | 8.5 | 16.0 | 2.33 | 7.64 | 9.9 | 12 | 6.5 | 11.9 | 1.87 | 6.98 | 36 |
| PF-200 | 5.5 | 2.6 | 0.71 | 3.72 | 4.7 | 30 | 4.9 | 2.7 | 0.73 | 3.50 | 71 |
| PF-1000 | 3.1 | 1.9 | 0.38 | 0.97 | 2.3 | 58 | 3.6 | 2.2 | 0.59 | 1.96 | 79 |
| PF-5000 | 2.0 | 1.7 | 0.23 | 0.96 | 1.6 | 77 | 2.9 | 2.2 | 0.46 | 1.20 | 84 |
| $\sqrt{\text{CRLB}}$ | 2.0 | 1.0 | 0.21 | 0.57 | 1.4 | 100 | 2.1 | 1.0 | 0.24 | 0.67 | 90 |

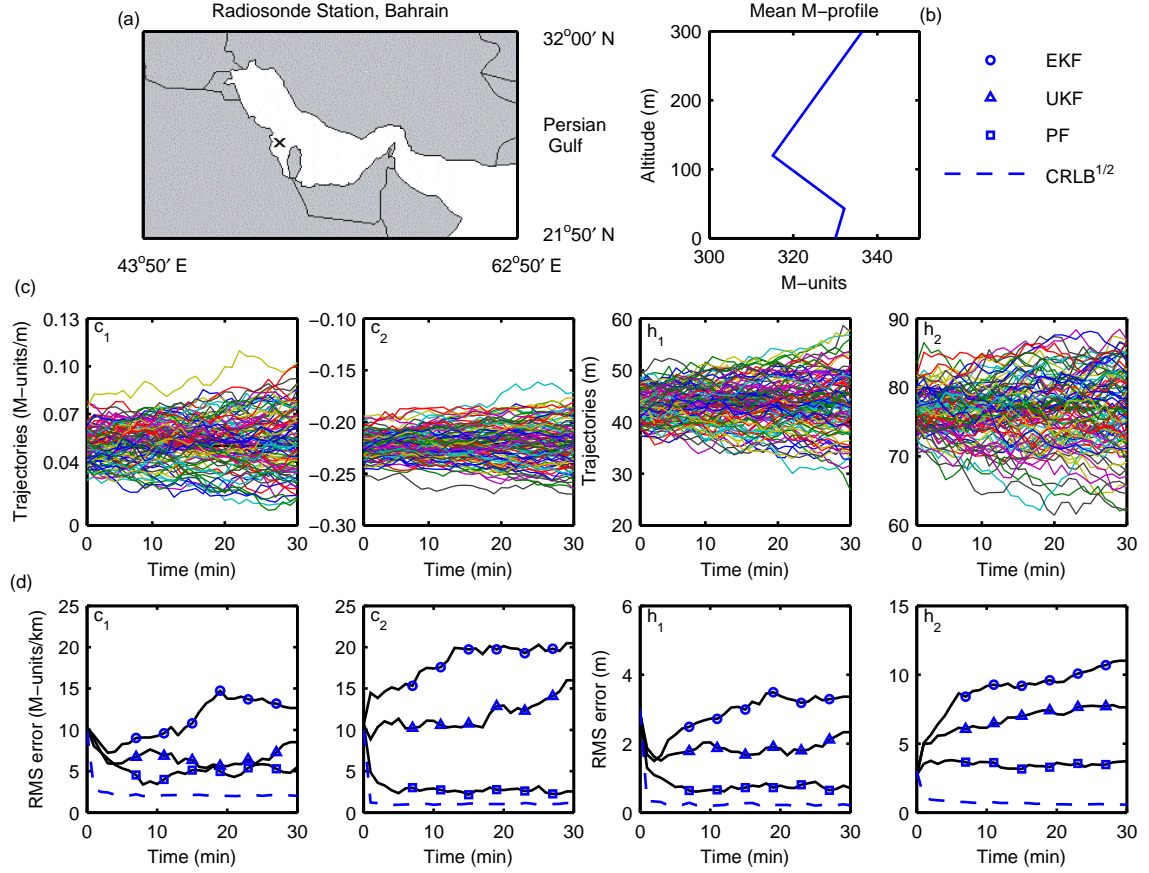


Figure 4.2: Case study I for comparison of the tracking algorithms. (a) Regional map and the location of the station (\times), (b) average spring M-profile, (c) evolutions of 100 Monte Carlo trajectories, and (d) RMS errors of the EKF (O), UKF (Δ), and 200-particle PF (\square) obtained from the tracking performance of these trajectories along with the square root of the posterior CRLB (dashed).

requires an order of magnitude more of CPU time. The PF-200 required a factor of 10 more CPU time than that of the UKF for this scenario. Hence, the PF is a costly alternative and as a general rule should be avoided as long as the Kalman framework provides reasonable tracking. However, atmospheric parameters sometimes can fluctuate abruptly. This requires increasing \mathbf{Q}_k to compensate for the sudden jumps. Initial tests showed that the Kalman structures are much more sensitive to these sudden moves and diverge if the sudden jump is large enough, even after \mathbf{Q}_k is increased, whereas particle filters showed more robust tracking

performance. Therefore, it can be concluded that the SBD tracking requires a particle filter approach even though they are computationally expensive.

Although the results in Table 4.2 show the most frequently encountered scenario in the SBD tracking, the simulations show that there are three different cases depending on where you are in the state space. The other two are when the PF and the UKF works but not the EKF and when all three filters perform well. However, these are relatively rare cases and occur only when the nonlinearity is not strong.

An important issue with the particle filters is the selection of the number of particles N_p to be used at each step. The increase in the efficiency of the PF with increasing N_p is given in Fig. 4.3 for this case study. Unfortunately it is hard to determine an optimum value since this curve is scenario dependent. A tropospheric propagation code such as the Terrain Parabolic Equation Model (TPEM) [26] can simulate typically 20 environments per second on a 3 GHz computer. Therefore, for a filter with a 1 min. update rate, $N_p < 20 \times 60 = 1200$ can be selected, which corresponds to an average 2% error in the tracked parameters for this scenario. An alternative to this is assuming a discrete state space instead of the continuous one used in this work. Hence, only a finite number of possible environment states needs to be pre-computed so that a larger number of particles can be used. Due to its discrete nature, the problem now can be solved using the grid-based methods such as a Hidden Markov Model (HMM) based tracking filter which employs a Viterbi algorithm. RFC estimation for a fixed path based on the Viterbi algorithm has been proposed in [12]. However, this requires a sufficiently dense gridding of the state space, which very quickly will grow as the state dimension increases.

4.4.2 Case Study II: Divergence in Surface-Based Duct Tracking

This example studies the divergence problem in SBD tracking. The height and slope values (Fig. 4.4) and their variations are selected very similar to the helicopter measured real M-profiles obtained in the Wallops'98 experiment [7] (Section

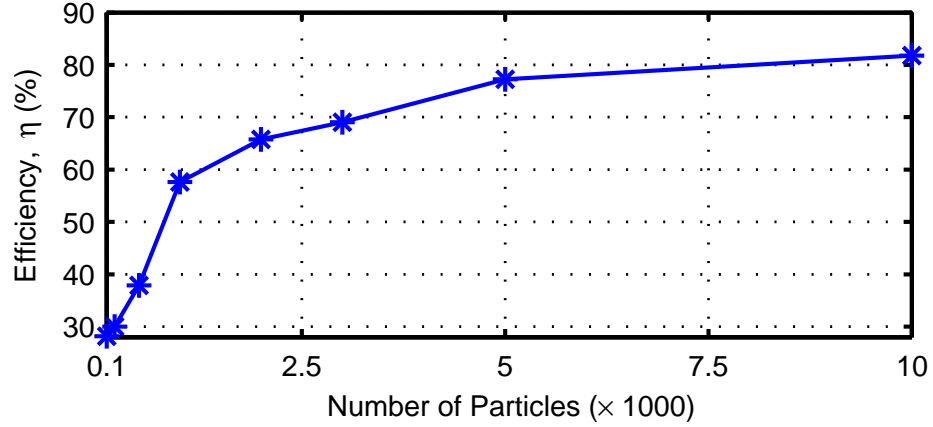


Figure 4.3: Efficiency of the PF as a function of the number of particles.

4.2.2). All the radar and simulation parameters are kept the same as Case Study I except \mathbf{Q}_k for the layer slopes and \mathbf{R}_k are taken as $(10 \text{ M-units/km})^2$ and $(4 \text{ dB})^2$, respectively. This trajectory is tracked 100 times by each filter to obtain divergent track probabilities.

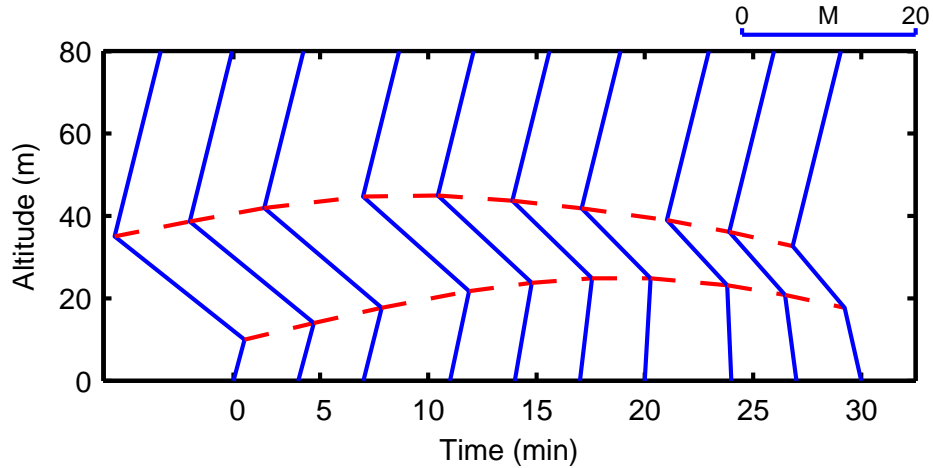


Figure 4.4: Case Study II: Temporal evolution of the range-independent duct.

The evolution of the clutter signal without the addition of noise is given in Fig. 4.5. This strong nonlinearity of $\mathbf{h}(\mathbf{x}_k)$ results in a high percentage of track divergence for the Kalman filters. For this scenario, a track is declared as divergent if any of the slope estimates for c_1 or c_2 have a RMS error greater than 50 M-units/km or any of the layer thickness estimates for h_1 or h_2 have a RMS

error larger than 5 m for any 5 consecutive minutes. A typical track result is given in Fig. 4.6 for each filter type. The divergence statistics of the filters are provided in Table 4.3. Similar to Case Study I, the PF performs significantly better than both the Kalman filters and the UKF is better than the EKF. Both Kalman filters mostly were able to follow the thickness variations but failed in tracking the slopes which usually have more effect on the clutter return. Interestingly, the EKF RTAMS error for the layer thickness is less than that of the UKF. However, this is more than offset by the fact that after only 10 min, the EKF reached a 47% divergence rate while none of the UKF runs diverged. The PF-200 starts to diverge after 30 min. with a 17% rate and only 2% of the PF-1000 runs failed to track the duct after 30 min.

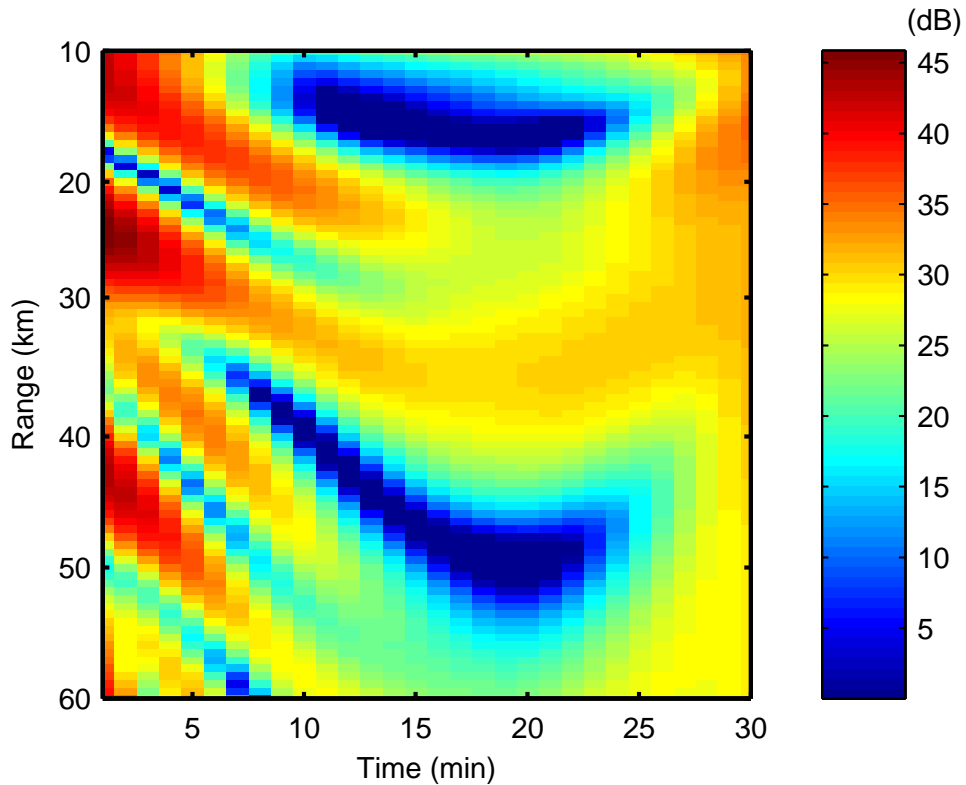


Figure 4.5: Evolution of the highly nonlinear relative radar clutter \mathbf{y}_k (dB) computed for the true environment without \mathbf{w}_k .

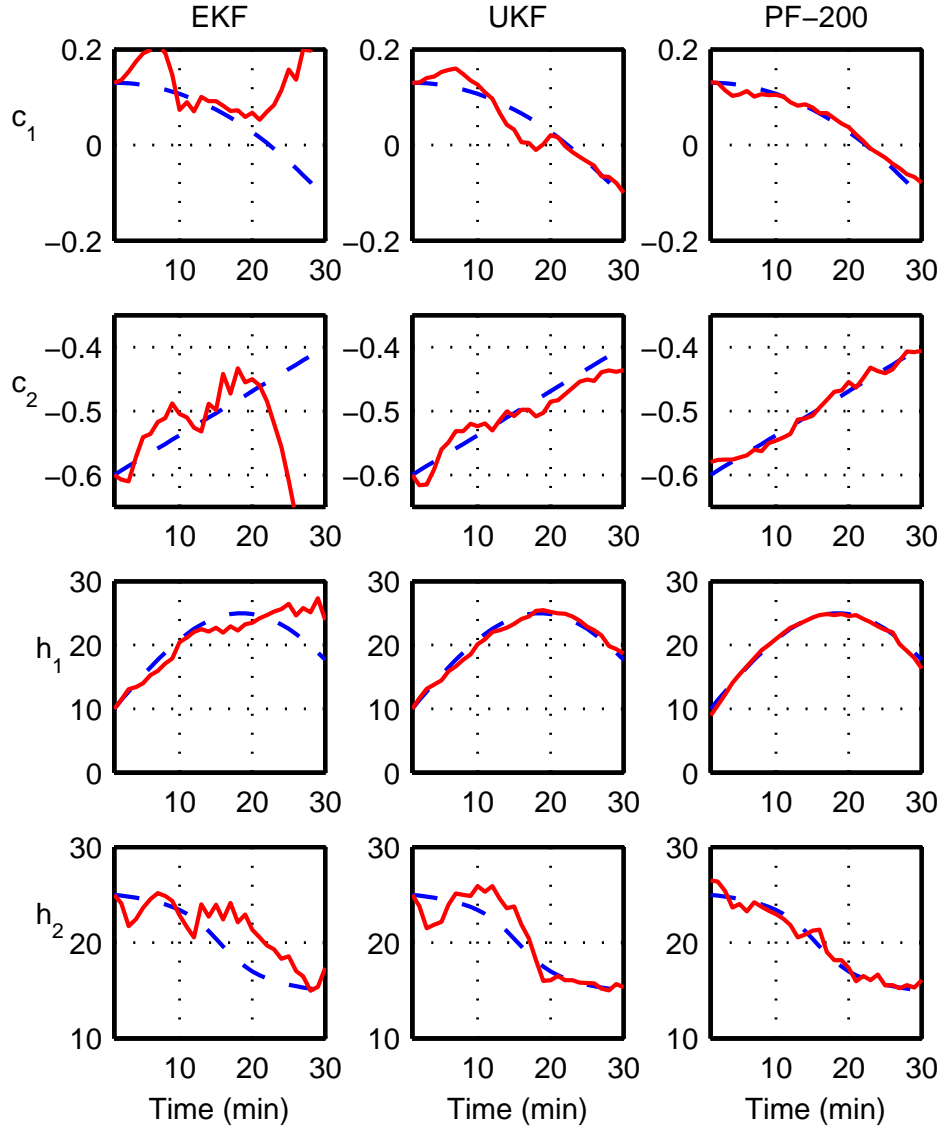


Figure 4.6: Case Study II: Temporal tracking of the range-independent SBD. c_1 and c_2 are in M-units/m and h_1 and h_2 are in meters. True trajectories (dashed) and filter estimates (solid) for the EKF, UKF and PF-200.

4.4.3 Case Study III: Range-Dependent Evaporation Duct Tracking in Coastal Regions

This example is used to compare the tracking performances of the three filters in an evaporation duct environment. Evaporation duct differs significantly from the SBD in terms of the nonlinearity of the measurement equation (4.2). The

Table 4.3: Performance Comparison for Case Study II

| Method | Average RTAMS | | Divergent Track Percentage After | | |
|----------------|---------------|-----|----------------------------------|---------|---------|
| | M-units/km | m | 10 min. | 20 min. | 30 min. |
| EKF | 84.2 | 2.9 | 47 | 69 | 90 |
| UKF | 41.8 | 3.3 | 0 | 29 | 37 |
| PF-200 | 27.7 | 0.9 | 0 | 0 | 17 |
| PF-1000 | 16.2 | 0.5 | 0 | 0 | 2 |

clutter in an evaporation duct environment does not have the complex patterns of the SBD-induced clutter such as the one in Fig. 4.5. Except for the very thick ducts which rarely occur, the evaporative duct clutter decreases monotonically with range and the nonlinearities are very mild [6]. This means that the Kalman filters will no longer suffer from the nonlinearities which severely limited their usage in the previous SBD tracking examples.

Eastern Mediterranean is selected for this example. Day time statistics of July are used. A summary of the selected region, environmental conditions, radar and simulation parameters are given in Table 4.4. The naval radar is taken to be located at 25km, looking towards the shore. It should be noted that evaporation ducts thicker than 10 m exist more than 80% of the time in this region. The regional statistics of the evaporation duct height (EDH) is given in Fig. 4.7(a) together with the pdf for the air-sea temperature difference given in Fig. 4.7(b). The small temperature difference makes possible the representation of the vertical evaporative M-profile using only the EDH as given in Section 4.2.1.

A complex, temporally evolving, range-dependent coastal evaporation duct as given in Fig. 4.7(c) is created. Corresponding 2-D M-profiles at $t = 0$, 60, and 120 min. are shown in Fig. 4.7(d). As a typical coastal duct, it has high variability near the coastal zones with multiple local disturbances with 10-30 min. and 2-5 km scales similar to those encountered in [24, 37–39], while it gets more uniform as the distance from the shore increases. It also includes the formation and dissipation of a strong offshore evaporative duct (between 60-100 min.) and

as usual, the duct starts to lose its strength as it gets closer to the land. To better represent the coastal zones, a denser grid is used for these regions. The nonuniform grid used here has 7 ranges at 1, 3, 5, 7, 10, 13, and 17 km from the shore. Hence, the state vector is composed of the EDH at these 7 ranges.

The tracking performance of the EKF, UKF, PF-200, and PF-1000 are given in Table 4.5. A typical EKF track is provided in Fig. 4.7(e). Both Kalman filters have a high performance with an average RTAMS of around 1 m. Since the nonlinearity is not severe, the 1st order accurate linearization used by the EKF is as good as the higher order accurate UKF and overall, the UKF achieves only 1% improvement over the EKF. Unlike the SBD tracking, the 200 point PF is no match for the Kalman filters, while PF-1000 is now comparable to the EKF and the UKF.

These above results show that Kalman filters are able to track evaporative ducts successfully, and can only be outperformed by a very high N_p PF which is computationally much more expensive.

4.5 Discussion

A fundamental question for a real RFC tracking system is the temporal/spatial step size. The continuous real-time inflow of clutter data enables RFC techniques to capture much finer details in the local environmental conditions. Track updates at every minute or two seems to be a reasonable choice for tracking since the typical RMS error in the propagation factor has been shown to exceed 6 dB after 30 min. due to temporal decorrelation of the environmental parameters [40]. Tracking faster may necessitate a decrease in the number of particles to be used in the PF which may degrade the track effectiveness.

During the simulations some special cases other than the provided examples have been noted which can cause track divergence. One of these is when one of the layer thickness parameters gets very small for a short period of time.

Table 4.4: Case Study III: Coastal Range-Dependent Evaporation Duct Tracking, Eastern Mediterranean

| Region | | Radar | |
|---|-----------|---|-------|
| Longitude | 20°E–30°E | Frequency | 5 GHz |
| Latitude | 30°N–40°N | Height | 15 m |
| Marsden Square | 142 | Range Bin | 100 m |
| Environment | | | |
| Duct Type | | Range-Dependent Evaporation Duct | |
| Month/Time | | July/Day Time Average | |
| Mean Duct Height | | 16.4 m | |
| % Time EDH>10 m | | 81.7% | |
| % Time Air-Sea $\triangle T < 1^{\circ}C$ | | 87.2% | |
| Simulation Parameters | | | |
| Track Length, k_{max} | | 120 min – 1 measurement/2 min | |
| Initial Covariance | | $\mathbf{P}_o = \text{diag}\{(3 \text{ m})^2\}$ | |
| State Noise Covariance | | $\mathbf{Q}_k = \text{diag}\{(0.707 \text{ m})^2\}$ | |
| Measurement Noise | | $\mathbf{R}_k = \text{diag}\{(3 \text{ dB})^2\}$, log-normal RCS | |

Table 4.5: Performance Comparison for Case Study III

| Method | Average RMS Error | | Average RTAMS (m) | Avg. % Improv. Over EKF |
|----------------|-------------------|-----------|----------------------|----------------------------|
| | 1 hr. (m) | 2 hr. (m) | | |
| EKF | 1.17 | 0.88 | 1.08 | - |
| UKF | 1.17 | 0.90 | 1.07 | 1 |
| PF–200 | 1.19 | 1.93 | 1.38 | -29 |
| PF–1000 | 1.13 | 1.42 | 1.13 | -6 |

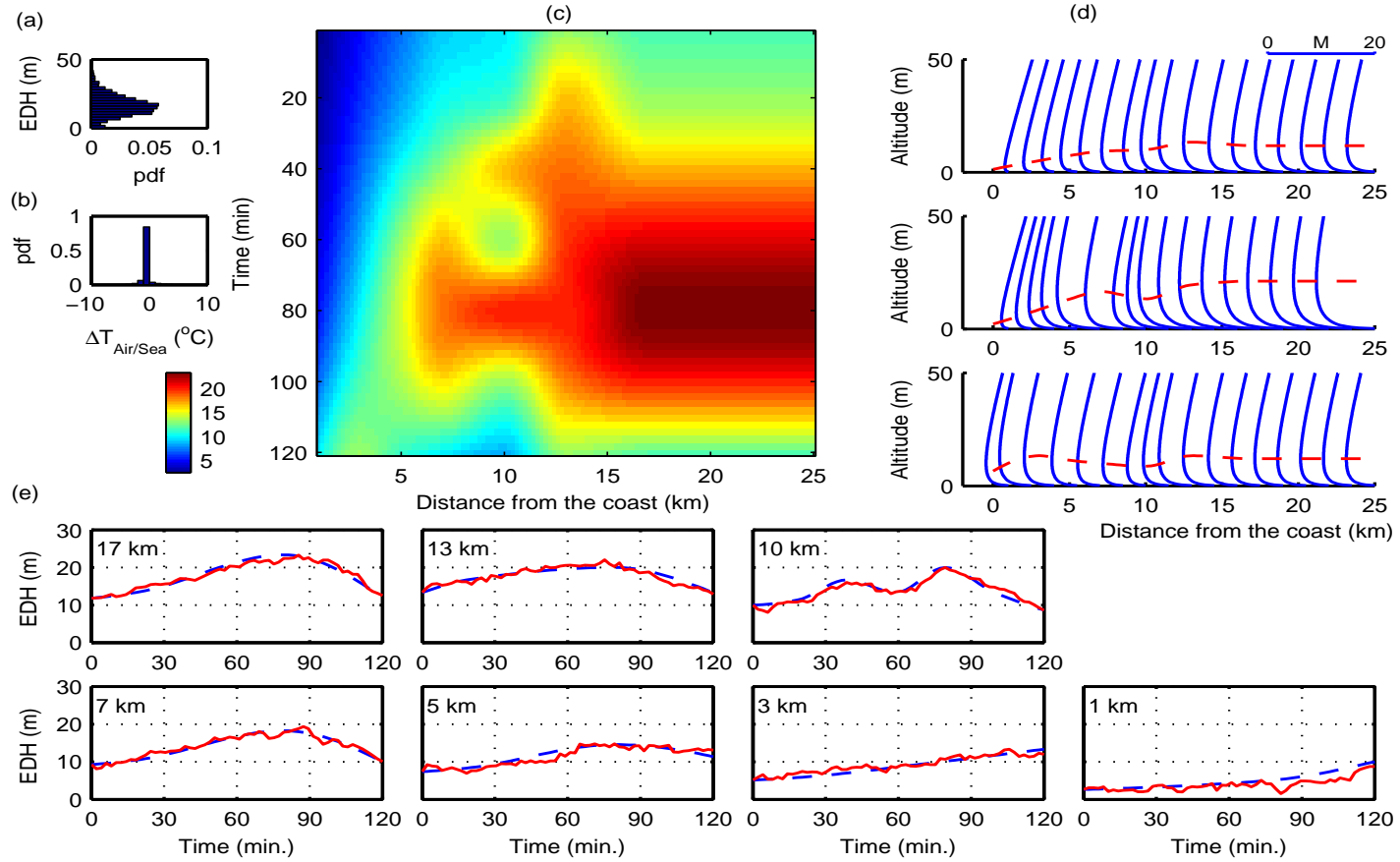


Figure 4.7: Case Study III: Range-Dependent Evaporation Duct Tracking. (a) Evaporation duct height (EDH) statistics and (b) air-sea temperature difference statistics for the given region/month/time, (c) spatio-temporal evolution of the simulated EDH, (d) 2-D M-profiles at 0, 60, and 120 min., and (e) the evolution of EDH for the selected range grid that is used to construct the state vector \mathbf{x}_k (dashed line as the true value, solid line as the EKF track).

Since the layer is thin it has minimal effect on electromagnetic propagation so the slope of this layer does not have any significance on the overall clutter structure. This leads to major deviations in the slope parameter and when the layer starts to thicken again, the track diverges since the starting slope value is too far from the true one. The PF is more resilient to this type of divergence than the Kalman filters.

The second case is when the overall duct height becomes less than the antenna height for some range interval (in a range-dependent profile) or for a short duration. Since the source now is outside the waveguide, the sea clutter drops possibly resulting in track divergence.

The final case is when the duct becomes very strong for some range interval (in a range-dependent profile) or for a short duration. A strong duct is formed when the inversion slope is so strong (highly negative) that the entire electromagnetic field is trapped before it reaches the upper boundary of the inversion layer. Then any inversion layer thickness value larger than this total entrapment thickness will have the same effect on the clutter, resulting in large deviations in the inversion layer thickness and as the duct loses its strength, divergence occurs since the starting value of the inversion layer thickness is too far from its true value.

4.6 Conclusion

The extended and unscented Kalman and particle filters have been studied for tracking the spatial and temporal evolution of the lower atmospheric index of refraction using the radar clutter return. The divergence statistics, computational complexities, and tracking performances of these filters were compared to each other using the posterior Cramér-Rao lower bound through various case studies. The results showed that the clutter can be a rich source of information for real-time tracking of the 3-D environment in which the radar is operating. The Kalman filters showed that they can be used successfully for various RFC tracking

cases such as evaporative duct tracking but were limited by the nonlinearity of the mapping from environmental refractivity to clutter (that uses the split step fast Fourier transform parabolic equation) and the non-Gaussianity of the environmental parameter densities, especially for the surface-based duct tracking. In contrast, the particle filter showed that it can successfully track a wide range of scenarios although it required much larger computation times relative to the Kalman filters.

4.7 Acknowledgment

The authors would like to thank Ted Rogers, SPAWAR, San Diego, CA, for providing the Wallops'98 clutter maps and providing insight on COAMPS and atmospheric modeling and John Hopkins University, Applied Physics Laboratory, Baltimore, MD, for providing the helicopter refractivity measurements.

The text of Chapter Four is in part and under some rearrangements a reprint of the material as it appears in Caglar Yardim, Peter Gerstoft, and William S. Hodgkiss, "Tracking refractivity from radar clutter," *IEEE Trans. on Antennas and Propagation*, submitted 2007. The dissertation author was the primary researcher and author, and the co-authors listed in this publication directed and supervised the research which forms the basis for this chapter.

Bibliography

- [1] J. R. Rowland and S. M. Babin. Fine-scale measurements of microwave profiles with helicopter and low cost rocket probes. *Johns Hopkins APL Tech. Dig.*, 8 (4):413–417, 1987.
- [2] E. R. Thews. Timely prediction of low-altitude radar performance in operational environments using *in situ* atmospheric refractivity data. *IEEE Proc.*, 137 (F-2):89–94, 1990.
- [3] Richard M. Hodur. The naval research laboratory’s coupled ocean/atmosphere mesoscale prediction system (COAMPS). *Monthly Weather Review*, 125(7):1414–1430, 1996.
- [4] Adam Willitsford and C. R. Philbrick. Lidar description of the evaporative duct in ocean environments. volume 5885. Proceedings of SPIE, Bellingham, WA, September 2005.
- [5] Anthony R. Lowry, Chris Rocken, Sergey V. Sokolovskiy, and Kenneth D. Anderson. Vertical profiling of atmospheric refractivity from ground-based GPS. *Radio Science*, 37(3):1041–1059, 2002. doi:10.1029/2000RS002565.
- [6] L. Ted Rogers, C. P. Hattan, and J. K. Stapleton. Estimating evaporation duct heights from radar sea echo. *Radio Science*, 35 (4):955–966, 2000. doi:10.1029/1999RS002275.
- [7] Peter Gerstoft, L. T. Rogers, J. Krolik, and W. S. Hodgkiss. Inversion for refractivity parameters from radar sea clutter. *Radio Science*, 38 (3):1–22, 2003. doi:10.1029/2002RS002640.
- [8] Peter Gerstoft, W. S. Hodgkiss, L. T. Rogers, and M. Jablecki. Probability distribution of low altitude propagation loss from radar sea-clutter data. *Radio Science*, 39:1–9, 2004. doi:10.1029/2004RS003077.
- [9] Amalia Barrios. Estimation of surface-based duct parameters from surface clutter using a ray trace approach. *Radio Science*, 39 RS6013:1–15, 2004. doi:10.1029/2003RS002930.

- [10] L. Ted Rogers, Michael Jablecki, and Peter Gerstoft. Posterior distributions of a statistic of propagation loss inferred from radar sea clutter. *Radio Science*, 40 (6):1–14, 2005. doi:10.1029/2004RS003112.
- [11] Caglar Yardim, Peter Gerstoft, and William S. Hodgkiss. Estimation of radio refractivity from radar clutter using Bayesian Monte Carlo analysis. *IEEE Trans. Antennas Propagat.*, 54(4):1318–1327, 2006.
- [12] S. Vasudevan, R.H. Anderson, S. Kraut, P. Gerstoft, L.T. Rogers, and J.L. Krolik. Recursive Bayesian electromagnetic refractivity estimation from radar sea clutter. *Radio Science*, in press.
- [13] Caglar Yardim, Peter Gerstoft, and William S. Hodgkiss. Statistical maritime radar duct estimation using a hybrid genetic algorithms – Markov chain Monte Carlo method. *Radio Science*, in press.
- [14] Caglar Yardim, Peter Gerstoft, William S. Hodgkiss, and Ted Rogers. Statistical estimation of refractivity from radar sea clutter. IEEE Radar Conference, Boston, MA, April 2007.
- [15] M. Levy. *Parabolic Equation Methods for Electromagnetic Wave Propagation*. The Institution of Electrical Engineers, London, United Kingdom, 2000.
- [16] Caglar Yardim, Peter Gerstoft, and William S. Hodgkiss. Atmospheric refractivity tracking from radar clutter using Kalman and particle filters. IEEE Radar Conference, Boston, MA, April 2007.
- [17] Caglar Yardim, Peter Gerstoft, and William S. Hodgkiss. Tracking atmospheric ducts using radar clutter: I. evaporation duct tracking using Kalman filters. IEEE APS Conference, Honolulu, Hawaii, June 2007.
- [18] Caglar Yardim, Peter Gerstoft, and William S. Hodgkiss. Tracking atmospheric ducts using radar clutter: II. surface-based duct tracking using multiple model particle filters. IEEE APS Conference, Honolulu, Hawaii, June 2007.
- [19] Maurice W. Long. *Radar Reflectivity of Land and Sea*. Artech House, 3 edition, 2000.
- [20] David A. Shnidman. Comparison of low angle radar clutter models. *IEEE Trans. Aerosp. Electron. Syst.*, 41(2):736–746, 2005.
- [21] R. A. Paulus. Evaporation duct effects on sea clutter. *IEEE Trans. Antennas Propagat.*, 38 (11):1765–1771, 1990.
- [22] Tracy Haack and Stephen D. Burk. Summertime marine refractivity conditions along coastal California. *Journal of Applied Meteorology*, 40:673–687, 2001.

- [23] R. A. Paulus. An overview of an intensive observation period on variability of coastal atmospheric refractivity. In *AGARD/NATO Conference on Propagation Assessment in Coastal Environments*, Bremerhaven, Germany, February, 1995.
- [24] Ian M. Brooks, Andreas K. Goroch, and David P. Rogers. Observations of strong surface radar ducts over the Persian gulf. *Journal of Applied Meteorology*, 38:1293–1310, 1999.
- [25] Janet K. Stapleton, V. Russell Wiss, and Robert E. Marshall. Measured anomalous radar propagation and ocean backscatter in the Virginia coastal region. In *31st International Conference on Radar Meteorology*, Seattle, WA, August, 2003.
- [26] Amalia E. Barrios. A terrain parabolic equation model for propagation in the troposphere. *IEEE Trans. Antennas Propagat.*, 42 (1):90–98, 1994.
- [27] J. P. Reilly and G. D. Dockery. Influence of evaporation ducts on radar sea return. *IEE Proc. Radar and Signal Processing*, 137 (F-2):80–88, 1990.
- [28] Steven M. Kay. *Fundamentals of Statistical Signal Processing - Volume I: Estimation Theory*. Prentice-Hall, New Jersey, 1993.
- [29] S. Julier, J. Uhlmann, and H. F. Durrant-White. A new method for nonlinear transformation of means and covariances in filters and estimators. *IEEE Trans. Automat. Contr.*, 45:477–482, 2000.
- [30] E. A. Wan and R. van der Merve. *The unscented Kalman Filter*, in S. Haykin, *Kalman Filtering and Neural Networks*. John Wiley & Sons, New York, 2001.
- [31] Arnaud Doucet, Nando de Freitas, and Neil Gordon. *Sequential Monte Carlo Methods in Practice*. Springer, New York, 2001.
- [32] Branko Ristic, Sanjeev Arulampalam, and Neil Gordon. *Beyond the Kalman Filter, Particle Filters for Tracking Applications*. Artech House, Boston, 2004.
- [33] N. J. Gordon, D. J. Salmond, and A. F. M. Smith. Novel approach to nonlinear/non-Gaussian Bayesian state estimation. *IEE Proc.-F*, 140 (2):107–113, 1993.
- [34] H. L. van Trees. *Detection, Estimation and Modulation Theory*. John Wiley & Sons, New York, 1968.
- [35] Petr Tichavský, Carlos H. Muravchik, and Arye Nehorai. Posterior Cramér-Rao bounds for discrete-time nonlinear filtering. *IEEE Trans. Signal Processing*, 46 (5):1386–1396, 1998.

- [36] Space and Naval Warfare Systems Center, Atmospheric Propagation Branch, San Diego, CA. *User's Manual for Advanced Refractive Effect Prediction System*, 3.4 edition, April 2005.
- [37] B. W. Atkinson, J.-G. Li, and R. S. Plant. Numerical modeling of the propagation environment in the atmosphere boundary layer over the Persian gulf. *Journal of Applied Meteorology*, 40:586–602, 2001.
- [38] Stephen D. Burk, T. Haack, L. T. Rogers, and L. J. Wagner. Island wake dynamics and wake influence on the evaporation duct and radar propagation. *Journal of Applied Meteorology*, 42:349–367, 2003.
- [39] B. W. Atkinson and M. Zhu. Radar-duct and boundary-layer characteristics over the area of The Gulf. *Q. J. R. Meteorol. Soc.*, 131:1923–1953, 2005.
- [40] L. Ted Rogers. Effects of variability of atmospheric refractivity on propagation estimates. *IEEE Trans. Antennas Propagat.*, 44 (4):460–465, 1996.

5

Conclusions and Future Work

5.1 Conclusions

Using the radar itself to be able to infer the environment in which it is operating is one of the most promising techniques that can offer three dimensional real or near-real time estimates for atmospheric refractivity. The fact that it requires no extra hardware or measurement and that it only uses the normally discarded clutter portion of the radar signal is what makes the technique appealing.

The major drawbacks of RFC are: (1) it cannot detect ducts that do not interact with the surface such as elevated ducts, (2) there can be other non-ducting related patterns in the clutter structure such as rain and the variation in local sea state that will affect the estimation, and (3) it may be limited in the maximum range it can be used due to the lower clutter-to-noise ratios at longer ranges.

The contributions of this dissertation can be classified broadly into the following two parts.

5.1.1 Statistical Estimation of Refractivity

The first part, which includes Chapters 2 and 3, is devoted to the development of a general framework for the statistical estimation of atmospheric radio refractivity from a radar clutter measurement at a certain azimuth direction and

time. The main contributions and accomplishments on statistical duct estimation are listed below:

- The problem of inferring the atmospheric M-profile was formulated in a Bayesian framework so that the environmental parameters could be represented with their joint posterior probability distribution (PPD).
- Calculation of radar clutter in inhomogeneous lower atmospheric media was formulated using the very low grazing angle sea surface scattering of the electromagnetic field obtained by the narrow-angle split-step fast Fourier transform (FFT) based parabolic equation (PE) approximation to the wave equation.
- We were ultimately interested in the end-user parameters such as the propagation factor (F) or the one-way transmission loss (L) that could be used in radar calculations such as the detection probability (P_D), two-dimensional coverage diagrams and the false alarm rate. Therefore the joint PPD of the environmental parameters was used in the projection of the environmental statistics into the PPD's of parameters-of-interest via multi-dimensional Monte Carlo (MC) integration.
- These MC integrals, along with the maximum a posteriori (MAP) and the minimum mean square error (MMSE) estimates of range-independent environmental duct parameters were calculated using techniques such as the genetic algorithms (GA), simulated annealing (SA), two different Markov chain Monte Carlo (MCMC) samplers, namely the Metropolis-Hastings (M-H) and the Gibbs (GS) samplers and compared with the exhaustive search results. The analysis showed that GA resulted in the fastest but least accurate MC integrations whereas the MCMC samplers provided very accurate MC integrations but required a large number of forward model split-step FFT PE runs which limited their effective usage as a near-real time statistical RFC estimation technique.

- A hybrid GA-MCMC method based on the nearest neighborhood technique that approximates the environmental parameter PPD using a Voronoi decomposition of the multi-dimensional state space was introduced. This resulted in significantly reduced number of forward model calculations without significantly compromising the accuracy in MC integral calculations that were obtained using the MCMC samplers.
- The ability to solve large multi-dimensional problems with the hybrid GA-MCMC method allowed introduction of range-dependent refractivity profile estimation. This involved defining multiple profiles at certain range intervals and interpolating between them. Ability to use these complex range-dependent structures resulted in estimation of environmental profiles that matched very well the measured clutter and provided much more realistic environmental predictions.
- All of these techniques were tested successfully with the data collected during the Wallops'98 experiment conducted by the Naval Surface Warfare Center, Dahlgren Division. The radar clutter data gathered by the Space Range Radar (SPANDAR) was inverted using both range-dependent and range-independent environmental profiles and the results were compared with the helicopter refractivity profile measurements conducted by the Applies Physics Laboratory of John Hopkins University.

5.1.2 Refractivity Tracking

The second part, which includes Chapter 4, is devoted to the development of a general framework for the spatial and temporal tracking of the atmospheric radio refractivity. The main contributions and accomplishments on statistical duct estimation are listed below:

- The temporal and spatial environmental parameter evolution was formulated as a first order Markov process after analyzing the helicopter profiles collected

during the Wallops'98 experiment.

- The problem was formulated in a Kalman framework where the state variables were the environmental parameters with prior densities selected using the regional statistics, and the measurement equation was composed of the highly nonlinear split-step FFT PE and the log-normal distributed sea surface radar cross section (RCS).
- Since the problem proved to be nonlinear and non-Gaussian, three tracking algorithms, namely the extended Kalman filter (EKF), the unscented Kalman filter (UKF), and the sequential importance resampling particle filter (SIR-PF) were analyzed for suitability in various RFC tracking applications.
- Performance calculations of all three filters were carried out using the RMS errors, filter efficiency calculations obtained using the numerically computed posterior Cramér-Rao lower bounds, track divergence statistics, and computation times.
- The effect of increasing the number of particles in a typical RFC tracking problem was addressed and RMS error predictions were made for a realistic PF, where the number of particles was dictated by the filter update rates and the speed of the split-step FFT PE.
- Surface-based and mixed type duct tracking proved to be very challenging for the EKF and UKF since the underlying Kalman framework used in these filters proved inadequate to handle the level of nonlinearity and non-Gaussianity in the clutter and the SBD parameters. On the other hand, the PF performed well in these environments, attaining much higher filter efficiencies than the Kalman filters. It was concluded that even the simplest range-dependent SBD tracking would necessitate a particle filter type formulation.
- Unlike the SBD tracking, evaporation duct tracking results showed that the

Kalman filters performed remarkably well in these environments. The mild nonlinearity in the evaporation duct-induced clutter patterns enabled both the EKF and the UKF track the evaporation ducts better than the PF using low to medium number of particles. Since high particle numbers are computationally too expensive and will be impossible to implement in a real-time tracking system, our analysis showed that the best filter to use in evaporation duct tracking would be the UKF, closely followed by the EKF.

5.2 Future Work

This section contains some of the possible extensions to the work done throughout this dissertation.

- It is important to further test the techniques introduced in this dissertation. This involves performing RFC estimation in different regions of the world such as the Persian Gulf and the Mediterranean, where significant ducting occurs. Moreover, previous experiments conducted at Wallops Island were not designed to test RFC tracking capabilities. Therefore, RFC tracking currently remains relatively untested.
- Another interesting future work would involve the investigation of the performance of RFC in various regions of the world using the existing naval radar and communication systems. This may be extended to designing the best RFC system in terms of the radar parameters such as the frequency, height, pattern, and power that will operate in a given region, taking the regional statistics and the local conditions into account.
- The ultimate purpose is combining the results of all other methods mentioned in Chapter 1. This would involve combining the RFC with the local atmospheric measurements, mesoscale atmospheric prediction models, lidar and GPS measurements, and regional statistics in a single Bayesian data assimilation framework, where likelihood will be dictated by the radar return

and hence, the RFC. The prior will be the regional statistics for the unknown parameters and the mesoscale model forecast, updated by other techniques, will serve both as an initial guess and as an estimator for wind conditions and direction, enabling the parabolic equation to calculate F and σ^o more accurately. Starting with a good initial guess may enable us to linearize the problem around the solution and use techniques requiring less computation.

- Another important future work will involve the inclusion of land clutter into the RFC estimation and analysis of the effects of land clutter in RFC calculations. Almost all the previous work in the literature is based on the sea clutter. However, near the coastal zones the clutter return includes not only the sea surface reflected clutter but also the much stronger land clutter, with uniquely different characteristics, which may have significant effects on the RFC inversion. This introduces significant challenges since the constant sea surface RCS assumption explained in Section 1.3.2 no longer will work in a land clutter case, which would require a new formulation that will most likely necessitate a prior information about the current wind and sea conditions, topography and type of land (forest, open grassland, heavy vegetation, residential areas, farmland, snow covered land, desert) for accurate land and sea surface RCS measurements.
- It is possible to perform RFC using different transmitter configurations such as the multiple frequency, multiple launch angle, and multiple source height configurations. It is therefore desirable to predict the effects of these transmitter configurations on the RFC estimation and tracking performance.
- Another interesting area of investigation is the tracking of quickly changing environments. Throughout this thesis, it was assumed that the changes were gradual relative to the update rates. However, studies on the spatio-temporal duct evolution resulted in some observations with abruptly changing refractivity profiles. Therefore, it is desirable to extend tracking perfor-

mance predictions of the EKF, UKF, and the PF for these rapidly fluctuating environments.

- Finally, it may be possible to improve significantly the RFC tracking by designing higher order tracking algorithms that can handle different situations such as the calm and highly fluctuating evaporation ducts, SBD, and the mixed type ducts, all at the same time. This likely will require multiple state models which includes regime parameters that will be added to the environmental parameters. Some proposed filters are static multiple-model (MM) filters, different kinds of dynamic MM filters such as the interactive multiple-model (IMM) filter, multiple model particle filters (MMPF), and the Gaussian sum particle filters (GSPF).